# METAL-OXIDE CARRIER-SELECTIVE CONTACTS FOR ON-CHIP EMBEDDED PHOTOVOLTAICS

A DISSERTATION
SUBMITTED TO THE DEPARTMENT OF ELECTRICAL ENGINEERING
AND THE COMMITTEE ON GRADUATE STUDIES
OF STANFORD UNIVERSITY
IN PARTIAL FULFILLMENT OF THE REQUIREMENTS
FOR THE DEGREE OF
DOCTOR OF PHILOSOPHY

Raisul Islam
August 2017

© Copyright by Raisul Islam 2017
All Rights Reserved

Raisul Islam

I certify that I have read this dissertation and that, in my opinion, it is fully adequate in scope and quality as a dissertation for the degree of Doctor of Philosophy.

(Krishna C. Saraswat) Principal Adviser

I certify that I have read this dissertation and that, in my opinion, it is fully adequate in scope and quality as a dissertation for the degree of Doctor of Philosophy.

(James Harris)

I certify that I have read this dissertation and that, in my opinion, it is fully adequate in scope and quality as a dissertation for the degree of Doctor of Philosophy.

(Eric Pop)

Approved for the Stanford University Committee on Graduate Studies

# Abstract

In this thesis, a systematic study of transition metal oxide integration to thin crystalline silicon (c-Si) solar cells as carrier-selective contacts is presented. Thin c-Si solar cell technology is suitable for on-chip embedded photovoltaics to harvest energy from ambient light powering internet-of-things (IoT) systems for environmental, medical and agricultural monitoring. It has also the potential to be integrated with a perovskite cell to result in high efficiency ($> 30\%$) tandem cell on flexible substrate. Unlike the conventional Si photovoltaic (PV) cells, thin solar cells face loss of absorption due to thinner absorber which can be mitigated by adopting a light trapping technique. However, our simulation suggests that contact selectivity limits the performance significantly when the absorber gets thinner even if light trapping is adopted. Contact selectivity implies the ability of a contact to allow one type of carrier while blocking the other type, and p-n junction provides this in a conventional PV cell. It is observed that when the absorber thickness gets smaller, significant performance improvement can be achieved by improving the contact selectivity beyond what is obtained from a p-n junction.

In this thesis, transition metal oxides are introduced as carrier-selective contacts to thin Si solar cells. Using oxides having asymmetric band offsets to Si, the contact selectivity of p-n junction solar cell can be improved resulting in a significant improvement in solar cell efficiency. Next, a heterojunction structure of solar cell is introduced using these oxides that does not require any high doped junctions inside the Si absorber. Removing high doped regions from the area and thickness constrained on-chip PV cell and replacing them with the transparent oxides utilizes the absorber material efficiently. Detailed simulation study of the heterojunction structure is presented where the impact of metal Fermi level pinning on oxides and the doping of the oxides on device performance is studied. It is shown that characterizing the Fermi level pinning properties of these oxides is important. Therefore, the Fermi level pinning properties of nickel oxide contacts are studied, a promising hole selective material, on Si experimentally. We also observe that doping plays a critical role in determining the performance of the oxides as selective contacts. A novel technique of introducing p-doping into nickel oxide using ultra-violet (UV)/ozone treatment technique is shown. Both spectroscopic and electrical characterization suggests that UV/ozone treatment introduces Ni vacancy defects in nickel oxide, which dopes it p-type. Finally, the integration of nickel oxide and

titanium oxide as hole selective and electron selective contacts respectively in an ultra-thin Si solar cell (2 $\mu$m) is demonstrated showing 10.8% efficiency without any light trapping scheme used. This represents a $\sim$13% relative improvement from a control cell without any oxide contact. Detailed physical characterization of the contact heterostructures is provided to understand the mechanism of performance improvement. The thesis is concluded with an outlook for the future works regarding double heterojunction solar cell replacing highly doped homojunction.

# Acknowledgments

First, I would like to express my sincere gratitude to my advisor Prof. Krishna C. Saraswat, without whom this work would not have been possible. When I came to Stanford, I had a very minimal experience in nanofabrication. Prof. Saraswat believed in me and gave me a lot of opportunities to learn from my mistakes. He also supported me throughout the project by every possible means - be it financially or administratively or technically. To this day, I thoroughly enjoy my discussion with him, where he is eager to talk about anything from the future trends in technology to the current sports. I am lucky and honored to work with such an advisor who, besides being a great academician, is also a great human being.

Secondly, I would like to express my regards and appreciation for the support from my thesis readers and committee members. Specially, I would like to mention Prof. James Harris and Prof. Eric Pop. I have done some part of my work in collaboration with Harris group. His knowledge about photovoltaics is extra-ordinary. From our discussions I have learned a lot. I also attended EE 216 class offered by him which gave a great foundation of device physics. Prof. Pop has been a great source of inspiration. I have been very lucky to get involved in some of his research besides my thesis topic which certainly has broadened my horizon and provided versatility in my research thinking. Also, I always get inspired by his exuberance and energy. His focus towards the detail and perfection amazes me.

I should also mention Prof. Theodore Kamins and Prof. Roger Howe who were in my oral examination committee. Prof. Kamins has provided useful feedback regarding my research. My office was very close to Prof. Howe's office and I enjoyed our small talks regarding various topics almost every week.

I express my gratitude to all the funding sources. These are something which made this project literally possible by financially supporting me and my experiments over the years. These include - (i) Solar Energy Research Institute of India and US (SERIIUS): a joint collaborative effort between India and the US through the Department of Energy, (ii) TomKat Center for Sustainable Energy in Stanford University, (iii) Office of the Vice Provost for Graduate Education in Stanford University for the Stanford Graduate Fellowship (SGF), and (iv) National Science Foundation (NSF) EFRI 2-DARE grant 1542883.

I acknowledge all the collaborators in this work. Specifically, the collaborators outside Stanford University are Prof. Reuben Collins and Gang Chen from Colorado School of Mines, Donovan Lee and Nobi Fuchigami from Intermolecular Inc., Nils Brinkmann from Solexel Inc. and Yvonne Schiele from University of Konstanz in Germany. I thank all of them for their effort.

I acknowledge the help and support from all the group member and collaborators in Stanford Nanofabrication Facility. This include the past and present members of the Saraswat group - Ashish Pal, Ju Hyung Nam, Donguk Nam, Dave Sukhdeo, Jason Lin, Wooshik Jung, Suyog Gupta, Ze Yuan, Archana Kumar, Gautam Shine, Pranav Ramesh, Koosha Nassiri Nazif, Shashank Gupta, Aravindh Kumar, Junkyo Suh. The others whom I would like to thank are Muyu Xue, Yusi Chen, Zheng Lyu, Ching-Ying Lu, Sanchit Deshmukh, Connor McClellan, Isha Datye, Michal Mleckzko, Eilam Yalon, Saurabh Suryavanshi, Andrew Meng, Axel Palmstrom, Katherine Roelofs, Kevin Bush, Hongyuan Yuan and Chris English.

I acknowledge the mentorship from different mentors. They are - Dr. Pawan Kapur, Dr. Mehrdad Moslehi from Solexel Inc., Dr. Ali Kemal Okyay from Bilkent University, Turkey.

I also acknowledge the support of all the staff of SNF and SNSF for their help in figuring out different process issues and making sure all the tools run smoothly. Specially, I have to mention the names of Jim McVittie, Michelle Rincon, Uli Thumser, Mahnaz Mansourpour, Carsen Kline, Maurice Stevens, Xiaoqing Xu, Usha Raghuram from SNF and Chuck Hitzman from SNSF. The staff handling the financial and administrative matters of Saraswat group also deserve appreciation. They include - Gail-Chun Creech, Crystle Palafox, Francesca Jimenez, Melinda Nichols, and Chet Frost.

I thank all the staff members of EE department for their support and help.

I could not have survived the rigor of PhD research without the support from my friends both in the bay area and in Bangladesh. My friends believed in me, helped me when needed and always made sure I had a lot of fun. I am lucky to have so many good friends around me. I thank David, Scott, Paurakh, Chineyere, Jaime, Greg, Xue, Sumit, Tanwir, Saddam, Zunaid, Rifat, Shabab, Amit and many more. I should also mention Ishtiaq Hossain and Asif Islam Khan, who helped me a lot to settle down in a completely new country.

My family and my extended family are a source of my strength. My two brothers - Rizvi and Niloy, my brother and sister-in-laws, cousin - Robert, Sopan, Lupin, Sabrina and many more deserve more than just an acknowledgement for their support. I remember all the sacrifices made by my parents who made sure I get the best possible education with their limited resources. I am always proud of them.

Finally, I would like to finish this section by mentioning about my wife Anika Sharin. From day one in Stanford till today, she has been my greatest strength. She is someone whom I can always rely on, who I know will always support me and all my dreams and go whatever length she can to make sure I get all the happiness in life.

# Contents

**Abstract** **iv**

**Acknowledgments** **vi**

**1 Introduction** **1**
1.1 Motivation . . . . . 2
1.2 Organization of the Thesis . . . . . 6

**2 Beyond The Yablonovitch Limit: Improving Ultra-thin Solar Cell Performance By Contact Selectivity Improvement** **7**
2.1 Introduction . . . . . 7
2.2 Background . . . . . 9
2.2.1 Contact Selectivity . . . . . 9
2.2.2 Thermodynamic Limit of Light Trapping - Yablonovitch Limit . . . . . 12
2.3 Improving Contact Selectivity using Transition Metal Oxides . . . . . 14
2.4 Simulation Framework . . . . . 15
2.5 Results and Discussion . . . . . 19
2.5.1 Performance Limit of Thin c-Si Solar Cell with Oxide Selective Contact . . . 19
2.5.2 Towards a Double Heterojunction Solar Cell Replacing High Doped Homojunction . . . . . 23
2.6 Conclusion . . . . . 25

**3 Si Heterojunction Solar Cells: A Simulation Study of the Design Issues** **26**
3.1 Introduction . . . . . 26
3.2 Details of Simulation . . . . . 29
3.2.1 Interface Trap Distribution . . . . . 30
3.3 Fermi Level Pinning . . . . . 31
3.3.1 Electron-Selective Contacts . . . . . 33
3.3.2 Hole Selective Contacts . . . . . 33

3.4 Effect of Interface Defects . . . 34
3.4.1 Electron Selective Contact . . . 35
3.4.2 Hole Selective Contact . . . 37
3.5 Conclusion . . . 39

**4 Tuning Electrical Properties of Nickel Oxide using UV/ozone Treatment 41**
4.1 Introduction . . . 41
4.2 Experimental Section . . . 44
4.2.1 Film Deposition . . . 44
4.2.2 Resistivity Measurement . . . 44
4.2.3 UV/Ozone Treatment . . . 44
4.2.4 MIS Contact Fabrication . . . 45
4.2.5 Characterization . . . 46
4.3 Results and Discussion . . . 47
4.3.1 Resistivity and Ionization Potential . . . 47
4.3.2 X-ray Photoelectron Spectroscopy (XPS) . . . 47
4.3.3 Angle Resolved X-ray Photoelectron Spectroscopy (AR-PES) . . . 49
4.3.4 Extraction of Ni/O ratio . . . 51
4.3.5 Extraction of Hole Barrier Height . . . 53
4.4 Conclusion . . . 56

**5 Characterization of Oxide-Selective Contacts - Fermi Level Pinning Study and Contact Selectivity 57**
5.1 Introduction . . . 57
5.2 Fermi Level Pinning Theory . . . 58
5.3 Device Fabrication . . . 60
5.4 Extraction of Schottky Barrier Height . . . 62
5.5 Results and Discussion . . . 63
5.6 Asymmetry of Contact Resistivity as Contact Selectivity . . . 65
5.7 Contact Resistivity . . . 67
5.8 Device Fabrication . . . 68
5.9 Results and Discussion . . . 70
5.10 Lifetime Test Structures for Contact Recombination Study . . . 71
5.11 Summary . . . 72

**6 Contact Selectivity Engineering in Ultra-thin c-Si Solar Cells using Transition Metal Oxides 73**
6.1 Introduction . . . 73

6.2 Experimental Details . . . 77
6.2.1 Device Fabrication . . . 77
6.2.2 Transmission Electron Microscopy (TEM) . . . 78
6.2.3 X-ray Photoemission Spectroscopy (XPS) . . . 78
6.3 Results and Discussion . . . 79
6.3.1 Characterizing Cell Performance under Sun Simulator . . . 80
6.3.2 External Quantum Efficiency (EQE) . . . 81
6.3.3 Effect of Annealing on Cell Performance . . . 82
6.3.4 Transmission Election Microscopy (TEM) . . . 82
6.3.5 X-ray Energy Dispersion Spectroscopy (EDS) . . . 83
6.3.6 X-ray Photoemission Spectroscopy (XPS) . . . 84
6.4 Conclusion . . . 86

**7 Future Work and Summary of Contributions** **88**
7.1 Future Work on Heterojunction Solar Cells . . . 89
7.1.1 Towards Ultimate Thin Solar Cell using 2D Materials . . . 90
7.2 Summary of the Thesis . . . 91
7.3 Summary of Contributions . . . 92
7.3.1 Journals . . . 92
7.3.2 Conferences . . . 92

**Bibliography** **94**

# List of Tables


2.1 Material Parameters of the Oxides [43, 49, 50, 44, 47] . . . . . 17

4.1 Percentage of area under the fitted curve of O 1s spectra for NiOx having different UV/Ozone treatments at different angles of X-ray incidence. . . . . 49

5.1 Comparison of the pinning factor from experiments with that of theoretical calculation. 64

5.2 Comparison of the charge neutrality level extracted from experiments with that of reported values. $\phi_{Bp}$ is with respect to the valence band of Si and the rest are with respect to the vacuum. All values are in eV. . . . . 65

5.3 Comparison of the contact resistivity (m$\Omega$-cm$^2$) for different contact configurations. 70

6.1 Cell parameter summary of the device with the highest efficiency for each type of fabricated structure . . . . . 79

6.2 Average of the cell parameter among many cells from each type of fabricated device 79

# List of Figures


1.1 Potential IoT applications for a smart connected world. The figure is reprinted from [1]. . . . . 1
1.2 (a) The trend of IoT sensors scaling to trillions in the near future. The figure is reprinted from [2] (b) Available power for harvest from four major energy harvesting sources. The figure is taken from [3]. . . . . 2
1.3 Global usage of electricity forecast. . . . . 3
1.4 Historical trend in the installed solar capacity in different forms in the United States with a forecast till 2022. This figure is taken from [10]. . . . . 4
1.5 Two examples of current state of the art IoT systems with PV cell integration. The figure is taken from [11, 12]. . . . . 5
1.6 Schematic of a wireless sensor network system node (a) along with the cross-section of on-chip embedded PV device (b) . . . . . 6

2.1 Energy band diagram of a $p^+/n^-/n^+$ junction solar cell showing the common recombination mechanisms. . . . . 9
2.2 Schematic of a p-n junction diode showing the minority carrier possible diffusion direction inside the quasi-neutral region. . . . . 11
2.3 Simulated recombination current density for three mechanisms discussed here as a function of cell thickness. This plot is taken from [34]. . . . . 11
2.4 Schematic of an ideal light trapping scheme showing the possible mechanisms for light path enhancement (green arrow) and losses (red arrow). . . . . 12
2.5 Energy band diagram of a solar cell with band engineered layer enhancing contact selectivity. EBL = Electron Blocking Layer and HBL = Hole Blocking Layer. . . . . 13
2.6 Energy band alignment of different semiconductors and oxides. Data taken from [40, 41, 42] . . . . . 14
2.7 Schematic of the Simulated Device Structures. (a) Control Sample (b) Test Sample . 15
2.8 Absorption spectra of different layers in a thin c-Si solar cell for the cases of (a) single light pass and (b) Yablonovitch limit of light trapping. . . . . 17

2.9 (a), (b) Open circuit voltage and (c), (d) short circuit current of thin c-Si solar cell compared between direct metal contact and oxide selective contact as a function of absorber thickness. . . . . 18
2.10 Fraction of the total solar spectra (AM1.5G) absorbed in the absorber layer of a solar cell as a function of absorber thickness and number of light passes through the cell. . 19
2.11 Efficiency of the c-Si solar cell as a function of absorber thickness showing comparisons between direct metal contact and oxide selective contact devices for single pass and thermodynamic light trapping case. . . . . 20
2.12 Current density inside the cell as a function of distance, x (shown with the arrow), in the short circuit condition for different direction of illumination. . . . . 21
2.13 Energy band diagram of a double heterojunction solar cell with oxide selective contacts replacing high doped junctions. . . . . 22
2.14 Performance comparison of the heterojunction cell with that of a homojunction cell having equal thickness of emitter and back surface field. . . . . 23
2.15 (a),(b) Summarizing the efficiency comparison between cells with (blue) homojunction cell with direct metal contact (black) homojunction cell with oxide selective contact (red) heterojunction cell with oxide selective contact, (c) the schematics of the devices compared in (a) and (b). . . . . 24

3.1 Generic energy band diagram of (a) homojunction solar cell and (b) double heterojunction solar cell having Si absorber material. EBL is Electron Blocking Layer and HBL is Hole Blocking Layer. . . . . 27
3.2 Schematic of the device structure studied in this paper. Electron selective contacts and hole selective contacts are studied separately with respect to p and n Si respectively so that the heterojunction becomes the carrier separating junction. . . . . 28
3.3 Schematic of the interface defect distribution considered in this work. . . . . 30
3.4 Effective metal workfunction determined from Eq. 2 as a function of metal workfunction in (a) $TiO_2$ (b) ZnO (c) $CuAlO_2$ (d) NiO. The relative band offsets of oxides to Si (not to scale) and the position of the metal pinning level are also shown. The relevant material parameters are tabulated in table 2.1. . . . . 31
3.5 Cell performance ((a) $V_{oc}$ (b) % FF (c) % Efficiency) as a function of effective metal workfunction for the oxides studied in this work. . . . . 32
3.6 $TiO_2$ and ZnO heterojunction cell light I-V response at AM 1.5G spectrum for different metal workfunctions, interface passivation and oxide dopings. . . . . 34
3.7 Difference between Fermi level and valence band edge at the oxide/Si interface in equilibrium for $TiO_2$ and ZnO heterojunction cell under AM 1.5G spectrum. . . . . 35

3.8 Charge density stored in the interface trap states as a function of voltage. Both $TiO_2$ and ZnO electron selective contacts have been compared for different dopings, interface passivation and $\phi_{M,eff}$. . . . . 35
3.9 $CuAlO_2$ and NiO heterojunction cell light I-V response at AM 1.5G spectra for different metal workfunctions, interface passivation and oxide dopings. . . . . 36
3.10 Difference between Fermi level and valence band edge at the oxide/Si interface in equilibrium for $CuAlO_2$ and NiO heterojunction cell under AM 1.5G spectrum. . . . 38
3.11 Charge density stored in the interface trap states as a function of voltage. Both $CuAlO_2$ and NiO hole selective contacts have been compared for different dopings, interface passivation and $\phi_{M,eff}$. . . . . 38

4.1 Schematic of the fabricated MIS device structure. The active area of the device is 0.0377 $cm^{-2}$. . . . . 43
4.2 Surface morphology of the ultra-thin (10 nm) $NiO_x$ film spin coated on Si. (a) Before UV/ozone treatment (RMS roughness = 1.216 nm) and (b) After 30 min UV/ozone Treatment (RMS roughness = 1.366 nm). . . . . 43
4.3 Grazing incidence X-ray diffraction (GI-XRD) spectra of NiOx deposited by ALD at different temperatures. Irrespective of the temperature the XRD shows polycrystalline nature of the film. At 150 °C the peaks are weak. The peaks get stronger with higher temperature. . . . . 45
4.4 (a) Film resistivity and ionization potential as a function of UV/ozone treatment duration. 0 min signifies the as-deposited film. (b) PESA measurement showing the valence band spectra of $NiO_x$, which was used to extract the ionization potential. . . 46
4.5 X-ray photoelectron spectroscopy elemental scan of $NiO_x$ for (a) Ni $2p_{3/2}$ (b) O 1s and (c) C 1s for different UV/ozone treatment condition. . . . . 47
4.6 Angle resolved XPS spectra of O 1s for (a) as-deposited sample (b) 10 min UV/ozone treated sample and (c) 60 min UV/ozone treated sample for three different angles. . 48
4.7 Sputter depth profile of the XPS of $NiO_x$ deposited by ALD. The percentages at 0 sputter time indicates the XPS at the surface of the film. . . . . 48
4.8 Fitting of the O 1s spectra at different angles of photo-electron emission. The fitting is done for three different UV/ozone treatment conditions, (a) as-deposited (b) UV/ozone treatment for 10 minutes (c) UV/ozone treatment for 60 minutes. . . . . 50
4.9 Angle resolved XPS spectra of C 1s for (a) as-deposited sample (b) 10 min UV/ozone treated sample and (c) 60 min UV/ozone treated sample for three different angles. . 50
4.10 Angle resolved XPS spectra of Ni $2p_{3/2}$ for (a) as-deposited sample (b) 10 min UV/ozone treated sample and (c) 60 min UV/ozone treated sample for three different angles. . . . . 51

4.11 Fitting of the C 1s spectra at different angles of photo-electron emission. The fitting is done for three different UV/ozone treatment conditions, (a) as-deposited (b) UV/ozone treatment for 10 minutes (c) UV/ozone treatment for 60 minutes. . . . . 52
4.12 $NiO_x$ film stoichiometry extracted from XPS spectra as a function of the angle of XPS. Three different UV/ozone treatment conditions are shown. The dotted lines are a guide to the eye. . . . . 53
4.13 Current-voltage characteristics of metal/$NiO_x$/p-Si MIS contact (schematic shown in Fig. 4.1) for (a) Al (d) Cu and (g) Pd. Richardson plots extracted from the I-V characteristics at different temperatures are shown at different reverse bias voltages for as-deposited $NiO_x$ [(b) - Al, (e) - Cu, (h) - Pd] and for 30 min UV/ozone treated $NiO_x$ [(c) - Al, (f) - Cu, (i) - Pd]. . . . . 53
4.14 Effective barrier height extracted from the slope of the Richardson plots in Figure 4.13 as a function of reverse bias voltage for different metal contacts (a) Al (b) Cu and (c) Pd comparing the as-deposited and 30 min UV/ozone treated $NiO_x$. . . . . 54
4.15 Energy band diagram of Metal/$NiO_x$/p-Si for (a) as deposited and (b) UV/Ozone treated $NiO_x$. Three different metals' Fermi level pinning position is shown. UV/Ozone treatment reduces the pinning and increases vacancy defects (not drawn to scale). . 55

5.1 Fermi level pinning explained. (a) M-S contact where the Fermi level is pinned at the charge neutrality level. This is the case where S is closed to zero. (b) M-I-S contact where the Fermi level is depinned and effective Fermi level is aligned with the metal Fermi level. This is the case where S is closed to 1. . . . . 58
5.2 Energy band lineup of different semiconductors with known charge neutrality level and the resulting barrier height for electrons and holes written. . . . . 59
5.3 Metal/NiO/Si Schottky barrier contact to study Fermi level pinning. Top metal contact is varied (Al, Mo, Pt) in each sample. . . . . 60
5.4 X-ray Photoemission spectroscopy of the deposited NiO. (a) Survey scan (b) Elemental scan of Ni $2p_{3/2}$, $2p_{1/2}$ and O 1s peak shown. . . . . 61
5.5 Temperature dependent I-V characteristics of Metal/p-Si contact (top) and Metal/NiO/p-Si contact (bottom) from which the barrier height is extracted. . . . . 62
5.6 Richardson plot of the contacts for three different metals âĂŞ Al, Mo, Pt. (a) Metal/NiO/p-Si (b) Metal/p-Si. The plots are obtained from temperature dependent current-voltage measurement. . . . . 63
5.7 Extracted effective barrier height for holes as a function of metal workfunction shown for both with NiO and without NiO. The pinning factor (S) is the slope of the straight line connecting the data points. . . . . 64
5.8 Simulated contact resistivity as a function of NiO thickness for different bandgaps. The electron affinity is assumed 1.5 eV. . . . . 66

5.9 Linear TLM structure top view. . . . . 66
5.10 Linear R vs d characteristics of a typical TLM graph. . . . . 68
5.11 Current voltage characteristics of 4 TLM contacts along with the corresponding schematics. . . . . 69
5.12 Resistance vs. distance curve of the 4 TLM structures to extract $\rho_c$. . . . . 70
5.13 Schematic of the lifetime test structure for (a) Pt/Si and (b) Pt/NiO/Si contact and (c) extracted contact recombination factor $J_{0c}$ as a function of anneal temperature. 71

6.1 (a) Energy band diagram of a p-n junction solar cell showing the recombination mechanisms, (b) energy band diagram of a p-n junction solar cell with selective contacts. 74
6.2 Schematic of three groups of 2 $\mu$m thick ultrathin c-Si solar cells - (i) double sided, with both $NiO_x$ and $TiO_x$ carrier-selective contacts on p-contact and n-contact respectively, (ii) single sided, with only $NiO_x$ as hole selective contact on p-contact and (iii) control, no carrier selective contact on either contact. . . . . 75
6.3 Fabrication process flow of the solar cell with oxide selective contacts. . . . . 76
6.4 J-V characteristics of the champion cells under AM1.5G one sun illumination. The inset figure shows the zoomed-in J-V near open circuit condition to highlight the improvement in $V_{oc}$. . . . . 79
6.5 Scatter plot of cell performance metrics ($J_{sc}$, $V_{oc}$ and %FF) as a function of efficiency comparing the statistical distribution of cell performance. The green stars represent the average of the corresponding clusters. . . . . 80
6.6 External quantum efficiency (EQE) as a function of wavelength showing comparison between three groups of fabricated cells - control (black), single sided selective contact (blue), double sided selective contact (red). . . . . 81
6.7 J-V characteristics of the cell containing double sided selective contact before and after forming gas annealing at 450 °C for 90 sec. . . . . 82
6.8 Aberration corrected [110] zone axis high resolution transmission electron microscope images of (a) non-annealed Si/$SiO_x$/$TiO_x$/Ti/Al, (b) 450 °C forming gas annealed Si/$SiO_x$/$TiO_x$/Ti/Al, (c) non-annealed Si/$SiO_x$/$NiO_x$/Pt, and (d) 450 °C forming gas annealed Si/$SiO_x$/$NiO_x$/Pt. . . . . 83
6.9 Scanning transmission electron microscopy images showing the elemental analysis location (1-5) (left) and the spectra of spatially resolved x-ray energy dispersive spectroscopy on those locations (right) for (a) unannealed Si/$SiO_x$/$TiO_x$/Ti/Al, and (b) 450 °C forming gas annealed Si/$SiO_x$/$TiO_x$/Ti/Al. . . . . 84
6.10 Scanning transmission electron microscopy images showing the elemental analysis location (1-7) (left) and the spectra of spatially resolved x-ray energy dispersive spectroscopy on those locations (right) for (a) non-annealed Si/$SiO_x$/$NiO_x$/Pt, and (b) 450 °C forming gas annealed Si/$SiO_x$/$NiO_x$/Pt. . . . . 85

6.11 Elemental XPS spectra of (a) Si 2p (b) Pt 4f and (c) Ni 2p for Pt/$NiO_x$/Si interface before and after forming gas anneal at 450 °C for 90 sec. . . . . 86
6.12 Elemental XPS spectra of (a) Ti 2p (b) O 1s and (c) Si 2p for Ti/$TiO_x$/Si interface before and after forming gas anneal at 450 °C for 90 sec. . . . . 86

7.1 (a) The schematic of the heterojunction cell with NiO on the back of low doped Si absorber (b) Current voltage characteristics of NiO/n-Si heterojunction cell under 1-sun condition for different annealing temperature. . . . . 88
7.2 Cross-sectional TEM image of Pt/NiO/Si heterostructure contact showing significant $SiO_x$. The reason for $SiO_x$ formation is the oxidizing environment seen by Si during sputtering. . . . . 89

# Chapter 1

# Introduction

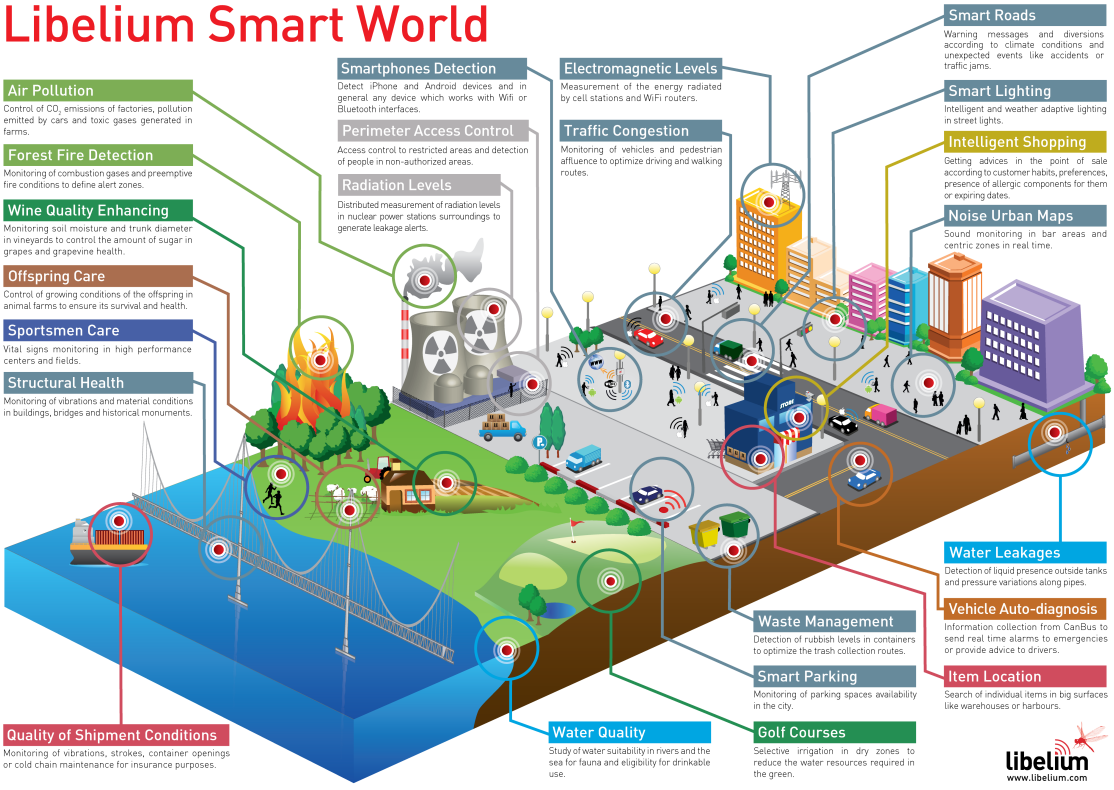


Figure 1.1: Potential IoT applications for a smart connected world. The figure is reprinted from [1].

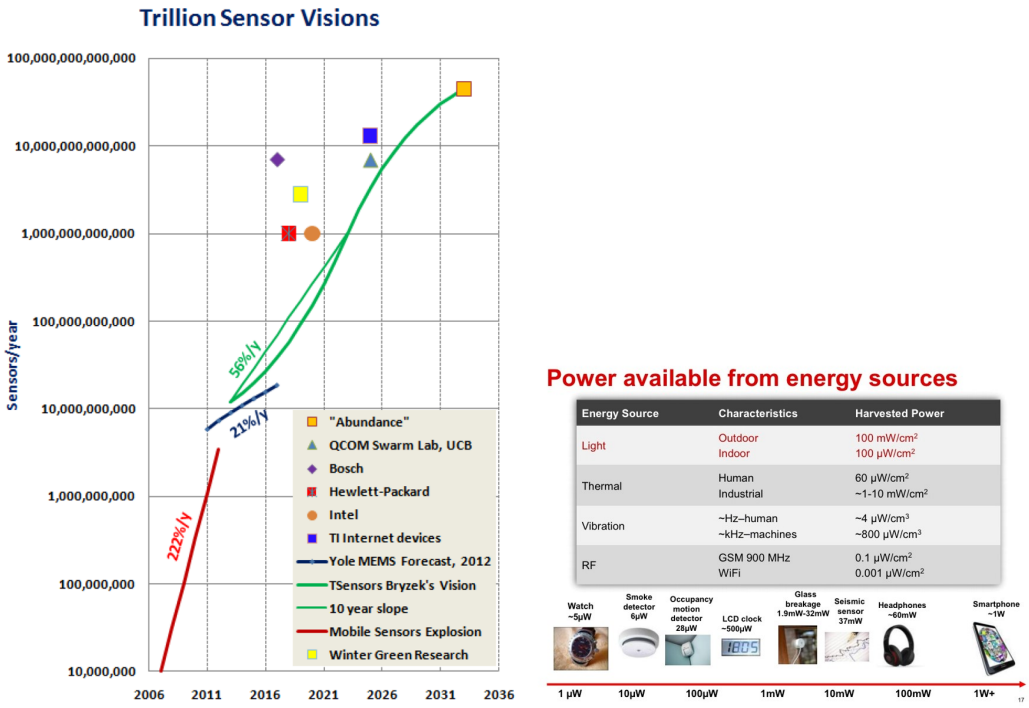


(a) (b)

Figure 1.2: (a) The trend of IoT sensors scaling to trillions in the near future. The figure is reprinted from [2] (b) Available power for harvest from four major energy harvesting sources. The figure is taken from [3].

## 1.1 Motivation

There has been a lot of speculation of how human civilization is going to be shaped in the future. Among different scenarios, one of the most important aspects that is agreed upon by most of the scholars is that the future world is going to be connected. The world is already getting more and more connected since the emergence of internet. After humans, the machines are also getting connected to each other and to humans through the internet-of-things (IoT). The IoT technology, a proliferation of multitudes of interconnected sensors and processors, is one of the most disruptive shift in technology since the origination of internet itself. The IoT promises passivity. The machines and tools that we use everyday will also monitor us and our surroundings and respond to our needs without instruction. At the core of the IoT is the wireless sensor networks, where a collection of sensors/sensing nodes communicate with each other and to the controlling station, typically through wireless channels, in order to collect spatially distributed data about their environment. Libelium Inc., a top IoT technology vendor, envisioned the future smart world by identifying potential important applications of the IoT sensor networks in Fig. 1.1 [1].

No matter how diverse the application space for IoT sensors is, one thing remains common - energy source for the sensors and the associated electronics. Traditionally the sensors get energy from batteries. However, IoT systems need to have their own power source in many applications. For example in environmental [4], agricultural [5] or harsh environment monitoring [6] battery is not desirable. Not only the maintenance and replacement cost for the batteries in these situations is prohibitive, batteries also poses environmental hazard if not disposed properly. Most importantly, the industry is currently envisioning of about a trillion sensor by the year 2036 (Fig. 1.2a). According to this figure, the mobile sensor market grew exponentially over 200 %/year between 2007 and 2014. Several organizations presented their visions for a continued growth to trillion sensors. Alongside with this massive growth in sensors, the energy demand in the wireless networks is increasing. The forecast shown in Fig. 1.3 reveals that by the year 2030, the highest share of global electricity usage will be in networks [7].

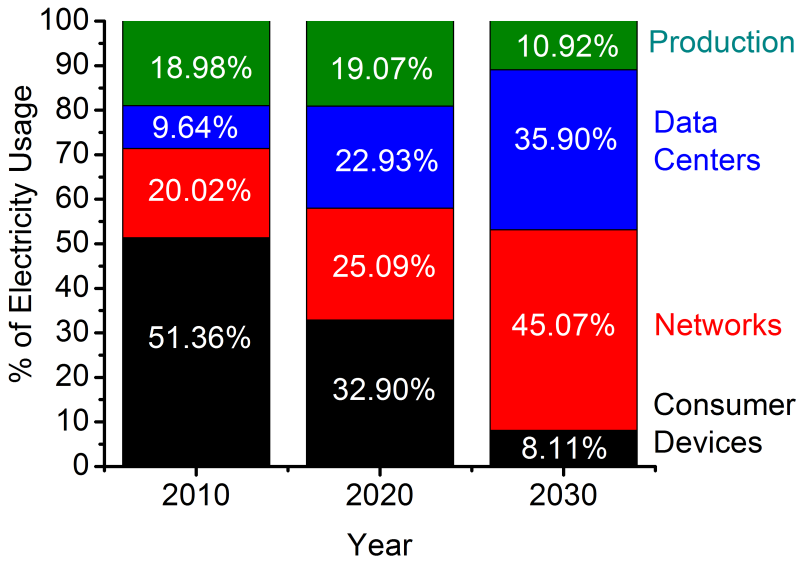


Figure 1.3: Global usage of electricity forecast.

With this enormous growth in IoT sensors, one of the biggest challenge is to reduce the energy waste. Even in low power mode, the 14 billion network enabled devices, which are currently in use worldwide, waste 400 TWh (terawatt-hour) of electricity. With 50 billion devices in 2020, the consumption will increase by factor 3.5 to over 1,400 TWh [8]. Energy waste presents a global issue for the IoT and is opposed to its resource saving benefits. In addition, if all of these devices were to be powered by batteries, people would need to dispose of hundreds of tons of hazardous waste every year - an irresponsible environmental impact and anything but future-proof. Even battery recycling is no alternative as it takes 6 to 10 times more energy to reclaim metals from some recycled batteries

than it does to produce it through other means, including mining [9].

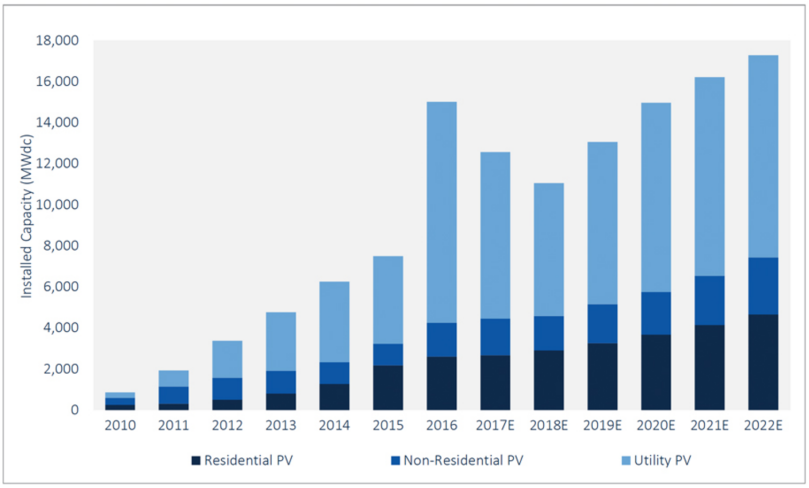


Figure 1.4: Historical trend in the installed solar capacity in different forms in the United States with a forecast till 2022. This figure is taken from [10].

Harvesting energy from alternative and renewable source can be a great way to solve the challenges posed by the batteries to power up billions of IoT sensors. Energy harvesting is the process of capturing ambient energy and utilizing it as electricity. There are 4 major sources of energy harvesting available from the environment -

1. Mechanical Energy (vibrations, deforemations)
2. Thermal Energy (temperature gradients or variations)
3. RF Energy (radio transmissions)
4. Solar Energy (sun, indoor and outdoor ambient light)

Fig. 1.2b shows the available power from the major energy harvesting sources along with the average power requirement for different consumer electronic and sensor products. Among these energy harvesting sources, photovoltaic (PV) energy harvesting has a high concentration of energy. Historically photovoltaic energy has been the dominant form of renewable energy for terrestrial and space application in the form of residential, commercial and utility based system. The growth of terrestrial PV in the United States over the years is shown in Fig. 1.4.

Typically energy harvesting from light occurs either as an embedded PV region in the chip formed using p or n doped well definition in silicon or through 3D integration of thin solar cell on top of the IoT chip. The example device in both of these cases are shown in Fig. 1.5.

A schematic of PV-integrated wireless sensor network system node 1.6a along with the cross-section of an on-chip PV cell 1.6b is shown. Irrespective of the method of integration, usually the

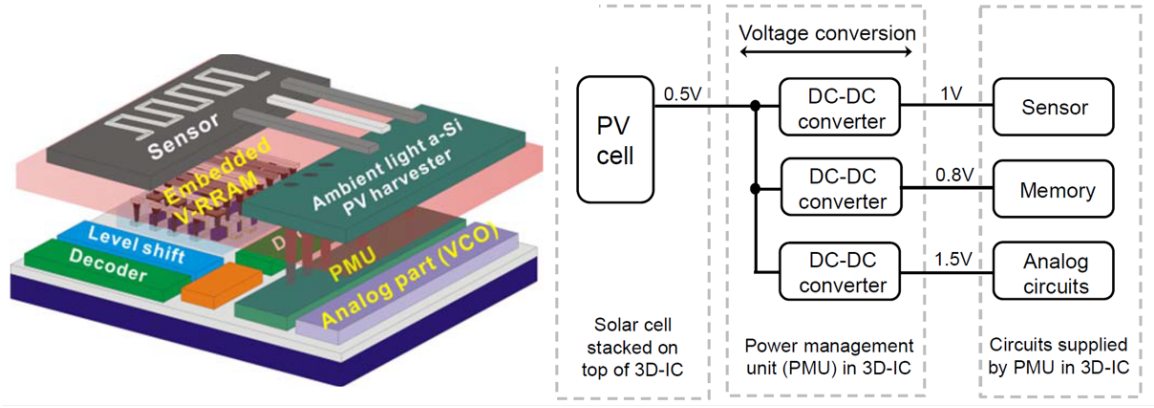


(a) Monolithic 3D⁺-IC IoT Chip

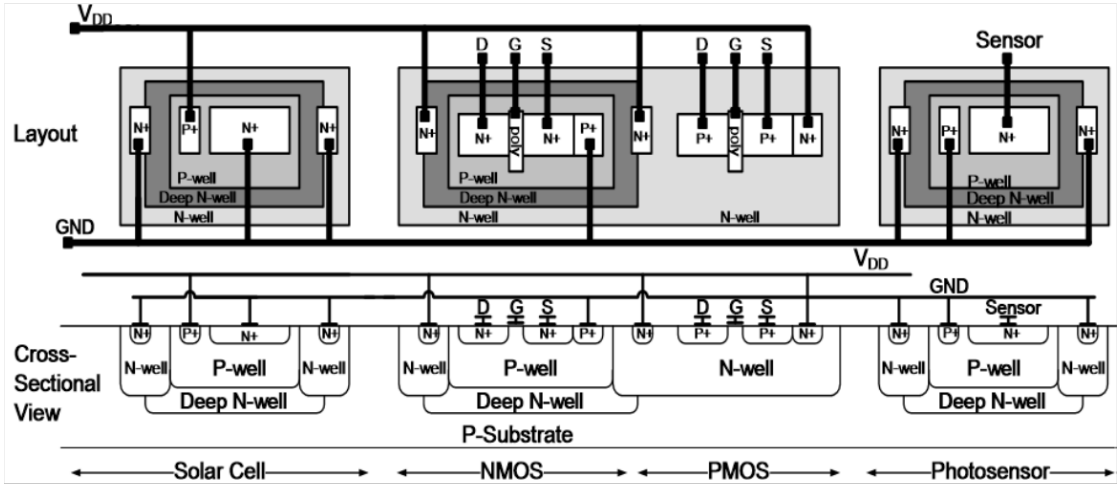


(b) Implantable Image Sensor for Subretinal Prosthesis

Figure 1.5: Two examples of current state of the art IoT systems with PV cell integration. The figure is taken from [11, 12].

on-chip PV device has significantly thinner absorber material (ultra-thin crystalline Si (c-Si) solar cell) than a terrestrial PV cell. This type of devices suffers two types of problems. One is insufficient light absorption (due to the indirect bandgap of Si) and the other is decreased contact selectivity. While there has been significant effort in the research community to address the insufficient light absorption issue, very little work has been done to address the contact selectivity issue specifically for ultra-thin c-Si solar cell.

Therefore, the purpose of this thesis is to address the contact selectivity issue in ultra-thin (c-Si) solar cell used for on-chip embedded photovoltaics to efficiently harvest energy for IoT sensors.

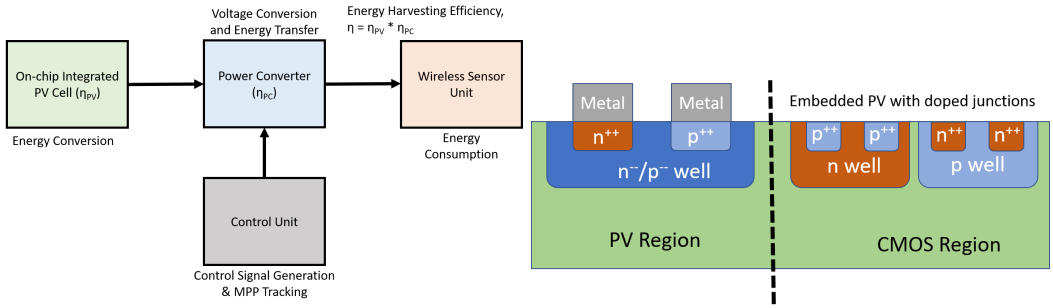


(a) Schematics of PV-integrated wireless sensor network system node

(b) Cross section of a chip with embedded PV system

Figure 1.6: Schematic of a wireless sensor network system node (a) along with the cross-section of on-chip embedded PV device (b)

## 1.2 Organization of the Thesis

This thesis consists of 7 chapters. Chapter 2 provides the background of ultra-thin c-Si solar cell and addresses the contact selectivity and light trapping problem. This chapter provides a simulation based study on the performance of solar cells as a function of absorber thickness and introduces transition metal oxides as a possible means to increase contact selectivity. This chapter also introduces a heterojunction based device scheme that does not require any high doped junction. Chapter 3 provides the detailed design optimization of heterojunction cell and identifies Fermi level pinning and oxide doping to be two of the most important design considerations. Chapter 4 introduces a novel technique to introduce p-type doping in nickel oxide (NiO) a promising material for hole selective contact. Detailed experimental results are discussed to understand the doping mechanism of the process. Chapter 5 shows different characterization techniques to quantify the effectiveness of a selective contact and shows that NiO can be a viable hole selective contact experimentally. Chapter 6 demonstrates the integration of NiO as hole selective contact to ultra-thin c-Si solar cell showing significant improvement in efficiency. This chapter also shows a 2 $\mu$m solar cell having both electron and hole selective contact (titanium oxide and nickel oxide respectively) having an efficiency of 10.8% which is $\sim$13% more compared to the control cell without any oxide selective contact. Finally, possible future direction of this research is discussed along with a summary of the thesis in chapter 7.

# Chapter 2

# Beyond The Yablonovitch Limit: Improving Ultra-thin Solar Cell Performance By Contact Selectivity Improvement

## 2.1 Introduction

Ultra-thin c-Si solar cells (having absorber layer of sub-10 $\mu$m) offer versatile benefit for energy harvesting. This technology has the potential to provide better stability and higher efficiency at low cost [13, 14]. Traditional thin film solar cell materials (CdTe, CIGS etc.) are not as stable as Si. Usage of less material for ultra-thin absorber also ensures lower cost. Through layer transferring, ultra-thin c-Si PV provides a path towards shrinking the material consumption cost by allowing multiple utilization of the substrate [15], which currently accounts for 40% of the module cost [16]. Thin absorber material is essential for flexible photovoltaics, creating the opportunity for photovoltaic energy harvesting in wireless sensor networks used in Internet-of-Things (IoT) application [17]. While the common flexible PV technologies (including the traditional thin-film technologies) are cheap and scalable, they suffer from long term stability and their potential for higher efficiency is limited, which is an important factor for energy harvesting in area constraint system like IoT sensors. Ultra-thin c-Si solar cell, if integrated with perovskite cells as tandems can promise $>$ 30% efficiency for a flexible PV system [18]. Ultra-thin c-Si PV technology can also harvest energy through on-chip embedded solar cells [12] or 3-D integration of solar cells onto chips [11]. This extends the usability of IoT sensor chips in harsh and natural environment for agricultural or environmental monitoring,

where batteries may not be sustainable energy harvesting source.

Unfortunately, silicon is not a strong absorber of sunlight despite holding more than 70% share of the overall PV industry. Therefore, scaling of the thickness of c-Si solar cell while ensuring the same or even better efficiency has been a significant research problem to this date [16]. The main challenge of scaling down the thickness of the absorber of c-Si solar cell is to make sure the solar spectrum is absorbed efficiently. Specially, the energy content in the infrared region of the solar spectrum is significant which gets absorbed poorly in ultra-thin c-Si solar cell and mostly transmitted through the material. The most straightforward solution to this problem is to employ light trapping. This process involves "folding" the light multiple times into the absorbing region of the solar cell, thereby increasing the optical path length of light and hence the probability of its absorption inside the solar cell. In other words, light trapping essentially increases the "optical" thickness of the absorber material. The ratio between the optical thickness and the absorber physical thickness is known as optical path length factor and is an important parameter in comparing different light trapping schemes.

Most commonly, light trapping is done by modifying the surface of the solar cell to increase the probability of total internal reflection. Also, it involves using anti-reflection coating in order to reduce the reflectivity at the air/absorber interface by using transparent material allowing gradual change in the index of refraction. By doing so, the reflection of light is reduced and it gets reflected back into the active volume several times before leaving the structure. There have been considerable efforts from the research community to address this issue by designing different schemes of light trapping. Most common technique is to texture the Si surface either to form upright or inverted regular pyramids [19, 20, 21] or by random textures [22]. These texturing is mostly suitable for bulk Si solar cells. For ultra-thin solar cells having absorber thickness below 10 $\mu$m, there are other techniques like - (i) nanophotonic light trapping that includes periodic semiconductor or dielectric structures [16] e.g. one dimensional (1D), single period or dual period two dimensional (2D) diffraction gratings, photonic crystals [23], nano-cones [24, 25] etc., (ii) plasmonic structures [26, 27], (iii) randomly structured semiconductor surfaces [28], (iv) Si nanowires [29] etc. Also, there are techniques which do not require physical nano-structuring but effectively increase the path length by increasing the local density of states [30] or introducing frequency shift [31].

The more light is trapped in an ultra-thin c-Si solar cell, the more confined the photogenerated carriers get inside the solar cell. This increases the minority carrier concentration at the metal contact interface. Given that the absorber lifetime remains high, with absorber thickness scaling, the contact recombination becomes a dominant component in the overall loss mechanism. In this chapter, the problem of imperfect contact is addressed for ultra-thin c-Si solar cell. Specifically, our simulation study shows that contact selectivity problem is more prominent when light trapping is employed to increase the light absorption. Improving the contact selectivity can improve the performance more for the case where light trapping is involved compared to the case of planar Si

cell.

## 2.2 Background

In this section, the theoretical background on the contact selectivity and the thermodynamic limit of light trapping will be discussed.

### 2.2.1 Contact Selectivity

With respect to photovoltaics, contact selectivity is defined as the ability of a contact to pass one type of carrier (electrons/holes) while blocking the other type (holes/electrons). The contact which allows electrons to pass and blocks holes is called electron selective contact (ESC)/ hole blocking contact (HBC). The other type of contact that allows holes to pass and blocks electrons is called hole selective contact (HSC)/ electron blocking contact (EBC). The photovoltaic power generation is composed of three basic steps -

1. Light Absorption and Carrier Generation
2. Carrier Separation and Transport to the Contacts
3. Carrier Extraction and Deliver Power to the Load

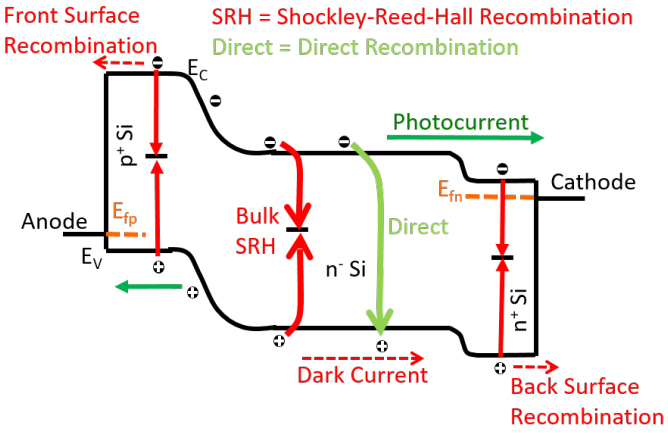


Figure 2.1: Energy band diagram of a $p^+/n^-/n^+$ junction solar cell showing the common recombination mechanisms.

Typically, a $p^+/n^-/n^+$ or $n^+/p^-/p^+$ homojunction fabricated by doping c-Si can perform all the three steps. The lightly doped middle layer ($n^-/p^-$) is the thickest region of the cell and called the absorber. It mostly absorbs the light and generates electron-hole pairs (ehp). The contact

regions are highly doped junctions. Usually the thickness of the contact regions is determined by the requirement for lateral conduction and contact resistivity. Both $n^+$ and $p^+$ contacts ensure that each contact can pass only one type of carrier while blocking the other type. The blocking function of the contacts requires the band bending between the differently doped junctions. In the regions close to the junction there is high electric field, which creates the force to separate ehp. In between the junction region lies the quasi-neutral region where the dominant method of transport is through diffusion. Fig. 2.1 shows the energy band diagram of a $p^+/n^-/n^+$ junction solar cells with the common recombination mechanisms. The electrons are extracted through the cathode ($n^+$) contact and the holes are extracted through the anode ($p^+$) contact (shown as photocurrent in green arrow). The undesired current flows in the opposite direction (shown as dark current in red arrow). There are mostly three components to this dark current - (i) bulk Shockley-Read-Hall (SRH) recombination (ii) radiative recombination and (iii) front and back surface recombination. Other than these three there is auger recombination, but that is only relevant for very high injection condition [32] and so we are ignoring it for this analysis. Also, for an indirect bandgap material like Si, radiative recombination is insignificant compared to the the other two recombination mechanisms and that is why it will also be omitted from our discussion. So, bulk SRH recombination and the front and back surface recombination plays the significant role in determining the overall efficiency of a solar cell. The total current density of a p-n junction solar cell is given by,

$$J = J_{ph} - J_{dark} \tag{2.1}$$

Here, $J_{ph}$ and $J_{dark}$ is the photocurrent and the dark current respectively. The dark current with its three components of recombination can be modeled as,

$$J_{dark} = J_{0,Front}\left[exp\left(\frac{qV}{n_1kT}\right)\right] + J_{0,Back}\left[exp\left(\frac{qV}{n_2kT}\right)\right] + J_{0,Bulk}\left[exp\left(\frac{qV}{n_3kT}\right)\right] \tag{2.2}$$

$J_{0,Front}$ and $J_{0,Back}$ corresponds to the front and back surface recombination velocity respectively, according to the following equations [33],

$$J_{0,Front} = \frac{qS_{n,0}p_i^2}{p_s} \tag{2.3}$$

$$J_{0,Back} = \frac{qS_{p,0}n_i^2}{n_s} \tag{2.4}$$

Here, $S_{n,0}$ and $S_{p,0}$ are the surface recombination velocity of the electrons and holes at the interface respectively. $J_{0,Bulk}$ represents the reverse saturation current due to the bulk recombination both in the quasi-neutral and the space-charge region. The bulk recombination mostly depend on the lifetime of the minority carrier. The minority carrier lifetime determines the diffusion length of

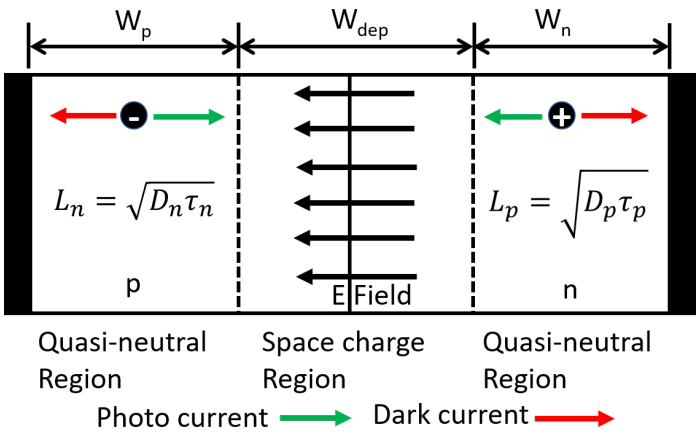


Figure 2.2: Schematic of a p-n junction diode showing the minority carrier possible diffusion direction inside the quasi-neutral region.

the carrier in the quasi-neutral region in the following way,

$$L_{p/n} = \sqrt{D_{p/n}\tau_{p/n}} \tag{2.5}$$

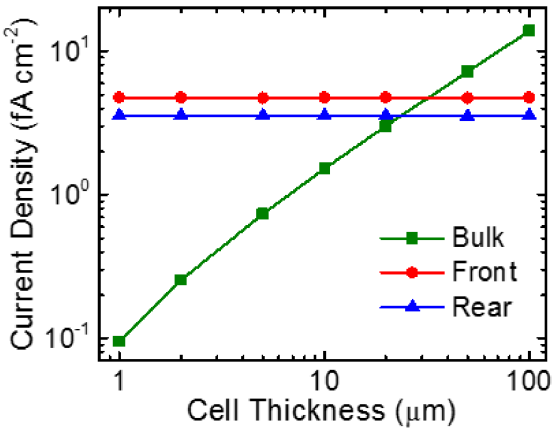


Figure 2.3: Simulated recombination current density for three mechanisms discussed here as a function of cell thickness. This plot is taken from [34].

Here, the subscripts p means hole and n means electron. L, D and $\tau$ represents diffusion length, diffusion coefficient and the lifetime of the carrier respectively. Fig 2.2 shows a schematic of a typical p-n junction diode showing the possible minority carrier diffusion direction in the quasi-neutral region of the device. The electric field direction in the space charge region is shown to assist the carrier extraction for power generation. Therefore, the bottleneck is the diffusion of minority carriers in

the quasi-neutral region which depends on the lifetime and diffusion length of the minority carrier. If $W_p >> L_n$ or $W_n >> L_p$ the dark current ($J_{0,Bulk}$) is determined by the bulk lifetime (typically known as long base diode assumption). Most of the terrestrial solar cells satisfy the assumption and hence the recombination loss is mostly SRH bulk recombination through the trap states inside the quasi neutral region. However, when $W_p \leq L_n$ or $W_n \leq L_p$, the overall dark current has significant contribution from the surface recombination. This is because the diffusion is equally probable in any direction, so the minority carrier have higher probability of reaching to the contacts before recombining in the bulk. Since, the surface recombination velocity depends mostly on the interface trap states which does not scale with the thickness of the device, we can conclude that for ultra-thin c-Si solar cell, the lowering the surface recombination velocity can also improve the performance of the cell significantly. Fig. 2.3 compares the bulk vs the surface recombination current as a function of cell thickness. In this simulation [34], the bulk lifetime of the cell is considered relatively high ($\tau_{bulk} = 1ms$). This figure suggests that for ultra-thin c-Si solar cell contact becomes a bottleneck for higher performance. In other words, the contacts need to be more selective than what is obtained from direct metal contact to $p^+/n^-/n^+$ or $n^+/p^-/p^+$ homojunctions.

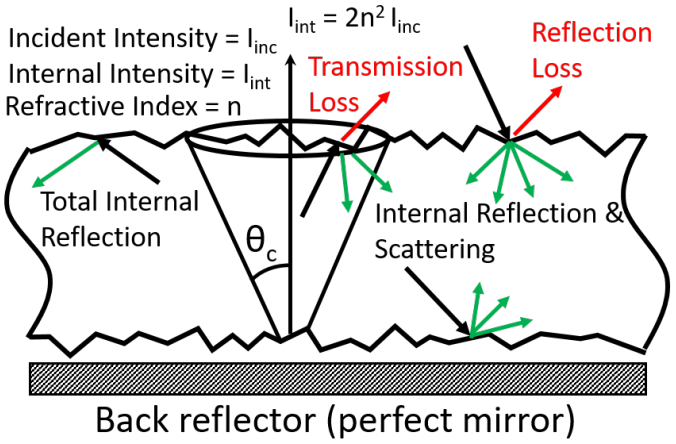


Figure 2.4: Schematic of an ideal light trapping scheme showing the possible mechanisms for light path enhancement (green arrow) and losses (red arrow).

### 2.2.2 Thermodynamic Limit of Light Trapping - Yablonovitch Limit

In order to evaluate the relative improvement from increasing the light trapping in ultra-thin c-Si solar cell, the thermodynamic limit of light trapping is a useful metric. It was first calculated by Eli Yablonovicth in the early 80's [35, 36]. The fundamentals of light absorption enhancement is explained using Fig. 2.4 where the perfect light trapping scheme is shown. In this calculation, lambertian light trapping is assumed [37] where the the light ray is assumed to lose all its direction

information and completely randomizes after getting scattered from a diffusely scattering textured surface. A perfect mirror is assumed to reflect all the transmitted light from the back surface (Fig. 2.4). Using this formalism, it can be shown that the internal light intensity is enhanced by a factor of $2n^2$ from the incident light intensity where n is the refractive index of the media. For silicon, $2n^2 \approx 25$. This means that a light ray in silicon is expected to make 25 passes on average before escaping [35]. Considering the normal incident light, taking the angular distribution of light rays into account the absorption is enhanced by a factor of $4n^2$. The Yablonovitch limit gives an upper limit to the light trapping for bulk crystalline silicon. For ultra-thin silicon, when the thickness of the cell becomes comparable to the wavelength of light, the usual ray optics based limit does not work. In that case wave optics can be used to find the nanophotonic light trapping limit [38]. In fact light trapping beyond the conventional thermodynamic limit of $4n^2$ has been demonstrated [31, 30, 38, 39].

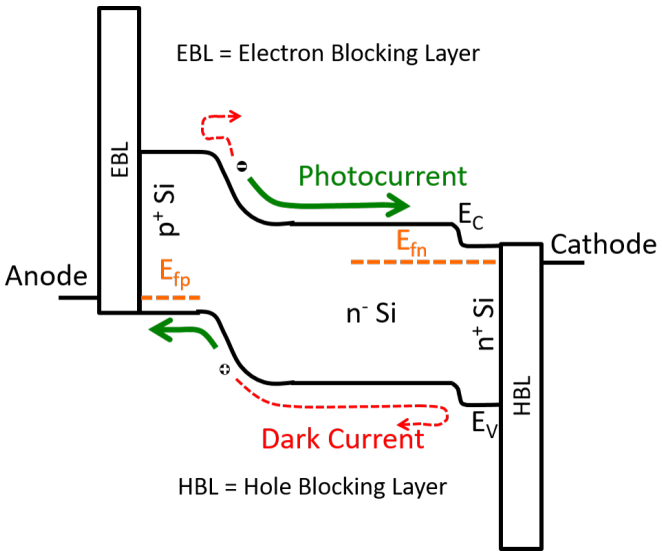


Figure 2.5: Energy band diagram of a solar cell with band engineered layer enhancing contact selectivity. EBL = Electron Blocking Layer and HBL = Hole Blocking Layer.

In this chapter, we show that using better photogenerated carrier management, performance enhancement is possible beyond the Yablonovitch limit. Improving contact selectivity is not light trapping in the usual sense. Since the ultimate goal of light trapping is to enhance the efficiency of the solar cell, increasing the contact selectivity is shown to be an effective technique of pushing the performance of the solar cell beyond the thermodynamic limit of light trapping. Light trapping results in better photon management. Selective contact results in better carrier management. The goal of this chapter is to show that it is not one or the other but both that can ensure best possible energy harvesting from ultra-thin c-Si solar cell.

## 2.3 Improving Contact Selectivity using Transition Metal Oxides

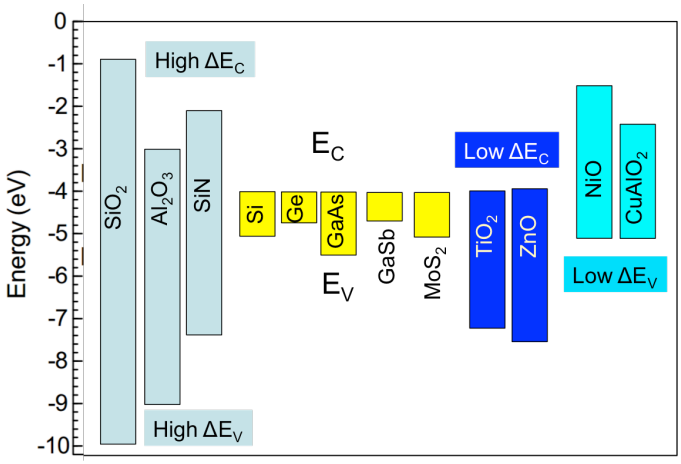


Figure 2.6: Energy band alignment of different semiconductors and oxides. Data taken from [40, 41, 42]

Fig. 2.5 shows the energy band diagram of a contact structure to improve the contact selectivity beyond the metal/semiconductor contact. Here, ultra-thin (nanometer scale) selective contact interlayer is used between metal and silicon (shown as EBL and HBL) to block the dark current and allow the photocurrent. EBLs have high conduction band offset and low valence band offset while the HBLs have high valence band offset and low conduction band offset with Si. The material can be either a semiconductor or an insulator. The basic rationale behind this contacting scheme is that although heterojunction between two semiconductors or semiconductor/insulator is far from ideal containing trap states to allow contact recombination current, the number of trap states is still a few orders of magnitude lower compared to the metal/semiconductor interface. As a result the contact recombination current can be reduced significantly allowing better carrier management. Also, due to high band offset for the minority carrier, the diode injection current in the forward bias will be completely blocked. The low band offset for the majority carrier will ensure that there is no significant barrier to the photo-generated current. Ideally the interface between EBL(HBL)/Si needs to be completely passivated. In practice, although perfect interface cannot be ensured, good interface passivation is possible using different surface treatment and annealing technique. Transition metal oxides (TMO) can be good candidates as selective contact layer for solar cells. Among different properties of TMO, the most important properties that can be useful for this purpose are - (i) ability to be doped from defects or extrinsic dopant species, (ii) usually wide bandgap that is transparent to the visible spectrum of sunlight and (iii) widely varying band lineup with Si. Fig. 2.6 shows the energy band alignment of different oxides and semiconductors with respect to Si and other

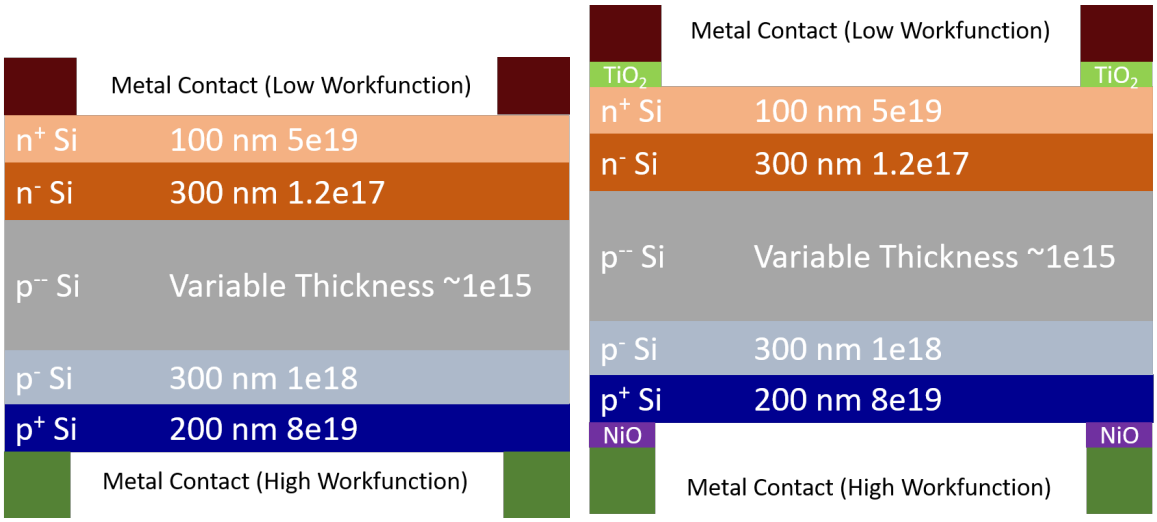


(a) Device with Direct Metal Contact (b) Device with Oxide Contact

Figure 2.7: Schematic of the Simulated Device Structures. (a) Control Sample (b) Test Sample

semiconductors. From this figure, we can see that titanium oxide ($TiO_2$) and zinc oxide (ZnO) have low conduction band offset, $\Delta E_C$, and high valence band offset, $\Delta E_V$ with respect to Si, making these suitable for electron selective contact or hole blocking layer (HBL). The opposite is true for nickel oxide (NiO) and copper aluminum oxide ($CuAlO_2$), making these suitable for hole selective contact or electron blocking layer (EBL).

Moreover, $TiO_2$ and ZnO are n type semiconductors, where both extrinsic and intrinsic doping through oxygen vacancy is possible [43]. ZnO has been shown to dope heavily with aluminum. On the other hand, NiO and $CuAlO_2$ are p type semiconductors, where both extrinsic and intrinsic doping through cation vacancy is possible. All of these four materials have been studied as window layer or transparent conducting oxide (TCO) for photovoltaics [44, 45, 46, 47] due to their optical transparency in the visible spectrum and distinct semiconducting properties. In this chapter, the simulation results shown are done using $TiO_2$ and NiO to understand the effect of absorber thickness on contact selectivity. Evaluation and relative comparison of these materials from selective contact point of view will be presented in another chapter.

## 2.4 Simulation Framework

Fig. 2.7 shows the schematic of the device structure simulated in this chapter. The software package AFORS-HET 2.5 (Automat FOR Simulation of Heterostructures) is utilized in order to simulate the selective contact solar cells [48]. In AFORS-HET, The 1-D Poisson equation and the carrier continuity equations are solved within the optical carrier generation determined by the Beer-Lambert

law as given below:

*Poisson Equation*,

$$\frac{\epsilon_0 \epsilon_r}{q} \frac{\partial^2 \phi\,(x,t)}{\partial x^2} = p\,(x,t) - n\,(x,t) + N_D\,(x) - N_A\,(x) + \sum_{trap} \rho_{trap}\,(x,t) \tag{2.6}$$

*Transport Continuity Equation*,

$$-\frac{1}{q}\frac{\partial^2 j_n(x,t)}{\partial x^2} = G_n(x,t) - R_n(x,t) - \frac{\partial n(x,t)}{\partial t} \tag{2.7a}$$

$$-\frac{1}{q}\frac{\partial^2 j_p(x,t)}{\partial x^2} = G_p(x,t) - R_p(x,t) - \frac{\partial p(x,t)}{\partial t} \tag{2.7b}$$

*Beer-Lambert Law*,

$$G(x,t) = \int_{\lambda_{min}}^{\lambda_{max}} d\lambda \Phi_0(\lambda,t) R(\lambda) A(\lambda) \alpha_x(\lambda) e^{-\frac{\alpha_x(\lambda)}{cos(\gamma)}} \tag{2.8a}$$

$$\alpha_x(\lambda) = \frac{4\pi k(\lambda)}{\lambda} \tag{2.8b}$$

Here, the meaning of the symbols are given below:

1. $\epsilon_r$ = Relative permittivity of the semiconductor
2. $\phi$ = Electric potential
3. $n,\ N_D$ = Electron concentration, Donor doping concentration
4. $p,\ N_A$ = Hole concentration, Acceptor doping concentration
5. $j_n/j_p$ = Electron/Hole current density
6. $G_n/G_p$ = Electron/Hole generation rate
7. $R_n/R_p$ = Electron/Hole generation rate
8. $\Phi_0$ = Incoming spectral photon flux
9. $R(\lambda)$ = Reflectance of the contact
10. $A(\lambda)$ = Absorptance of the contact
11. $\alpha_x(\lambda)$ = Spectral absorption coefficient of the semiconductor
12. $k(\lambda)$ = Extinction coefficient of the semiconductor
13. $cos(\gamma)$ = Factor to consider path length enhancement of light from textured surface

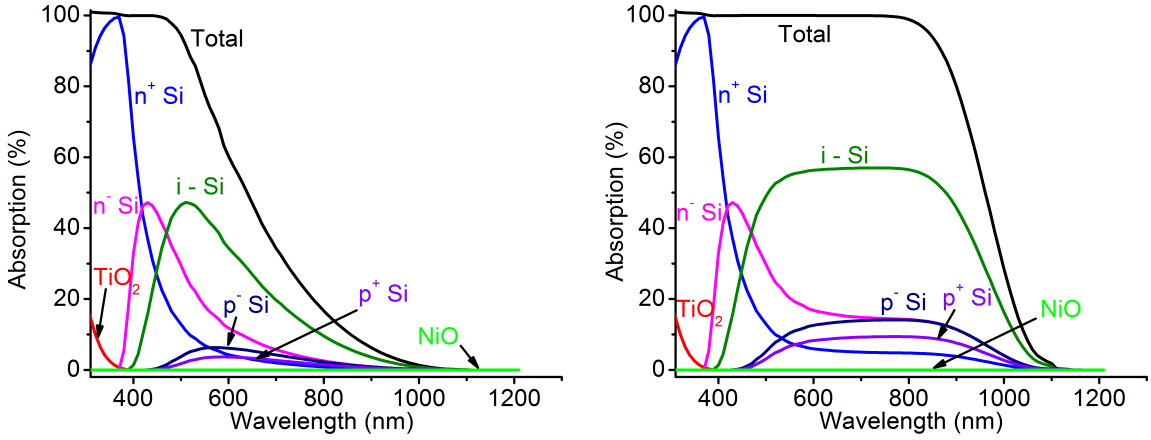


(a) Single pass of solar spectra

(b) Yablonovitch limit of light trapping

Figure 2.8: Absorption spectra of different layers in a thin c-Si solar cell for the cases of (a) single light pass and (b) Yablonovitch limit of light trapping.

The absorber thickness is varied from 1 $\mu$m to 120 $\mu$m while keeping the high doped region same. We only scale the absorber thickness because the need to ensure low series resistance of the cell restricts the minimum thickness of the emitter and back surface field regions. The standard AM1.5G spectrum is used to calculate photo-generated carriers given the experimentally extracted absorption coefficient of Si. The oxides were simulated as wide bandgap semiconductors with the parameters taken from the published literature and are assumed to not absorb any photons. The oxide properties used in this simulation study is given in the following table 2.1. This table provides

Table 2.1: Material Parameters of the Oxides [43, 49, 50, 44, 47]

| Metal Oxide | $TiO_2$ | ZnO | $CuAlO_2$ | NiO |
|---|---|---|---|---|
| Dielectric Constant, k | 86 | 7.96 | 7.7 | 11.75 |
| Electron Affinity, $\chi$ (eV) | 4 | 4 | 2 | 1.8 |
| Bandgap, $E_g$ (eV) | 3.2 | 3.4 | 3.0 | 3.6 |
| Effective Density of States (Conduction Band), $N_C$ ($cm^{-3}$) | $7.93 \times 10^{20}$ | $3.92 \times 10^{18}$ | $8.87 \times 10^{18}$ | $8.87 \times 10^{18}$ |
| Effective Density of States (Valence Band), $N_V$ ($cm^{-3}$) | $1.79 \times 10^{19}$ | $3.34 \times 10^{18}$ | $7.57 \times 10^{18}$ | $7.57 \times 10^{18}$ |
| Electron Mobility, $\mu_n$ ($cm^2/Vs$) | 0.1 | 60 | 0.12 | 0.1 |
| Hole Mobility, $\mu_p$ ($cm^2/Vs$) | 0.1 | 3 | 0.12 | 0.1 |
| $\phi_{CNL}$ (w.r.t. Vacuum) (eV) | 4.6 | 4.12 | 4.2 | 4.85 |
| Pinning Factor, S | 0.24 | 0.58 | 0.37 | 0.26 |

an extensive list of the relevant material parameters for all the materials considered in simulation for this and the subsequent chapters. For the experimental proof-of-concept, only $TiO_2$ and NiO are considered. For the purpose of light trapping simulation, multiple passing of incident light is

considered, which in each pass loses its intensity as determined by the Beer-Lambert law. Since, Yablonovitch limit stipulates an average of 25 passes in silicon before the light escapes, we consider 25 passes of light to be equivalent of simulating the thermodynamic limit of light trapping. The absorption spectra for different layers of the device shown in Fig. 2.7b is shown in Fig. 2.8. We observe that with single pass in a thin c-Si solar cell a significant portion of infrared is lost. Light trapping enhances the effective path length which improves the absorption in the infrared region of the spectra.

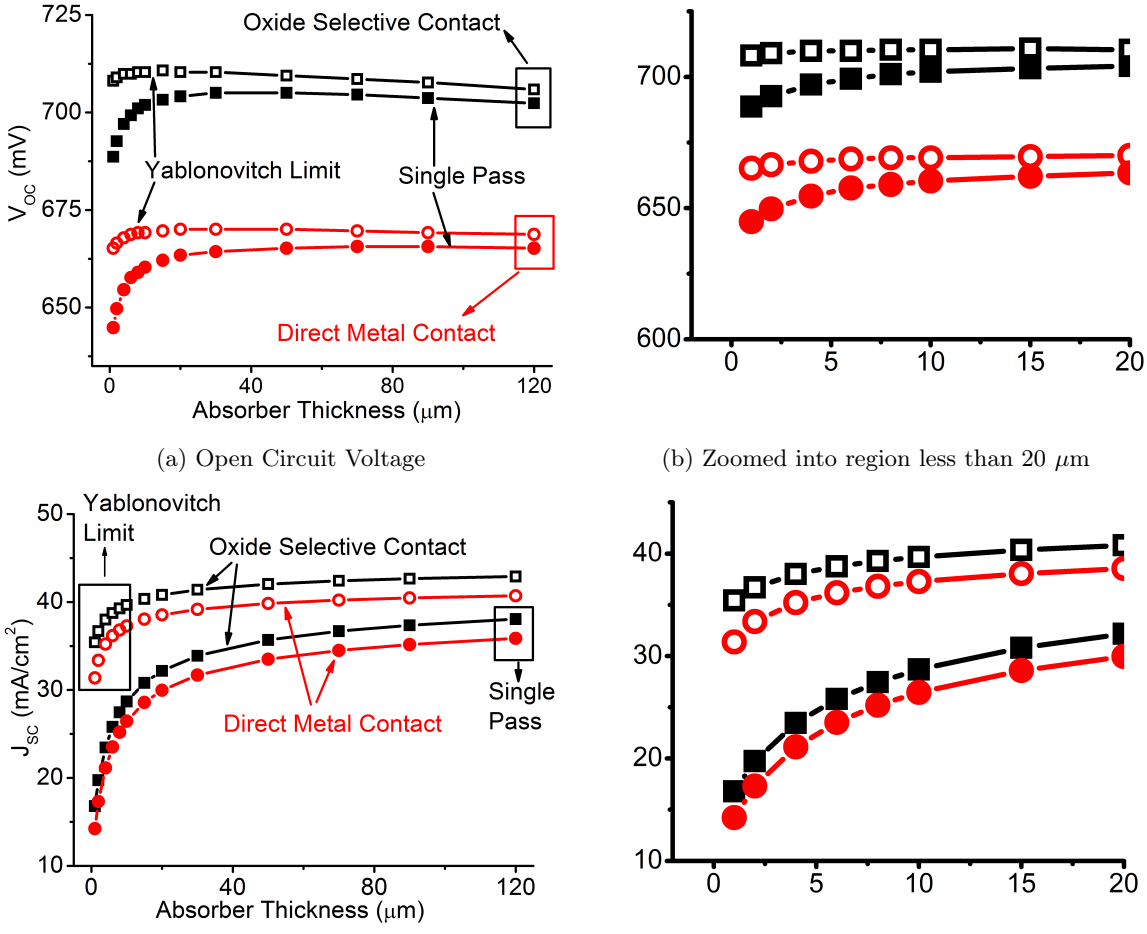


(a) Open Circuit Voltage

(b) Zoomed into region less than 20 $\mu$m

(c) Short Circuit Current

(d) Zoomed into region less than 20 $\mu$m

Figure 2.9: (a), (b) Open circuit voltage and (c), (d) short circuit current of thin c-Si solar cell compared between direct metal contact and oxide selective contact as a function of absorber thickness.

## 2.5 Results and Discussion

### 2.5.1 Performance Limit of Thin c-Si Solar Cell with Oxide Selective Contact

Fig. 2.9 shows the performance metrics ($V_{oc}$ and $J_{sc}$) of c-Si solar cell shown in Fig. 2.7 as a function of absorber thickness. In each figure, $V_{oc}$ and $J_{sc}$ are compared between direct metal contact and oxide selective contact (both EBL and HBL). For each type of devices, two terminal cases of light trapping schemes are shown. One case is single pass which simulates the device assuming only one pass of solar spectrum through the device. The other case is "Yablonovitch" limit which simulates the device assuming 25 passes of solar spectrum through the device. We observe dramatic change in $V_{oc}$ and $J_{sc}$ below 20 $\mu$m absorber thickness. A zoomed-in version of the Figs. 2.9a and 2.9c is shown to the right of the corresponding figure (Figs. 2.9b and 2.9d respectively) to observe the x-axis range below 20 $\mu$m more clearly.

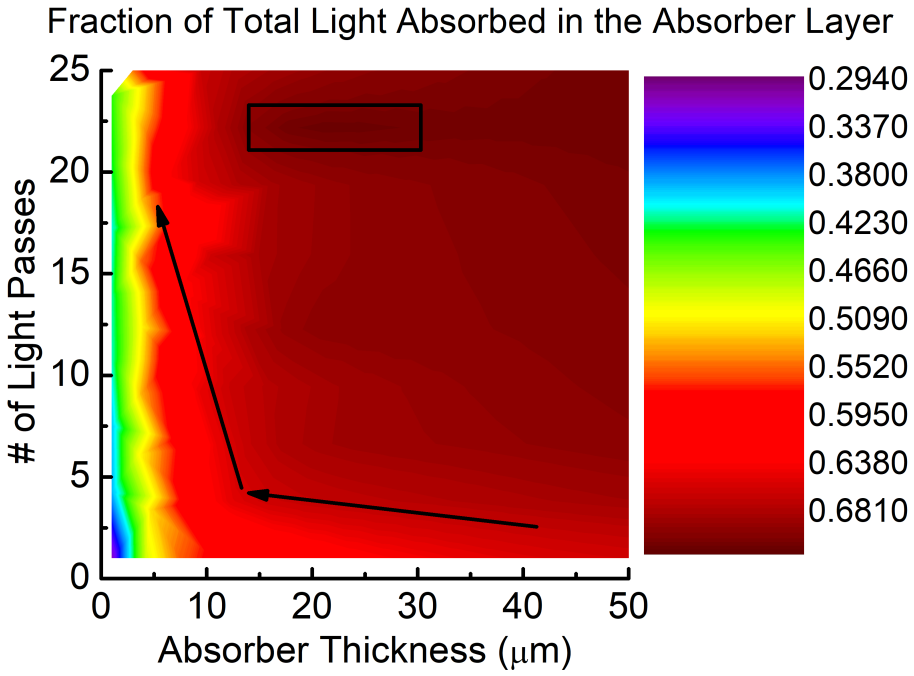


Figure 2.10: Fraction of the total solar spectra (AM1.5G) absorbed in the absorber layer of a solar cell as a function of absorber thickness and number of light passes through the cell.

We observe that $V_{oc}$ increases slightly as the thickness decreases from 120 $\mu$m. However, below 20 $\mu$m the $V_{oc}$ starts decreasing significantly. Integrating oxide selective contact can improve open circuit voltage significantly, although the shape of the curve remains same. For thicknesses below 20

$\mu$m the forward injection current over the barrier becomes significantly higher, which is responsible for the sharp decrease in $V_{oc}$. By blocking the forward injection current, oxide selective contacts can reduce the dark current that results in an increased $V_{oc}$. Note that the improvement in $V_{oc}$ from the oxide selective contact exceeds beyond that is obtained from light trapping.

$J_{sc}$ follows a different trend than $V_{oc}$ as a function of absorber thickness. Without light trapping, $J_{sc}$ starts decreasing fast when the absorber thickness is reduced. In this case, obviously a significant improvement comes from increasing the light trapping. However, the benefit of integrating oxide selective contact is also visible in $J_{sc}$. The amount of $J_{sc}$ increase is more in light trapped case compared to the case when there is no light trapping. Specifically, when the curve is zoomed below 20 $\mu$m (Fig. 2.9d), we observe the clear advantage of adding oxide selective contact to the ultra-thin solar cell having light trapping. This is because light trapping increases the carrier concentration in a thinner semiconductor film which brings more minority carriers close to the contacts. This carrier confinement due to light trapping in ultra-thin c-Si solar cells can be observed in Fig. 2.10. In this figure, the color contour represents the fraction of the total light absorbed in the variable thickness absorber layer (Fig. 2.7). The lower this fraction is, the more carriers are generated in the highly doped contact region which is subject to the surface recombination. The edge of the contours are shown with the arrow. It can be observed that when thickness decreases, the fraction decreases slightly. Roughly 20 $\mu$m thickness is when the fraction reaches its peak (shown with the black rectangle). It means that below this thickness, more light trapping will bring more minority carriers near the surface region of the cell which increases the probability of surface recombination.

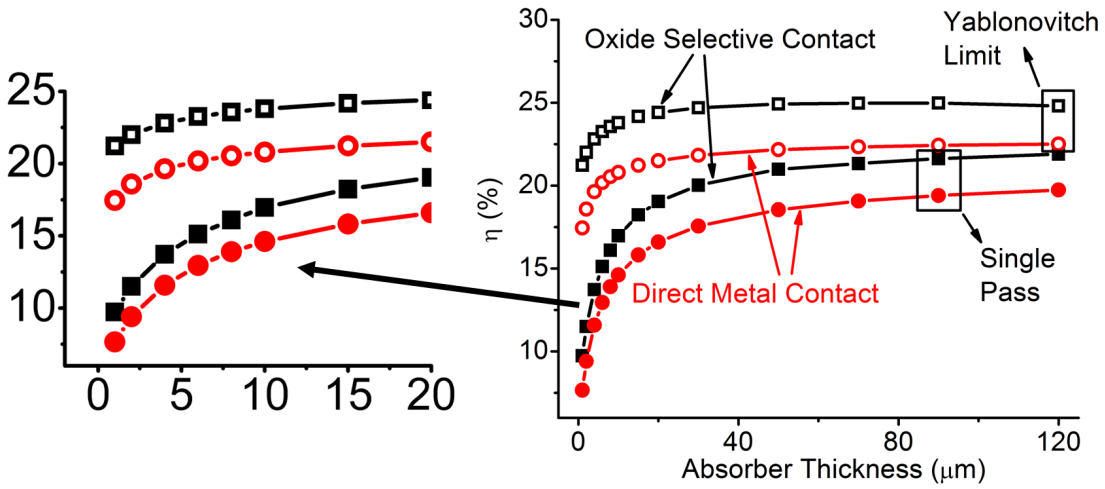


Figure 2.11: Efficiency of the c-Si solar cell as a function of absorber thickness showing comparisons between direct metal contact and oxide selective contact devices for single pass and thermodynamic light trapping case.

Finally, the efficiency is shown in Fig. 2.11 comparing direct metal contact with oxide selective

contact as a function of absorber thickness. This roughly follows Fig. 2.9c in trends. However, the zoomed in version reveals that for absorber thickness below 20 $\mu$m the benefit of incorporating oxide selective contact is significant. Specially, oxide selective contact improves the efficiency of ultra-thin cells beyond "Yablonovitch" limit of light trapping. Nevertheless, the improvement from the oxide selective contact without light trapping reaches close to the "Yablonovitch" limit near higher absorber thickness (>100 $\mu$m). This is important because it can allow us to reap the same benefit of light trapping just by improving the contacts which is a relatively cheaper process than surface texturing.

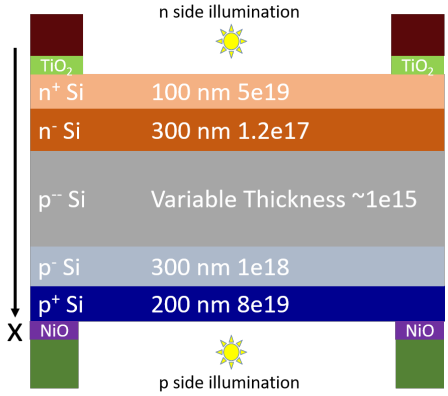


(a) Device with Oxide Contact

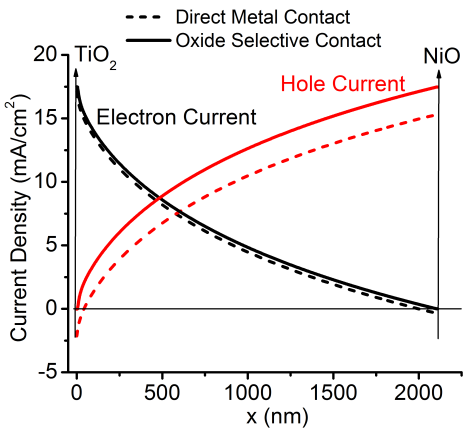


(b) Illumination from the n contact side.

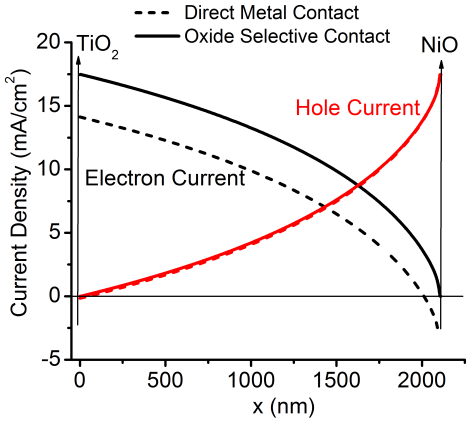


(c) Illumination from the n contact side.

Figure 2.12: Current density inside the cell as a function of distance, x (shown with the arrow), in the short circuit condition for different direction of illumination.

In order to understand the mechanism of contact selectivity enhancement from device perspective, Fig. 2.12 can be studied. In this figure, electron and hole currents are plotted separately as a function of position in the cell from one contact to the other (The direction x is shown with the arrow). The

contact edge between oxide/si is shown with the vertical line in each sub-figure. The two different sub-figures ( 2.12b and 2.12c) are shown for the illumination from n and p side respectively ( 2.12a). The UV portion of the spectra is absorbed at a shallow depth from the illumination side. This means that for a single pass of light more photo-generated carriers are generated near the contacts where the illumination is from. By simulating two different sides of illumination, we can show the effect of electron and hole selective contact separately. In Fig. 2.12b, we observe that at the $TiO_2$/Si interface, the oxide suppresses (makes it zero at the interface) the hole current that is negative. Negative hole current corresponds to the holes traveling towards the top contact (opposite to the arrow). This is the unwanted dark current that $TiO_2$ blocks as an electron blocking layer. Also, the electron current is almost same at the interface which proves that $TiO_2$ contact blocks one type of carrier (hole) and allows the other type (electron) - the definition of contact selectivity. Similarly, Fig. 2.12c shows that NiO blocks electron current which is negative meaning it was flowing in the positive x-direction towards the p type contact. At the same time, the hole current remains almost same proving its contact selectivity properties.

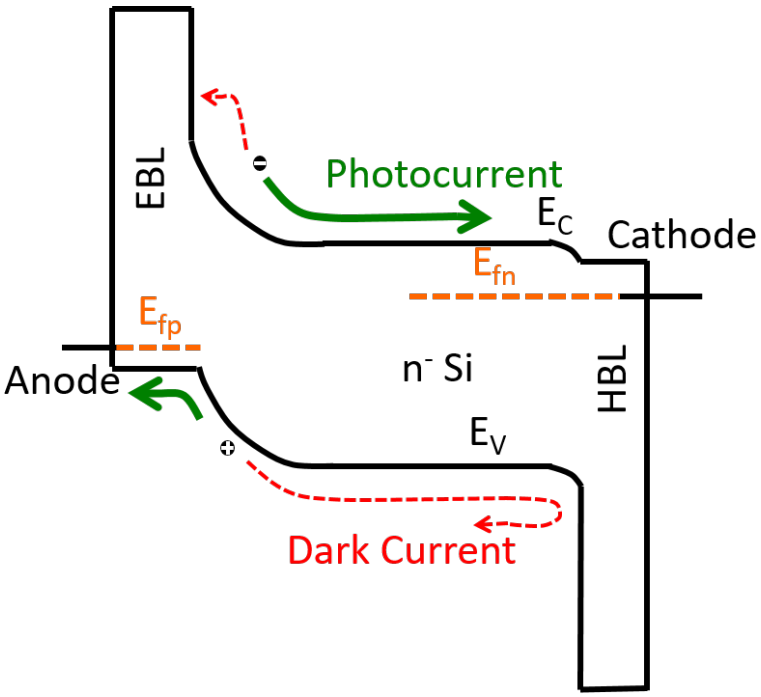


Figure 2.13: Energy band diagram of a double heterojunction solar cell with oxide selective contacts replacing high doped junctions.

In practice, the contacts are not ideal. The suppression of the minority carrier is hampered from the interface recombination due to the trap states at the oxide/silicon hetero-interface. Sometimes, oxide can have small barrier to the majority carrier due to imperfect band alignment. Nevertheless,

the basic principle of blocking the minority carrier from reaching metal/semiconductor interface remains same. These non-idealities bring the challenges of optimizing the contacts and choosing the right material. The detailed optimization of the contacts will be presented in the next chapter.

### 2.5.2 Towards a Double Heterojunction Solar Cell Replacing High Doped Homojunction

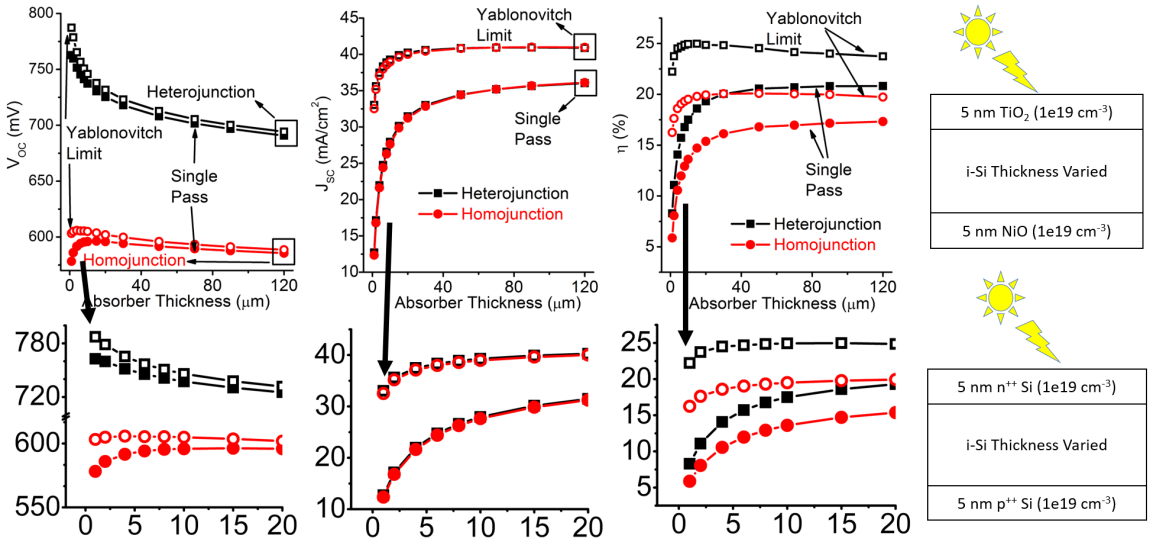


Figure 2.14: Performance comparison of the heterojunction cell with that of a homojunction cell having equal thickness of emitter and back surface field.

It is understood from Fig. 2.10 that with increasing light trapping and only the scaling of the low doped absorber layer, increasing amount of light is absorbed in the high doped contact regions. It has been shown that the carrier lifetime reduces exponentially with increasing doping [51, 52]. So, these carriers generated in the high doped region, besides subject to surface recombination, experience low bulk lifetime and high auger recombination. Specifically for ultra-thin on-chip embedded solar cells these the usable area for photo generation is limited. In this case, it is desired to design selective contacting scheme without any highly doped silicon region. Moreover, commercially available Si solar cell for power generation application requires diffusion doping which is a high temperature step ($>$ 800 °C). High temperature steps add significant cost to the manufacturing process [53] and subject the wafer to thermally induced degradation which reduces the bulk lifetime of the absorber material. If we make direct heterojunctions between oxide/low doped semiconductor then the asymmetric band offsets can separate the carriers given that the band bending inside Si absorber is like the one shown in Fig. 2.13. This is possible in two ways. First, if the oxides are perfect insulator, the metal contacts need to have right workfunction (low for HBL and high for EBL) and

the Fermi level pinning needs to be close to the corresponding band edge of Si. Second, if the oxides can be doped, the electron selective contacts need to be doped n type and the hole selective contact needs to be doped p type where the workfunction of the oxides would determine the band bending. The difference between doped heterojunction and doped homojunction is that usually doping these oxides is a low temperature process which also can provide high band offset for minority carriers and usually have high bandgap which does not absorb sunlight. In practice, direct heterojunction cells depend both on the metal contact and the doping in the oxide which will be discussed in detail in the later chapters.

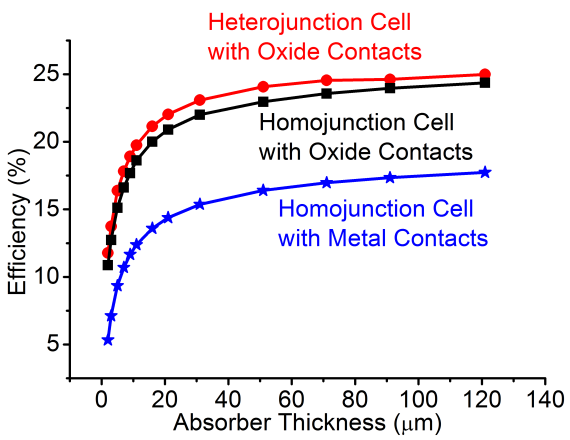


(a) Single Pass

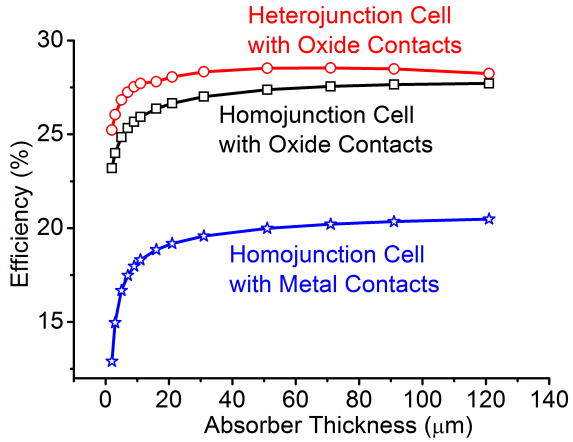


(b) Yablonovitch Limit

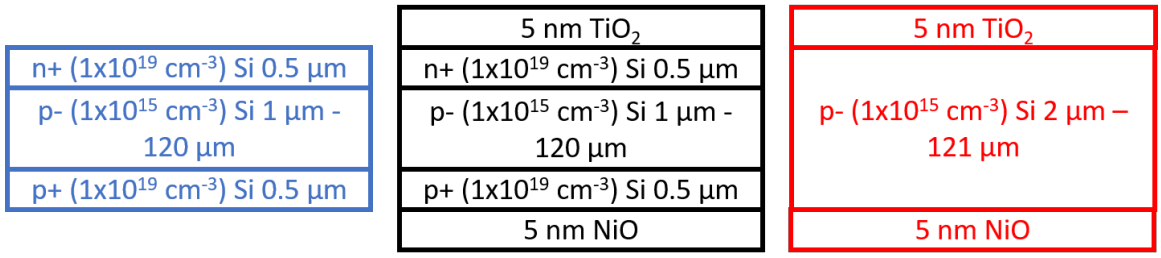


(c) The three device structures compared above

Figure 2.15: (a),(b) Summarizing the efficiency comparison between cells with (blue) homojunction cell with direct metal contact (black) homojunction cell with oxide selective contact (red) heterojunction cell with oxide selective contact, (c) the schematics of the devices compared in (a) and (b).

Fig. 2.14 shows the performance comparison of a double heterojunction cell with that of a homojunction cell having same doping and same thickness of the contact regions. Usually the thickness of the oxide selective contacts are chosen to be very thin (in the order of nanometer). So the contact regions are chosen to have the same thickness in homojunction cell also. In practice, some kind of transparent conducting oxide (TCO) like indium tin oxide (ITO) is necessary to properly ensure

the lateral conduction of the carriers. From this figure, we observe that the open circuit voltage is increased significantly in heterojunction cells. Since the high doped region in the homojunction is ultra-thin the improvement in short circuit current is not visible from the oxide selective contact. Here the band asymmetry from the oxides provide maximum suppression of the dark current which improves the $V_{oc}$ significantly. Overall the efficiency improvement is more in the case of light trapping compared to the single pass which shows the importance of better carrier management when the carrier is confined within an ultra-thin absorber layer. Also, for thicker absorber layer the surface texturing does not bring as much increase to the efficiency as can be provided from the oxide selective contact because of the thin emitter/BSF regions.

## 2.6 Conclusion

Finally to summarize the discussion in this chapter, the comparison between three solar cell structures are shown in Fig. 2.15. This figure shows the imprtance of oxide selective contact for ultra-thin c-Si solar cell. Also, it shows the importance of removing high doped junctions specifically when light trapping is used to enhance solar spectra absorption. Although the benefit of removing the high doped junction is not significant over integrating oxide selective contact on a p-n homojunction from efficiency perspective, it provides a path towards a fabrication process that is in low thermal budget which reduces the energy pay-back time and reduces the cost of fabrication. In the next chapter, we discuss the design issues of Si heterojunction solar cell having semiconducting oxide selective contacts.

# Chapter 3

# Si Heterojunction Solar Cells: A Simulation Study of the Design Issues

Silicon heterojunction solar cells having semiconducting oxide selective contacts can revolutionize the photovoltaic industry with the promise of low cost and high efficiency. In this chapter, we have identified the potential design issues of silicon heterojunction cell using simulation. This work compares two possible electron selective oxides ($TiO_2$ and ZnO) and two possible hole selective oxides ($CuAlO_2$ and NiO). The Fermi level in the oxide at the oxide/metal interface is pinned by the metal (its workfunction and eventual interface dipoles). We considered this effect, which determines the effective workfunction of the metal contact as opposed to the actual metal workfunction. Our simulation suggests that Fermi level pinning has significant impact on the device performance. We also considered different interface passivation effects and oxide dopings in our simulation. The simulation suggests that high doping in oxides is beneficial to counter balance the effect of poor surface passivation. Our work provides an extensive understanding of the design of Si heterojunction solar cell using band engineered semiconducting oxide as the selective contact replacing highly doped emitter and back surface field.

## 3.1 Introduction

A selective contact is the key component in high efficiency solar cell. Historically, a diffused p-n junction provided carrier selective contact. In this scheme, a low-doped (n or p) absorber is doped $p^{++}$ and $n^{++}$ on each side respectively along with metal contacts. The carrier selectivity is achieved through an asymmetry of carrier concentration types at the contacts from high doping. Fig. 3.1a shows a typical band diagram of such a structure, where the band bending from the doping asymmetry is responsible for the carrier separation and extraction. However, at operating

condition this structure cannot provide a high barrier to the dark current resulting from the carrier injection at forward bias. That is why, the record efficiency (∼25 %) of a p-n homojunction Si solar cell [54] is still significantly below the limiting efficiency of 29.43 % [55]. Moreover, fabricating a p-n homojunction device with dopant diffusion is a high temperature process and is one of the sources of high cost and high energy payback time [56].

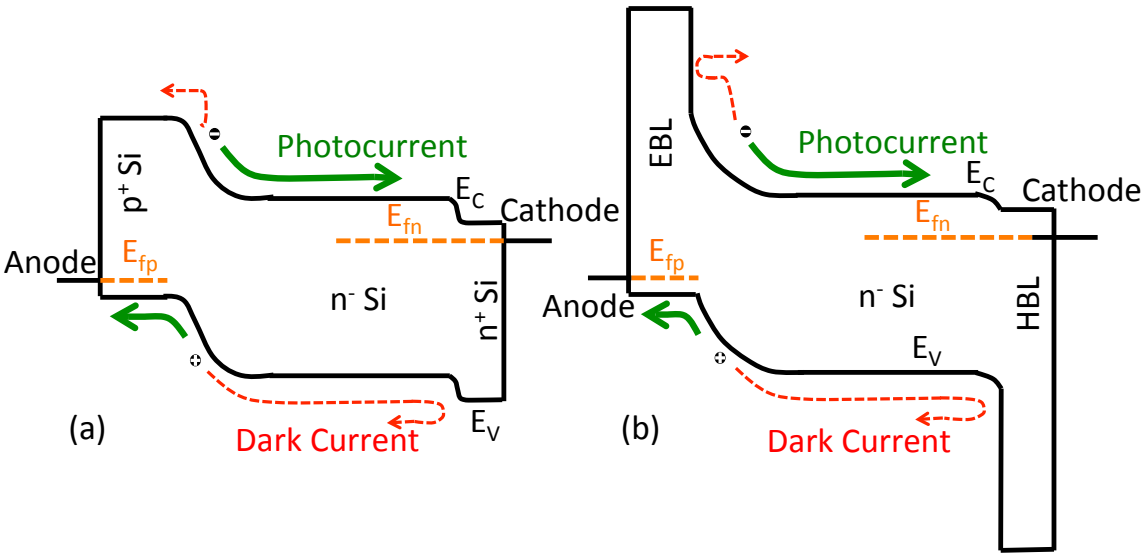


Figure 3.1: Generic energy band diagram of (a) homojunction solar cell and (b) double heterojunction solar cell having Si absorber material. EBL is Electron Blocking Layer and HBL is Hole Blocking Layer.

Simulation results suggest that band engineered heterojunctions having high band offset for one type of carrier and low for the other carrier type provides better carrier selectivity than homojunctions [57, 58]. Fig. 3.1b shows the energy band diagram of a conceptual Si solar cell where both the electron and hole selective contacts are made by heterojunctions. Contact selectivity also depends on the passivation quality of the contacts otherwise the minority carriers would recombine at the contacts resulting in high dark current. Heterojunctions of a-Si and c-Si have shown great promise due to excellent passivation quality provided by a-Si. Introduced in 1992 by Sanyo [59] as HIT$^{TM}$ cell, it holds the current record of cell efficiency of 25.6% [60]. The bandgap of a-Si is such that it still absorbs sunlight in the visible spectrum resulting in a loss of short circuit current [61]. Therefore, semiconducting metal oxides with asymmetric band offsets to Si can be viable candidates for designing selective contacts in heterojunction solar cells. These oxides replace highly doped emitter and back surface field in a homojunction cell resulting in a low temperature fabrication process. It has been shown that NiO and $TiO_2$ to be excellent candidates for hole selective and electron selective

contacts, respectively [57]. In the previous chapter, the relationship between absorber thickness and the impact of contact selectivity was discussed in detail. Numerous implementations of such devices have been reported in the literature [62, 63, 64, 65, 66, 67, 68], in which, $TiO_2$ [62] and $LiF_x$ [66] are used as an electron selective contact and $MoO_x$ [64, 66, 65], PEDOT:PSS [63] and $WO_x$ [67, 68] as a hole selective contact. Some of the materials ($LiF_x$, $MoO_x$) implemented do not have a band offset that is suitable as a selective contact. The only way these materials work is by creating a defect band near the valence or the conduction band of Si [64].

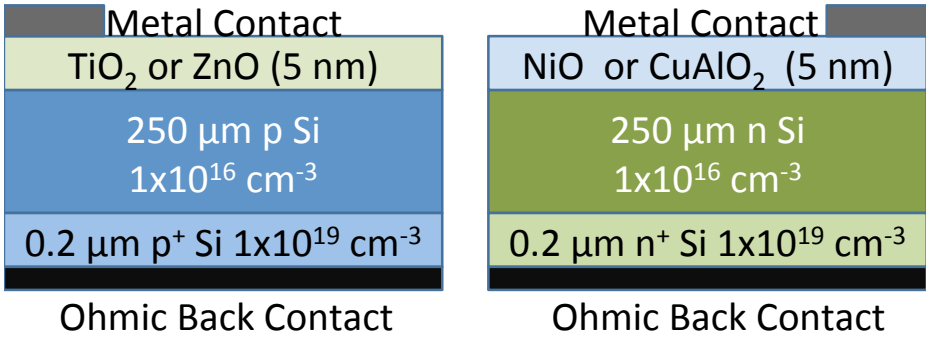


Figure 3.2: Schematic of the device structure studied in this paper. Electron selective contacts and hole selective contacts are studied separately with respect to p and n Si respectively so that the heterojunction becomes the carrier separating junction.

Non-idealities in these oxides and oxide/Si interface are a bottleneck in implementing heterojunction solar cells. Most importantly, Fermi level pinning at the metal/oxide interface which creates a Schottky barrier, needs to be considered properly. The built-in potential of a homojunction cell is determined by the Fermi level difference between the high doped emitter and the back surface field. Also the highly doped Si makes the contact resistance not a significant roadblock in designing Si homojunction cells. For oxide/Si heterojunctions, doping of the oxide and Fermi level pinning both will be important factors in determining barriers for both minority and majority carriers. The effect of non-ideal TCO workfunction on silicon heterojunction cell has been studied previously [69]. However, a small band offset at the majority carrier side poses more stringent design requirement for choosing the right metal workfunction and oxide doping. Therefore, proper design optimization taking Fermi level pinning into account is necessary. In this chapter, the optimization of selective contact considering Fermi level pinning and interface passivation will be presented in detail. Besides understanding the design constraints, this work will provide a reasonable metric for evaluating different materials for carrier selective properties. However, various materials properties and process-related issues as well as degradation effects are not covered by the idealized approach presented in this simulation study. The contact optimization work presented here is based on simulation study done using AFORS-HET simulation software [70]. The details of the simulation and the material

parameters of the oxides considered in this chapter has been presented in the previous chapter.

## 3.2 Details of Simulation

Fig. 3.2 shows the device structure simulated in this work. The oxides were simulated as wide bandgap semiconductors with the parameters taken from the published literature (see table 2.1). Direct tunneling through the 5 nm oxide is ignored. To evaluate the oxides as contacts forming carrier separating junctions, two separate device structures are considered for the electron selective and the hole selective contact. This allows us to optimize one type of contact independently without the influence of other. Therefore, we simulated four one-sided Si heterojunction solar cells; in two of them 5-nm thick, p-doped NiO and $CuAlO_2$ were used as the hole-selective contacts while 0.2 $\mu$m, highly n-doped Si was utilized as the electron-selective contact for a 250 $\mu$m thick, n-doped Si absorber (Fig. 3.2). In the other two solar cells, 5 nm thick, n-doped ZnO and $TiO_2$ were utilized as the electron-selective contacts while 0.2 $\mu$m, highly p-doped Si was used as the hole-selective contact for a 250 $\mu$m thick, p-doped Si absorber (Fig. 3.2). The focus of this simulation study is to optimize the heterojunction contacts and therefore thick absorber layer is considered to decouple the effect of the bottom contact from the top. However, similar simulation performed for ultra-thin absorber material provides the same conclusion with regards to contact optimization.

In practical implementation usually these oxides are used along with some TCOs (e.g. ITO, Ag nanowire etc.) to allow sufficient lateral conduction. In this situation the metal contact is made with the oxide through the TCO. Therefore it might seem that the results presented in this work are not applicable when there is a TCO present between the metal and the oxide. However, the TCOs are also subject to Fermi level pinning and this study is applicable to the contact between TCO and carrier selective oxide. Moreover, in case when the junction is formed in the back of the solar cell, specially in all back contact solar cell, TCOs are not required. In that situation this work is of great importance and could provide a guide for designing the contacts effectively. The effect of non-ideal lateral conduction in TCO is an addition to the series resistance to the light I-V response. We have ignored it deliberately, in order to study the effect of Fermi level pinning properly because it also causes an addition of series resistance and sometimes introduce extraction barrier to the carrier being extracted out of the contact.

No optical losses due to the top surface reflection is taken into account. However, the Si absorber is considered to absorb the spectra based on its absorption coefficient at a certain wavelength. At the bottom contact, $\phi_M$ is assumed such that it behaves as an ohmic contact. The top contact is where the Fermi level pinning of metal on oxide is considered and $\phi_{M,eff}$ is set as a simulation parameter which determined the boundary condition. The non-ideal surface passivation is simulated assuming a constant defect distribution along the bandgap of the oxide overlapping with that of the Si.

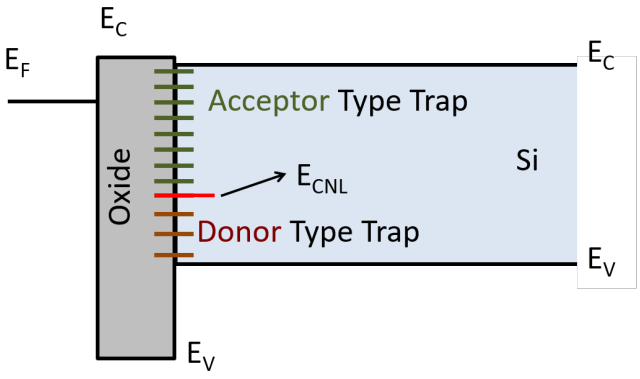


Figure 3.3: Schematic of the interface defect distribution considered in this work.

### 3.2.1 Interface Trap Distribution

We assume a constant defect distribution along the bandgap of Si at the oxide/Si interface according to the following equation,

$$N_{trap}(E) = \left(E_{trap}^{end} - E_{trap}^{start}\right) N_{trap}^{const} \vartheta \left(E - E_{trap}^{end}\right) \vartheta \left(E_{trap}^{start} - E\right) \tag{3.1}$$

Here, $E_{trap}^{start}$ and $E_{trap}^{end}$ denotes the start and end energy of the energy interval within the bandgap where a constant defect density is assumed, $N_{trap}^{const}$ denotes the constant defect density per energy and $\vartheta(E)$ is the step function.

The character of the defects switches from donor type to acceptor type at the $E_{CNL}$ of Si as we move from the valence band towards the conduction band (Fig. 3.3). We vary $N_{trap}^{total}$ from $10^{10}$ cm$^{-2}$ to $10^{13}$ cm$^{-2}$. The surface lifetime ($\tau_s$) is related to the defect density as,

$$\tau_{s,n/p} = \frac{1}{\sigma_{n/p} \upsilon_{th} N_{trap}^{total}} \tag{3.2}$$

Here, $\sigma_{n/p}$ corresponds to the capture cross-section of electrons (n) or holes (p), $\upsilon_{th}$ is the thermal velocity of the carriers. This corresponds to the surface lifetimes ($\tau_s$) of 1 ms, 100 $\mu$s, 10 $\mu$s and 1 $\mu$s respectively at the metal oxide/Si interface assuming electron/hole capture cross section of the defect is $10^{-14}$ cm$^2$. The effective lifetime ($\tau_{eff}$) is related to the bulk lifetime ($\tau_b$) and the surface lifetime ($\tau_s$) as,

$$\frac{1}{\tau_{eff}} = \frac{1}{\tau_b} + \frac{1}{\tau_s} \tag{3.3}$$

Since $\tau_b$ is assumed to be 10 ms, the effective lifetime is mostly dominated by $\tau_s$. Constant defect density is a simplified picture. However for qualitative comparison, this is sufficient.

The effects of metal oxide doping, surface passivation at the metal oxide-Si interface and also the

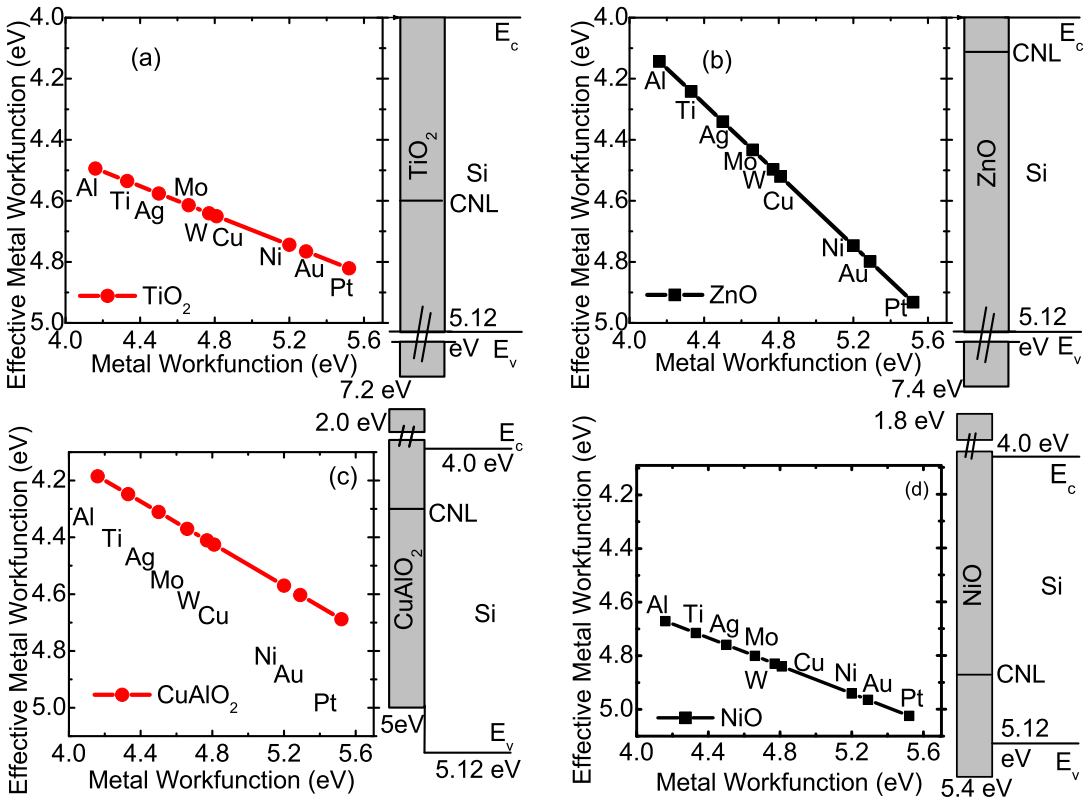


Figure 3.4: Effective metal workfunction determined from Eq. 2 as a function of metal workfunction in (a) $TiO_2$ (b) ZnO (c) $CuAlO_2$ (d) NiO. The relative band offsets of oxides to Si (not to scale) and the position of the metal pinning level are also shown. The relevant material parameters are tabulated in table 2.1.

metal work function of the metal contact at the metal oxide side were investigated. We simulated the performance of the solar cell for metal oxide dopings of $10^{17}$, $10^{18}$, $10^{19}$, $10^{20}$ $cm^{-3}$. Different metal work functions at the metal oxide end were also simulated to evaluate the performance of different metals that we can use at the metal oxide contact.

## 3.3 Fermi Level Pinning

Ideally, barrier height seen by the carriers (electrons/holes) from the band bending at an MS junction is determined by the metal workfunction, $\phi_M$, and the semiconductor workfunction, $\phi_S$, determined by the semiconductor doping. However, metal induced gap states (MIGS) are created by the electron wavefunction in metal penetrating into the bandgap of the semiconductor [71]. This causes a dipole charge to be formed at the interface. In equilibrium, metal Fermi level ($E_{FM}$) moves close to the charge neutrality level ($E_{CNL}$) of the semiconductor, a point where the MIGS switch their

characteristics from donor-like to acceptor-like in order to minimize the overall dipole charge. This causes the barrier height for a particular MS junction less sensitive to the metal workfunction, a phenomenon known as Fermi level pinning. How strongly $E_{FM}$ will be pinned towards $E_{CNL}$ is determined by the empirical parameter pinning factor (S) defined as [72],

$$S = \frac{\partial \phi_B}{\partial \phi_M} = \frac{1}{1 + 0.1\,(\varepsilon_\infty - 1)} \tag{3.4}$$

Here, $\varepsilon_\infty$ is the high frequency dielectric constant of the semiconductor and $\phi_B$ is the barrier height at the MS interface. Effective metal workfunction, $\phi_{M,eff}$, of a pinned MS junction is therefore given by,

$$\phi_{M,eff} = S\phi_M + (1 - S)\,\phi_{CNL} \tag{3.5}$$

where $\phi_{CNL}$ is the position of the charge neutrality level with respect to the vacuum.

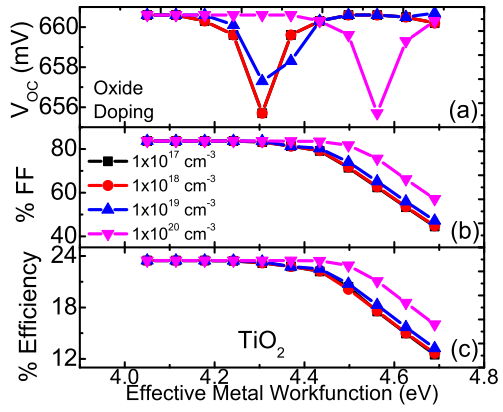


(a) $TiO_2$

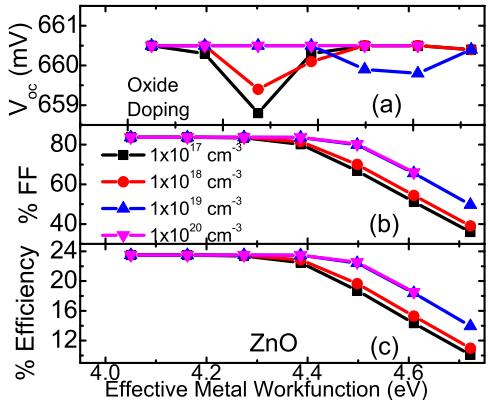


(b) ZnO

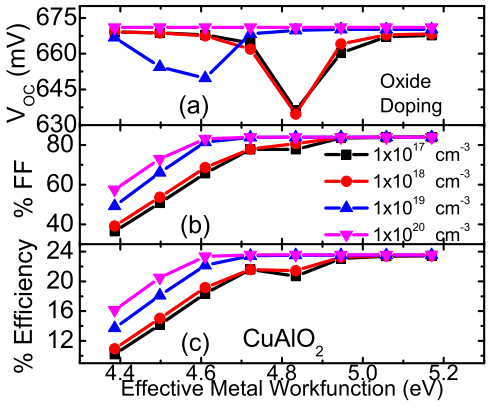


(c) $CuAlO_2$

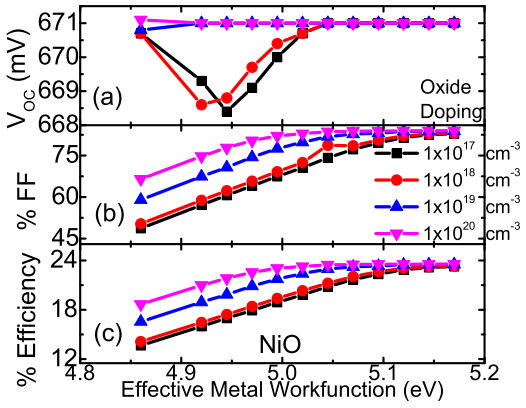


(d) NiO

Figure 3.5: Cell performance ((a) $V_{oc}$ (b) % FF (c) % Efficiency) as a function of effective metal workfunction for the oxides studied in this work.

### 3.3.1 Electron-Selective Contacts

Previously reported values of $\phi_{CNL}$ and S [43] for the studied semiconducting oxides are used to calculate $\phi_{M,eff}$ of different contact metals for the heterojunction solar cell and are shown in Fig. 3.4. The Fermi level pinning at the metal/oxide interface leads to an effective metal workfunction, i.e. the $\phi_{M,eff}$ is a joint property of the metal in contact with the oxide, not the property of the oxide alone. Corresponding schematic band alignment of oxide and Si is shown to the right of each plot of effective metal workfunction to provide a visualization of the effective barrier that will be formed for different types of metals. The effect of workfunction on the ideal device performance (perfect surface passivation) for different oxide doping is shown in Fig. 3.5. First thing to note here is that the maximum $V_{OC}$ is 660 meV. However, a-Si passivated solar cells show $V_{OC}$ greater than 700 meV [60]. This discrepancy is because of using a doped Si homojunction as back surface field (BSF). Doped a-Si readily achieves very high dopant concentration. We have assumed a doping of $1 \times 10^{19}$ $cm^{-3}$ for the BSF in our simulation. If the doping of $1 \times 10^{20}$ $cm^{-3}$ is assumed for the BSF instead, the $V_{OC}$ is greater than 700 meV according to our simulation. Nevertheless, If we observe Fig. 3.4 and 3.5 together, we would find some constraint for each oxide. Fig. 3.4a reveals that the lowest $\phi_{M,eff}$ that we can expect from $TiO_2$ is 4.5 eV for the commonly used metal aluminum. Around that $\phi_{M,eff}$, the device performance (Fig. 3.5) is degraded because of the high barrier seen by electrons. Comparatively, ZnO can provide much lower $\phi_{M,eff}$ ($\sim$4.1 eV in Fig. 3.4b), which ensures the best device performance for a range of doping in ZnO. Higher effective barrier adds to the overall series resistance of the device degrading the fill factor (% FF). ZnO can provide lower effective barrier to electrons than $TiO_2$, because the charge neutrality level lies much closer to the conduction band in ZnO, and it has a higher pinning factor (S = 0.58) than $TiO_2$ (S = 0.24) that gives it more control to change the barrier height by changing $\phi_M$. It is also observed that devices having low oxide doping suffer the most. This can be attributed to the fact that Schottky barrier thickness increases as the doping is reduced. Moreover, higher doping in the oxide causes the charge to screen the effect of metal Fermi level pinning. This means that the effect of non-ideal metal Fermi level diminishes with higher doping in the oxide where the oxide Fermi level determines the built-in potential. Since the barrier thickness is narrow in highly doped oxide, whatever barrier that is formed between the oxide and the metal has an insignificant effect .

### 3.3.2 Hole Selective Contacts

Fig. 3.4c and 3.4d show $\phi_{M,eff}$ achievable for the hole selective contacts $CuAlO_2$ and NiO. If we look at the band offset diagram, we can see that the comparison here is not that straightforward. The reason is NiO has a positive valence band offset (VBO) with Si (valence band of NiO lies lower than that of Si) whereas $CuAlO_2$ has a negative valence band offset (valence band of $CuAlO_2$ lies higher than that of Si). Literature also suggests a range of NiO bandgap [73], which makes it difficult to pinpoint a single value to use in simulation. This positive VBO in NiO creates an

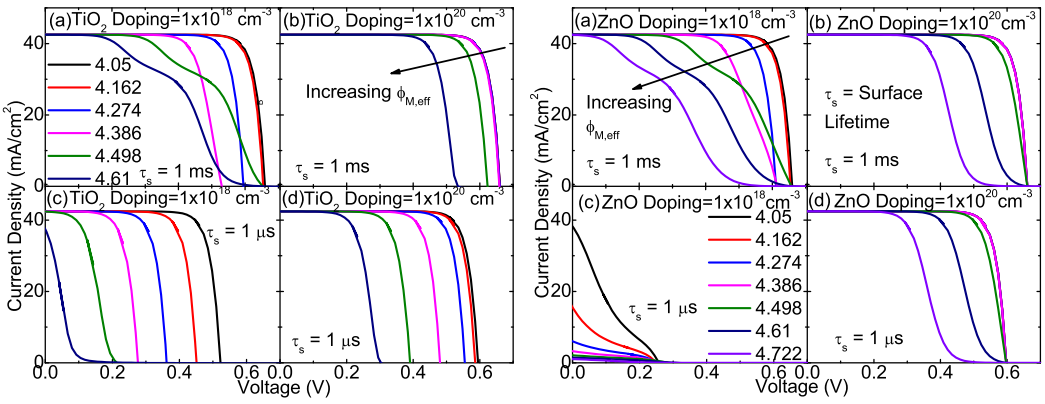


(a) $TiO_2$ (b) ZnO

Figure 3.6: $TiO_2$ and ZnO heterojunction cell light I-V response at AM 1.5G spectrum for different metal workfunctions, interface passivation and oxide dopings.

additional extraction barrier for the hole. However, the presence of no additional barrier from VBO in $CuAlO_2$ does not help much because its $E_{CNL}$ lies farther away from the valence band resulting in the highest $\phi_{M,eff}$ to be around 4.7 eV. This causes a high barrier for holes and around that value the performance starts to degrade. For NiO, the pinning situation is much better as it can ensure a high $\phi_{M,eff}$ ($\sim$5 eV in Fig. **??**). However, the additional barrier caused by the positive VBO affects carrier extraction. Nevertheless, we have assumed a conservative value of VBO between NiO and Si. In practice the bandgap of NiO can be engineered by varying the deposition condition [74] resulting in the tuning of VBO.

## 3.4 Effect of Interface Defects

Interface trap states, $D_{it}$, play a significant role in determining the effectiveness of the selective contacts. Fig. 3.1b shows the band diagram of a double heterojunction cell with the directions of different current components. The high band offset is supposed to suppress the injected dark current. However, if that interface has a high density of $D_{it}$ in the midgap region, instead of getting reflected at the high band offset barrier, the minority carrier recombines at the interface. The recombination current flows in the direction opposite to that of the photocurrent resulting in increased dark current. As a result $V_{OC}$ drops since it depends on the ratio of the photocurrent and the dark current. In effect, poor surface passivation can defeat the whole purpose of using band engineered oxide heterojunction as the selective contacts because it will provide an additional path for the dark current to flow. In this section, we will determine the effect of interface passivation and explore its interaction with other design constraints.

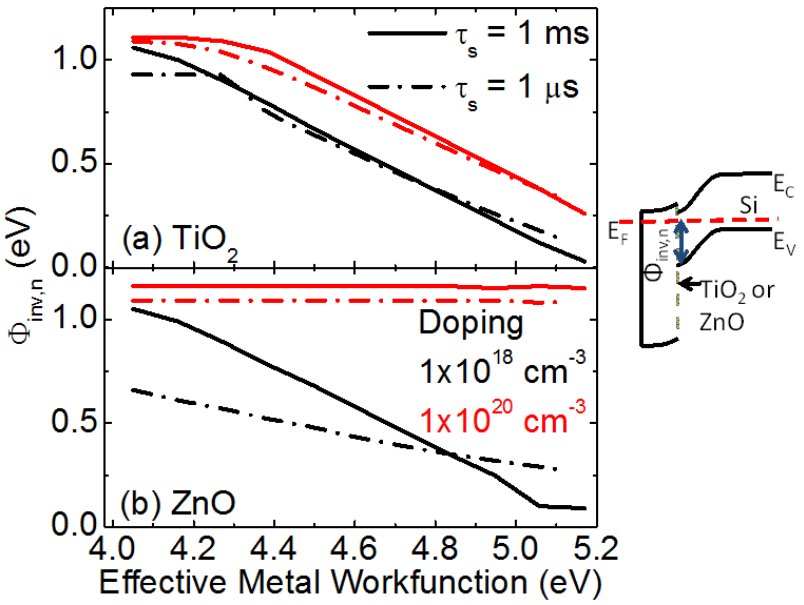


Figure 3.7: Difference between Fermi level and valence band edge at the oxide/Si interface in equilibrium for $TiO_2$ and ZnO heterojunction cell under AM 1.5G spectrum.

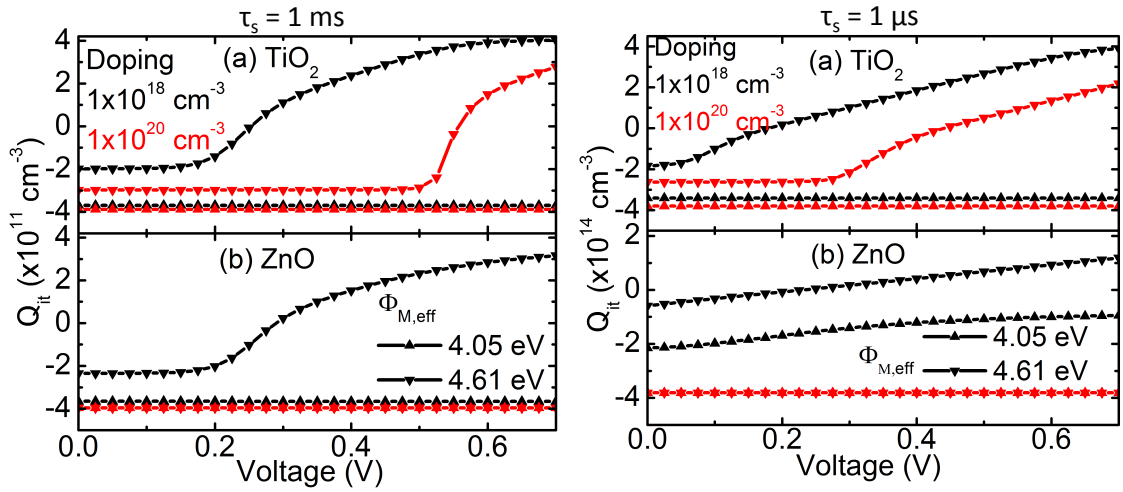


Figure 3.8: Charge density stored in the interface trap states as a function of voltage. Both $TiO_2$ and ZnO electron selective contacts have been compared for different dopings, interface passivation and $\phi_{M,eff}$.

### 3.4.1 Electron Selective Contact

Fig. 3.6 compares the light I-V response for the electron selective contacts for different $\phi_{M,eff}$, interface passivation ($\tau_s$) and oxide doping. This figure suggests that high doping can compensate

some of the drastic effects of poor interface passivation. This can be explained by Fig. 3.7, which shows the difference between Fermi level and the valence band edge at the interface in thermodynamic equilibrium ($\phi_{inv,n}$) in dark condition. The thermodynamic equilibrium signifies the device condition after junction formation with no external excitation (light or bias). This metric corresponds to the overall band bending of the junction due to the asymmetry of carriers in the heterojunction.

From the device physics point of view, $V_{OC}$ represents a point where the band bending is such that the forward injection current (source of dark current) is equal to the photocurrent (flowing in opposite direction). Higher band bending at the thermodynamic equilibrium causes the $V_{oc}$ point to occur at higher voltage. It has recently been shown that the carrier separation at the selective contacts and hence the $V_{oc}$ is governed by the conductivity difference for holes and electrons at the contacts [58]. Band bending at the thermodynamic equilibrium determines the conductivity near the contact region. Therefore, $\phi_{inv,n}$ effectively determines the overall performance of the device. From Fig. 3.7, we can see that high oxide doping increases $\phi_{inv,n}$ and makes it insensitive to $\phi_{M,eff}$ for ZnO. For $TiO_2$, $\phi_{inv,n}$ decreases with $\phi_{M,eff}$. This is because $TiO_2$ has a very high relative dielectric constant (∼86) compared to ZnO (∼7). So high doping does not screen the electric field resulting in band bending dependent on metal workfunction. This effect is also manifested in Fig. 3.6, where we see that $V_{OC}$ in $TiO_2$ cell is more sensitive to metal workfunction than that in ZnO even at high doping.

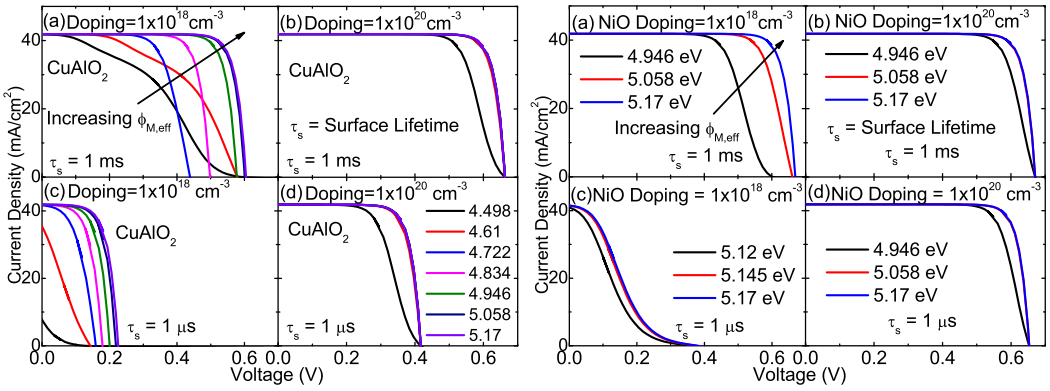


(a) $CuAl_2$ (b) NiO

Figure 3.9: $CuAlO_2$ and NiO heterojunction cell light I-V response at AM 1.5G spectra for different metal workfunctions, interface passivation and oxide dopings.

We see a distinct kink and overall S-shaped I-V in low-doped oxide for high $\phi_{M,eff}$. The two main causes of this s-shape are the presence of a barrier for majority carrier extraction and the charge stored in $D_{it}$ given by the following equation,

$$Q_{it} = \varepsilon_0 \varepsilon_r^{oxide} \left.\frac{\partial \phi(x)}{\partial x}\right|_{x_{it}^{oxide}} - \varepsilon_0 \varepsilon_r^{Si} \left.\frac{\partial \phi(x)}{\partial x}\right|_{x_{it}^{Si}} \tag{3.6}$$

Here, $\varepsilon_r^{oxide}$ and $\varepsilon_r^{Si}$ represent the relative dielectric constant of oxide and Si respectively. Also, $x_{it}^{oxide}$ and $x_{it}^{Si}$ denotes the oxide/Si interface from the oxide side and the Si side respectively to account for the discontinuity of the electric field at the interface. $Q_{it}$ is plotted as a function of voltage for different oxide doping and surface passivation in Fig. 3.8. From this figure, we can get a comparative picture between $TiO_2$ and ZnO based on their stark difference in dielectric constant. High-k $TiO_2$ changes the $Q_{it}$ distribution rapidly as a function of gate voltage. Especially for a high $\phi_{M,eff}$ at low oxide doping, the Fermi level at the interface moves as the voltage changes. This changes the amount and the type of charge stored in $D_{it}$. The voltage where this occurs shows up as a kink in the I-V characteristics. For high doping in oxide, change in voltage is screened by the dopant charge and the Fermi level at the interface remains constant and hence the $Q_{it}$ remains constant. Therefore, at high oxide doping we do not see a significant kink in the I-V characteristics. For a high-k oxide like $TiO_2$, the voltage change at the metal terminal can still have an affect on the Fermi level at the interface. This can affect the cell performance based on the interface passivation. If the interface passivation quality is good, the effect of non-ideal (high for electron selective contact) metal workfunction needs to be kept as low as possible. In that case, both low-k dielectric and high doping are beneficial. We can see this clearly by comparing Fig. 3.6a and 3.6b for both $TiO_2$ and ZnO. If the interface passivation quality is poor, it can be compensated by choosing a combination of metal workfunction, dielectric constant and doping of the oxide in such a way that the $Q_{it}$ crossover does not appear in the voltage range of interest. Only charge stored in the interface defect states can not completely explain the S-shape seen in Fig. 3.6. When $\phi_{M,eff}$ increases, Schottky barrier height at the contact increases resulting in an increased barrier for majority carrier extraction. These non-extracted majority carriers recombine at the interface causing S-shaped I-V. The S-shape disappears when the oxide doping increases, which reduces the space charge region and enhances the internal electrical field.

### 3.4.2 Hole Selective Contact

Fig. 3.9 compares I-V response under illumination for hole selective contacts for different $\phi_{M,eff}$, $\tau_s$ and oxide doping. There is a 0.23 eV valence band offset between NiO and Si [75]. Therefore holes in Si see a barrier of 0.23 eV when extracted. This poses a strict limit on the allowable $\phi_{M,eff}$. Since we have not taken tunneling into account, the simulation convergence becomes an issue when $\phi_{M,eff}$ becomes too low. $CuAlO_2$ on the other hand has a slight negative band offset ($\sim$-0.12 eV) with Si (Fig. 3.4c). This makes the carrier extraction from Si to $CuAlO_2$ easier than NiO. However, doping in oxides still plays a significant role specifically for low workfunction metals. This is because in $CuAlO_2$ $E_{CNL}$ lies far away from the valence band edge and it is hard to reduce the barrier between metal and oxide. Even a high workfunction metal Pt pins 0.3 eV away from the valence band edge.

Only the band offset consideration should not dictate the choice of a contact material (oxide and metal). This also depends on pinning and doping of the oxide. The most important point here is

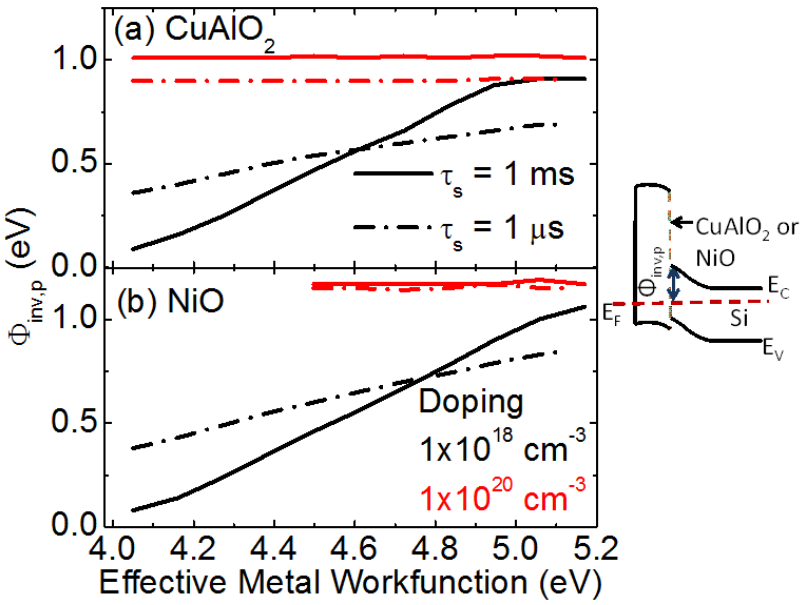


Figure 3.10: Difference between Fermi level and valence band edge at the oxide/Si interface in equilibrium for $CuAlO_2$ and NiO heterojunction cell under AM 1.5G spectrum.

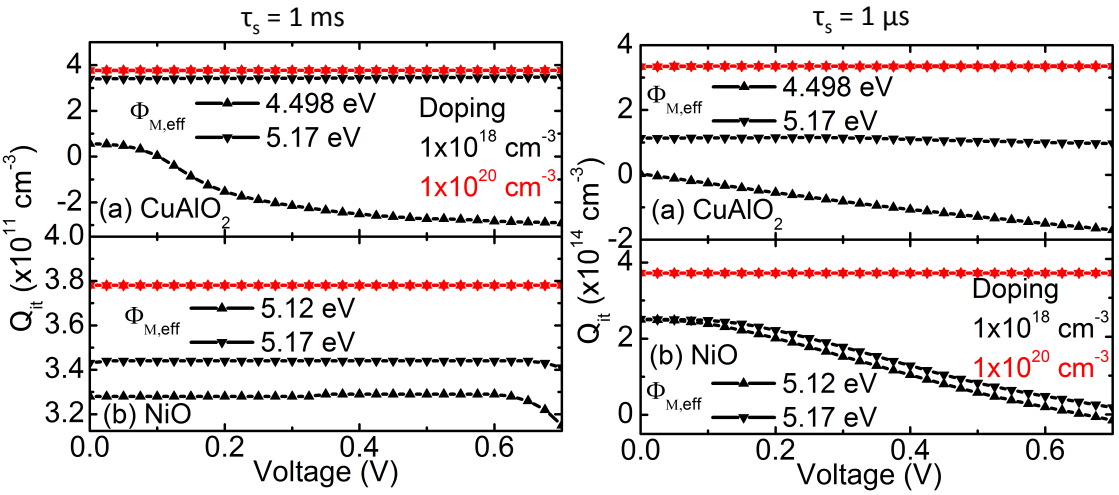


Figure 3.11: Charge density stored in the interface trap states as a function of voltage. Both $CuAlO_2$ and NiO hole selective contacts have been compared for different dopings, interface passivation and $\phi_{M,eff}$.

the drastic reduction of $V_{OC}$ when the interface passivation is poor in $CuAlO_2$/Si interface even at a high doping. In order to explain this we look at Fig. 3.10, which shows the difference between the Fermi level and conduction band edge at the interface in equilibrium ($\phi_{inv,p}$). This figure represents

the extent of inversion at the interface when the heterojunction is formed. From this figure, we observe that for $CuAlO_2$, $\phi_{inv,p}$ decreases significantly when the surface passivation becomes poor (Fig. 3.10a red solid and dotted line) for highly doped oxide. No reduction is seen for NiO. This is due to the small positive valence band offset between NiO and Si, which cause a triangular well for holes to accumulate at the equilibrium. Because of these accumulated holes, the band bending remains high irrespective of the interface passivation. Therefore a slight positive band offset might be useful depending on whether the oxide can be doped and the Fermi level pinning is such that very low barrier height is possible from the metal side. However, such an offset should be carefully engineered as the accumulated majority carrier account for a possible s-shaped I-V characteristics. Also, doping in these oxides induces trap levels near the band edge resulting in an increase in trap assisted tunneling which can improve the contact selectivity. Previous simulation suggests that high doping in oxide can provide additional band bending resulting in a reduction in the tunnel barrier thickness [76]. Therefore, our simulation not including tunneling is a conservative estimate of the device performance.

Fig. 3.11 shows $Q_{it}$ as a function of voltage for different hole selective contacts. Similar to electron selective contacts, the figure suggests that kink in the I-V response to light for low $\phi_{M,eff}$ can be explained using the crossover of $Q_{it}$. The voltage where the crossover occurs corresponds to the voltage where kink appears. For low-doped oxide with good surface passivation this crossover occurs in the usable voltage range and is visible. For poor surface passivation, this crossover occurs outside of the voltage range between short-circuit and open-circuit. Hence the kink is not visible. However, the usual shape of I-V response is altered and a slight S-shape is seen. For high oxide doping, S-shape is not visible as the Fermi level at the interface between oxide and semiconductor changes only slightly as a function of voltage.

## 3.5 Conclusion

In this chapter, a thorough understanding of the design and optimization of heterojunction solar cells using semiconducting oxides as selective contact is presented. Our simulations suggest that the surface passivation and metal/oxide barrier height play important roles in determining the performance of such devices. However, proper design considering the aspects of selective contacts is the key to replace high doped emitter and back surface field used in traditional Si homojunction cell. Specifically:

1. Besides band offset, the Fermi level pinning properties of the oxides need to be taken into account, requiring $E_{CNL}$ to lie close to one of the band edges and it should have relatively high pinning factor.

2. High-k oxides allow the electric field at the oxide/Si interface to be influenced by the metal

workfunction more than the low-k oxides. So high-k oxides are affected by the non-ideal metal workfunction more than the low-k oxides.

3. High doping in oxides is beneficial to counter balance the effect of poor surface passivation. Low doping can cause S-shaped I-V for non-ideal metal workfunction.

4. The ideal band offset for the majority carrier is supposed to be zero. However, if it is negative, it can provide low barrier to carrier extraction but impacts $V_{oc}$. If it is positive, it can provide some barrier to the carrier flow, but it can cause higher inversion at the interface resulting in high $V_{oc}$. The exact value of the band offset that is tolerable is determined by the effective metal workfunction, doping of the oxide and the relative improvement in $V_{oc}$.

# Chapter 4

# Tuning Electrical Properties of Nickel Oxide using UV/ozone Treatment

Drastic reduction in nickel oxide ($NiO_x$) film resistivity and ionization potential is observed when subjected to ultraviolet (UV)/ ozone ($O_3$) treatment. X-ray photoemission spectroscopy suggests that UV/$O_3$ treatment changes the film stoichiometry by introducing Ni vacancy defects. Oxygen-rich $NiO_x$ having Ni vacancy defects behaves as a p type semiconductor. Therefore, in this work, a simple and effective technique to introduce doping in $NiO_x$ is shown. Angle resolved XPS reveals that the effect of UV/$O_3$ treatment does not only alter the film surface property, but also introduces oxygen-rich stoichiometry throughout the depth of the film. Finally, simple metal/interlayer/semiconductor (MIS) contacts are fabricated on p type Si using $NiO_x$ as the interlayer and different metals. Significant barrier height reduction is observed with respect to the control sample following UV/$O_3$ treatment, which is in agreement with the observed reduction in film resistivity. From an energy band diagram point of view, the introduction of the UV/$O_3$ treatment changes the defect state distribution resulting in a change in the pinning of the Fermi level. Therefore, this work also shows that the Fermi level pinning property of $NiO_x$ can be controlled using UV/$O_3$ treatment.

## 4.1 Introduction

Binary metal oxides offer versatile applications in flexible electronics [77], solar photovoltaics [62, 63, 64, 65, 66, 67, 68], sensors [78], display technology [77] and memory technology [79, 80, 81]. Transition metal oxides are desirable in these applications because of their transparency, robustness, ability to be deposited on a variety of substrates and varied semiconducting (both p and n) properties. Most of these oxides (e.g. $TiO_2$, ZnO, $SnO_2$, $Cu_2O$, NiO) show semi-insulating properties in perfect stoichiometry. However, a slight deviation from the stoichiometry introduces native defects

(e.g. vacancies or interstitials) contributing electrons or holes to the lattice system. For example, formation of oxygen vacancies is energetically favorable in oxides like $TiO_2$ and ZnO. An oxygen-deficient stoichiometry is believed to be the reason for n type semiconducting properties in these oxides [43]. On the other hand, NiO and $Cu_2O$ exhibit the opposite behavior, i.e. these oxides tend to exhibit p type behavior as a result of an oxygen-rich stoichiometry [43]. In NiO, oxygen-rich stoichiometry results in the formation of nickel vacancies, not the oxygen interstitials [82]. In order to maintain charge neutrality near the Ni vacancy site, two $Ni^{2+}$ ions lose an extra electron each to form $Ni^{2+}$. Thus a quasi-localized pair of holes is generated for each Ni vacancy causing p type behavior [83, 84].

Controlling Ni vacancy defects in NiO lattice would enable us to control its resistivity and transport properties, which can be useful in various applications. For example, in resistive-RAM (RRAM), this can improve the switching characteristics of the device [85]. Also, the formation of Ni vacancy defects can introduce localized states near the valance band and lower the hopping transport barrier for holes resulting in an increase in hole mobility - a phenomenon desired in flexible substrate thin film transistors (pMOS). Nickel oxide is also a potential candidate for p type carrier selective contacts with Si. The high conduction band offset, low valence band offset, and depinning of the Fermi level with Si, which have been demonstrated [49], can provide a contact that allows hole transport while blocking electron transport. Recently, reports of band engineered metal oxides as selective contacts to heterojunction Si solar cell have created an effective way to design future generation solar cells at lower cost and lower thermal budget [62, 63, 64, 65, 66, 67, 68]. In this application, controlling the resistivity of the oxide selective contact is very important to optimize the device design. It has been shown by simulation that higher doping density in the oxides in heterojunction solar cell can effectively compensate for negative effects of poor interface passivation [86]. Ultraviolet (UV)/ ozone ($O_3$) treatment has been used to modify the surface properties of thin films [87, 88, 89]. Specially Wang *et al.* demonstrated that UV/$O_3$ treatment to nickel acetate anode buffer layer can significantly improve the open circuit voltage in polymer solar cells [87].

In this chapter, we have demonstrated that post deposition UV/ozone treatment can lower the resistivity of solution deposited $NiO_x$. We have also observed the reduction in resistivity for $NiO_x$ films deposited in different methods like atomic layer deposition (ALD), sputtering, and evaporation. Besides resistivity, ionization potential increases, which makes it more suitable as a hole selective contact to Si. Detailed study using X-ray photoemission spectroscopy (XPS) revealed that after UV/ozone treatment, the oxygen to nickel ratio of the film increases. We conclude that the UV/ozone treatment introduces Ni vacancies into the lattice, which results in increased hole concentration. Previous reports demonstrated surface modification of $NiO_x$ after UV/ozone treatment [90]. This explains the possible increase in ionization potential, which is extremely surface sensitive. Using angle resolved XPS, we observed that besides modifying the surface, UV/ozone treatment increases the O to Ni ratio through the depth of the film. Therefore, surface modification by itself cannot

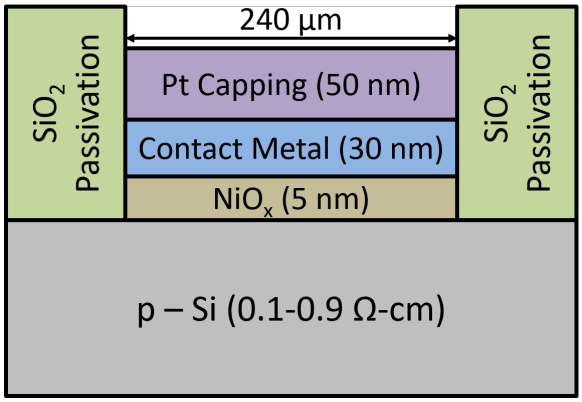


Figure 4.1: Schematic of the fabricated MIS device structure. The active area of the device is 0.0377 $cm^{-2}$.

explain the significant reduction in film resistivity.

Finally, we transferred the UV/ozone treatment results to atomic layer deposition (ALD) synthesized $NiO_x$ on Si from which metal/interlayer/semiconductor (MIS) contacts were fabricated. Schematic of the device is shown in Figure 4.1 and the detail of the fabrication is explained in the experimental section. Effective Schottky barrier height seen by the charge carrier can be extracted from an MIS device [49]. We observed that UV/ozone treatment lowers the effective Schottky barrier height of the contact, which is consistent with our observation of lowering of film resistivity and ionization potential with UV/ozone treatment.

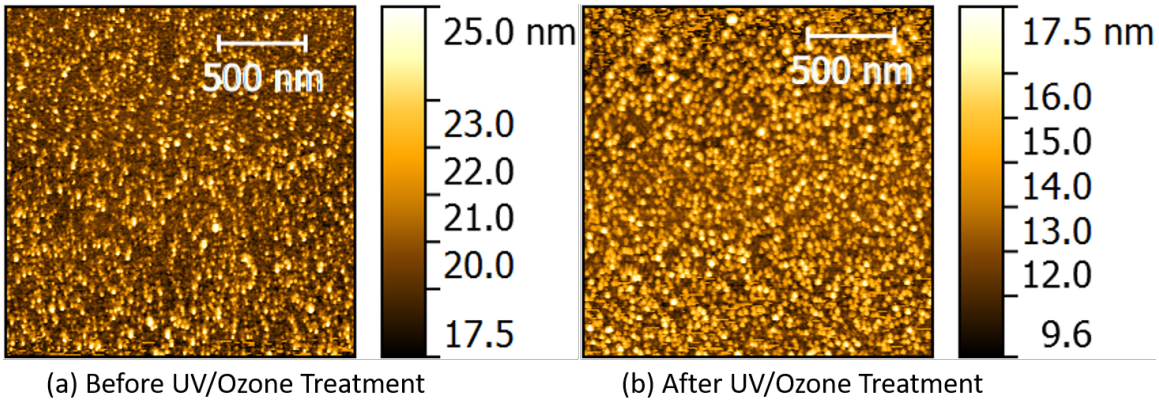


Figure 4.2: Surface morphology of the ultra-thin (10 nm) $NiO_x$ film spin coated on Si. (a) Before UV/ozone treatment (RMS roughness = 1.216 nm) and (b) After 30 min UV/ozone Treatment (RMS roughness = 1.366 nm).

## 4.2 Experimental Section

### 4.2.1 Film Deposition

$NiO_x$ film was deposited using spin coating technique where a solution of Nickel Formate Dihydrate (150 mg), Ethylene Glycol (3 ml) and Ethylene Diamene (150 $\mu$l) was made and stirred at 50 °C - 60 °C overnight. After that the solution was filtered with 0.2 $\mu$m Nylon filter before spin casting it at 4000 rpm for 60 s on the substrate. Glass substrates were used for resistivity characterization. They were sonicated in acetone and isopropyl alcohol (IPA) for 15 mins each followed by a UV/ozone cleaning for 15 mins. Finally the sample was annealed at 300 °C for 60 min. Thicker layers were built up by repeating the spin coating procedure following the anneal. Each coating procedure increased the $NiO_x$ thickness by roughly 10 nm. All the steps were done in ambient condition. Surface morphology of the film before and after UV/ozone treatment was obtained using atomic force microscopy (AFM) (Fig. 4.2. The AFM images show that the surface morphology does not change significantly with UV/ozone treatment. The rms roughness of the film before and after UV/ozone treatment is 1.216 nm and 1.366 nm respectively. This figure suggests that the change in electronic properties of $NiO_x$ after UV/ozone treatment is due to the change in stoichiometry rather than that of surface morphology.

### 4.2.2 Resistivity Measurement

A Van-Der-Pauw structure was made for 4 point probe resistivity measurement. In this technique, a small square sample was prepared by spin coating 40 nm $NiO_x$ on glass substrate with 100 nm gold contacts evaporated at each corner of the square sample using a shadow mask.

### 4.2.3 UV/Ozone Treatment

UV/ozone treatment was performed using a Jelight Inc. UVO-Cleaner® system (model 42). This tool is capable of performing a photosensitized oxidation process, where atomic oxygen and ozone is generated when molecular oxygen is dissociated by the UV light (184.9 nm and 253.7 nm wavelength) generated from a mercury vapor lamp. The 184.9 nm UV line decomposes oxygen molecules and synthesizes ozone according to the following reaction,

$$2O_2 \xrightarrow{184.9\text{ nm}} O_3 + O^*$$

The 253.7 nm UV line decomposes ozone and produces high energy $O^*$ (activated oxygen) according to the following reaction,

$$O_3 \xrightarrow{253.7\text{ nm}} O_2 + O^*$$

The end result of this process is to create highly activated atomic oxygen that reacts with $NiO_x$ to create Ni vacancy in the film. Additionally, UV/ozone treatment removes the organic contaminants from the surface of the film. Detailed mechanism of this process can be found in literature [91].

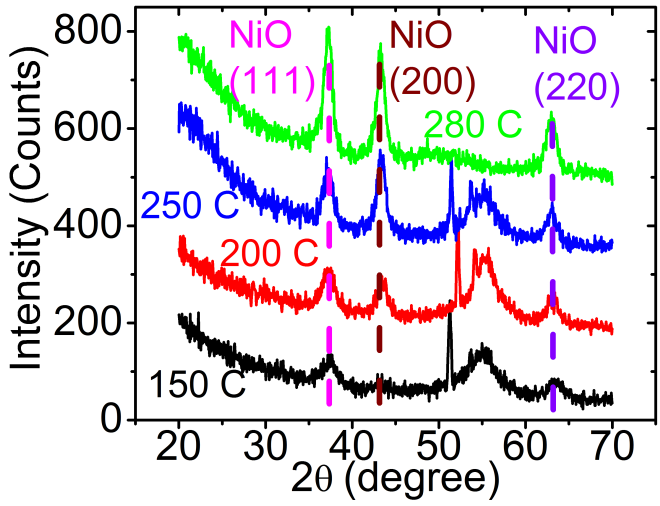


Figure 4.3: Grazing incidence X-ray diffraction (GI-XRD) spectra of NiOx deposited by ALD at different temperatures. Irrespective of the temperature the XRD shows poly-crystalline nature of the film. At 150 °C the peaks are weak. The peaks get stronger with higher temperature.

### 4.2.4 MIS Contact Fabrication

Figure 4.1 shows the schematic of the MIS device used to extract the barrier height for holes at the $Si/NiO_x$ interface. A lightly doped p-type Si wafer (0.1-0.9 Ω-cm resistivity) was RCA cleaned with a final dilute (2%) HF dip to remove any oxide produced during cleaning. It was then placed into the oxidation furnace to grow 300 nm $SiO_2$ using a wet oxidation process. This provides passivation of the Si surface. An open area in the $SiO_2$ was then defined using photolithography and a wet etch in a 2% HF solution. After removing the photoresist in acetone and plasma ashing, a very thin layer of $NiO_x$ (5 nm) was deposited by atomic layer deposition (ALD) technique. ALD deposition of $NiO_x$ was used in this experiment in order to control the thickness of the material precisely, since barrier height is sensitive to interlayer thickness. This technique used alternating pulses of Ni amidinate (Bis(N,N'-di-t-butylacetamidinato) nickel(II)) precursor and ozone in an Intermolecular Inc. Tempus A-30 ALD system to deposit very conformal and uniform (non-uniformity of $< 2\%$ over a 300 mm wafer) films. The precursor temperature was 120 °C and the substrate temperature was 200 °C. In this recipe, the deposition rate was 0.75 - 0.85 Å/cycle. Grazing Incidence X-ray Diffraction result suggests that the film is poly-crystalline with a cubic lattice (Fig. 4.3). A 30 nm metal contact (Al, Cu or Pd) followed by a 50 nm Pt capping layer was deposited next using e-beam

evaporation. The main function of the Pt capping layer is to protect the contacting metal layer from the environmental degradation. Since the I-V characteristics from the three devices containing metal contact having different workfunction is being compared, it is important that the top surface of the metal contact is protected and the surface remains pristine. We deposited the Pt capping layer in the same chamber as the contacting metal without breaking the vacuum. This ensures that the workfunction of the contacting metal remains protected from the environmental degradation. Finally, a second photolithography-patterning step followed by dry etching of metals and underlying $NiO_x$ using an ion-milling process isolated each MIS structure by removing the metals and $NiO_x$ from the $SiO_2$ passivation layer. The UV/ozone treatment (30 min) was done immediately after the $NiO_x$ deposition and before the metal deposition step. We also fabricated control samples where no UV/ozone treatment was performed.

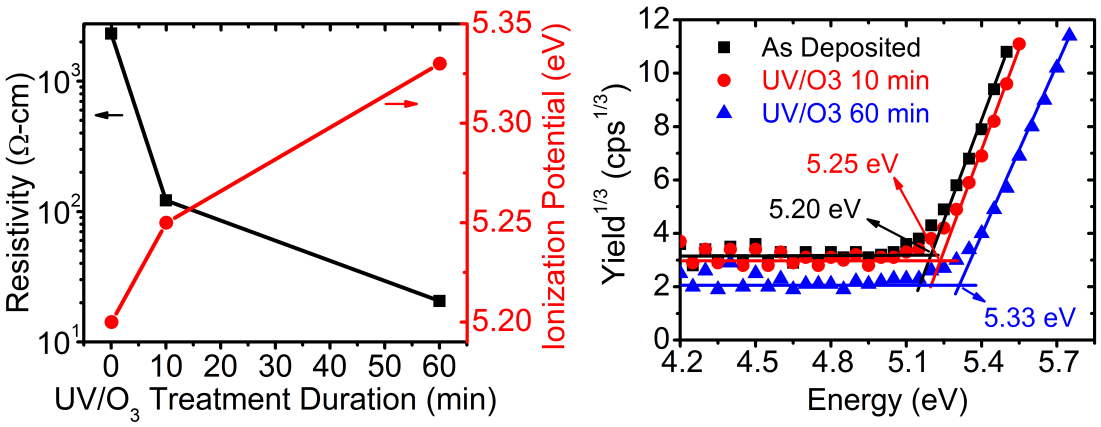


(a) (b)

Figure 4.4: (a) Film resistivity and ionization potential as a function of UV/ozone treatment duration. 0 min signifies the as-deposited film. (b) PESA measurement showing the valence band spectra of $NiO_x$, which was used to extract the ionization potential.

### 4.2.5 Characterization

A Hall measurement system from MMR Technologies Inc. (model H50) was used in the Van-Der-Pauw mode to determine the room temperature conductivity and mobility. Photoelectron Spectroscopy in Air (PESA) was used to measure the ionization potential of the $NiO_x$ films. PESA is a spectroscopic (ultraviolet photoemission spectroscopy (UPS)) technique, which counts the photoemission electrons in air instead of ultra high vacuum [92]. It can reveal the ionization potential of the material and is very surface sensitive [93]. XPS was performed on a PHI Versaprobe system, which uses Al (K$\alpha$) radiation (1486 eV). A cascade microtech probe station was used at different temperatures ranging from -40 °C to 120 °C controlled by the temptronic temperature controller

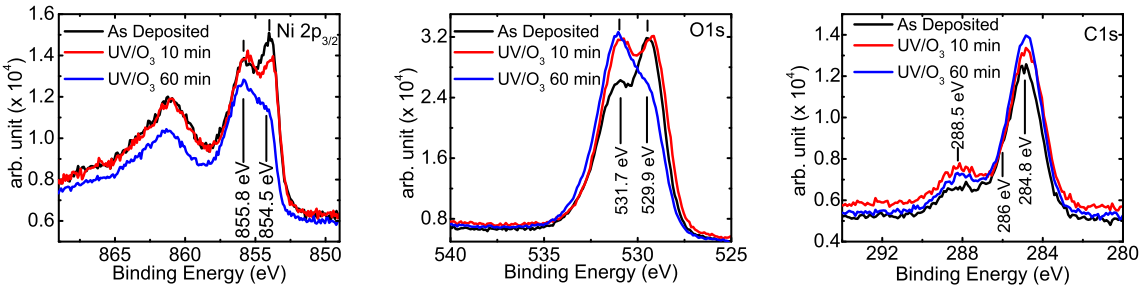


(a) (b) (c)

Figure 4.5: X-ray photoelectron spectroscopy elemental scan of $NiO_x$ for (a) Ni $2p_{3/2}$ (b) O 1s and (c) C 1s for different UV/ozone treatment condition.

to measure the I-V characteristics of the MIS devices, which were used to extract the barrier height for hole transport between Si and the contacts.

## 4.3 Results and Discussion

### 4.3.1 Resistivity and Ionization Potential

The resistivity of a solution synthesized, as-deposited $NiO_x$ film is around $10^3$ Ω-cm (Figure 4.4a). When the film is treated with UV/ozone for 10 minutes, the resistivity drops more than one order of magnitude. For a longer UV/ozone treatment of 60 minutes, the resistivity decreases by two orders of magnitude to values near 10 Ω-cm. Figure 4.4a also shows the ionization potential of $NiO_x$ using photoelectron spectroscopy in air (PESA) measurements (Figure 4.4b). With UV/ozone treatment, the ionization potential of $NiO_x$ increases. Higher ionization potential signifies better hole injection capability of the material when a junction is formed. Liu et al. also reported improvement in hole injection capability of $NiO_x$ with UV/ozone treatment [90]. In this paper [90], the improvement in hole injection capability is explained by an increase in NiO(OH) species on the surface which is dipolar in nature. Eventually the surface dipole on $NiO_x$ is modified resulting in a vacuum level shift at the interface, which improves the hole injection capability. However, the paper concludes that more than 5 min of UV/ozone treatment does not impact the surface of $NiO_x$ anymore and longer UV/ozone treatment does not improve the hole injection efficiency any further. Our results show that longer than 5 min of UV/ozone treatment has significant impact on the film properties (both resistivity and ionization potential).

### 4.3.2 X-ray Photoelectron Spectroscopy (XPS)

In order to explain our results, we compared the XPS spectra of Ni $2p_{3/2}$, O 1s and C 1s for three different conditions of UV/ozone treatment (0, 10 min, 60 min) in Figure 4.5. Different oxidation

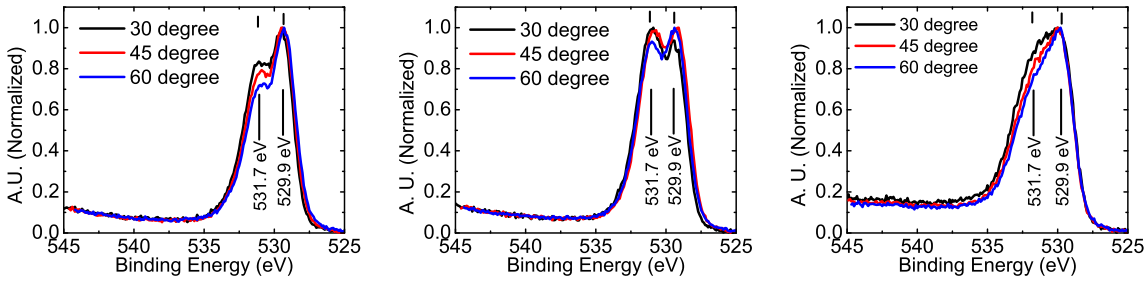


Figure 4.6: Angle resolved XPS spectra of O 1s for (a) as-deposited sample (b) 10 min UV/ozone treated sample and (c) 60 min UV/ozone treated sample for three different angles.

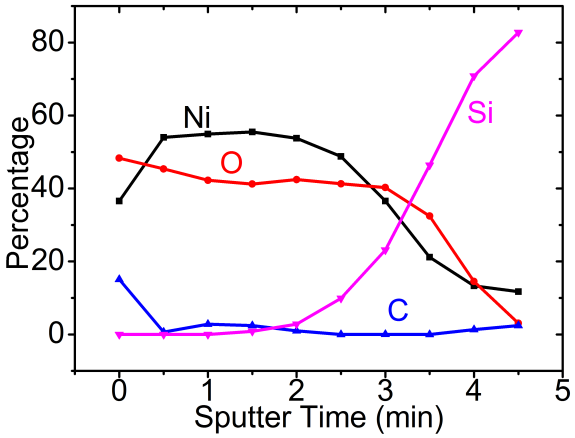


Figure 4.7: Sputter depth profile of the XPS of $NiO_x$ deposited by ALD. The percentages at 0 sputter time indicates the XPS at the surface of the film.

states of Ni manifest themselves in both the Ni $2p_{3/2}$ and O 1s spectra. Therefore both the spectra are used to identify $Ni^{2+}$ and $Ni^{3+}$ states. Figures 4.5a and 4.5b both reveal that with increasing UV/ozone treatment duration the peaks associated with the $Ni^{3+}$ oxidation state (855.8 eV for Ni $2p_{3/2}$ and 531.7 eV for O 1s) increase with respect to peaks associated with the $Ni^{2+}$ (854.5 eV for Ni $2p_{3/2}$ and 529.9 eV for O 1s) oxidation state [94, 95, 96]. It is known that the $Ni^{3+}$ oxidation state arises either from NiO(OH) species or from Ni vacancies inside the lattice [94, 95, 96]. Therefore, with UV/ozone treatment, the growth in the relative strength of the $Ni^{3+}$ state with respect to $Ni^{2+}$ state indicates a shift in the thermodynamic equilibrium toward Ni vacancy formation [97]. After the surface of $NiO_x$ is saturated with NiO(OH) species, the oxygen rich environment causes the atomic oxygen to change the stoichiometry by introducing Ni vacancies. The relative peak intensity for different states of C 1s (284.8 eV for C, 286 eV for C-O and 288.5 eV for C=O) does not show any significant difference with UV/ozone treatment (Figure 4.5c). This carbon probably originates

from a brief exposure of the sample to air between UV/ozone treatment and XPS. Sputter depth profile of the film indicates (Fig. 4.7) that there is no carbon residue inside the film from the organic precursors used in the deposition process.

### 4.3.3 Angle Resolved X-ray Photoelectron Spectroscopy (AR-PES)

Table 4.1: Percentage of area under the fitted curve of O 1s spectra for NiOx having different UV/Ozone treatments at different angles of X-ray incidence.

| | 30° | | 45° | | 60° | | |
|---|---|---|---|---|---|---|---|
| UV/Ozone Condition | Binding Energy (eV) | % Area | Binding Energy (eV) | % Area | Binding Energy (eV) | % Area | Peak Identification |
| As Deposited | 529.28 | 46.1 | 529.22 | 52.79 | 529.21 | 56.72 | $Ni^{2+}$ |
| | 531.11 | 43.46 | 531.02 | 29.74 | 531.07 | 27.1 | $Ni^{3+}$ |
| | 532.67 | 10.44 | 532.1 | 17.46 | 532.16 | 16.18 | C=O/Si=O |
| UV/Ozone 10 min | 529.13 | 38.36 | 529.07 | 43.54 | 529.21 | 48.19 | $Ni^{2+}$ |
| | 530.93 | 45.21 | 530.92 | 43.73 | 531.07 | 38.82 | $Ni^{3+}$ |
| | 532.05 | 16.44 | 532.19 | 12.72 | 532.28 | 12.99 | C=O/Si=O |
| UV/Ozone 60 min | 529.57 | 38.8 | 529.67 | 45.47 | 529.57 | 43.81 | $Ni^{2+}$ |
| | 531.25 | 33.81 | 531.38 | 32.04 | 531.1 | 30.07 | $Ni^{3+}$ |
| | 532.85 | 27.4 | 533.01 | 22.49 | 532.63 | 26.12 | C=O/Si=O |

In order to determine if the stoichiometry change was limited to the surface or occurred throughout the film thickness, we performed angle resolved XPS (AR-XPS) on the same sample for three different angles of photon emission with respect to the sample surface. As angle increases, photoelectrons generated within the sample must pass through more material to escape and be collected. Hence, at high angles the XPS signal contains the most information from the depth of the film and as angle decreases the XPS signal becomes more surface sensitive. Figure 4.6 shows the AR-XPS spectra of O 1s for three different UV/ozone treatment conditions. Since the XPS signal strength varies significantly for different angles, we present the data by normalizing each spectrum to the corresponding highest peak. In the as-deposited sample (Figure 4.6a) the O 1s peak associated with the presence of $Ni^{3+}$ (531.7 eV) decreases in intensity with respect to the $Ni^{2+}$ related peak (529.9 eV) as angle increases indicating a higher concentration of $Ni^{3+}$ near the surface. For a 10 min UV/ozone treatment (Figure 4.6b), the $Ni^{3+}$ related peak intensity remains close to the $Ni^{2+}$ related peak irrespective of the angle. This signifies two points. First, UV/ozone treatment does not only affect the surface of the film but it also introduces Ni vacancies throughout the film. Secondly, the relative height of $Ni^{3+}$ compared to the $Ni^{2+}$ is larger at each angle after 10 minutes of UV/ozone

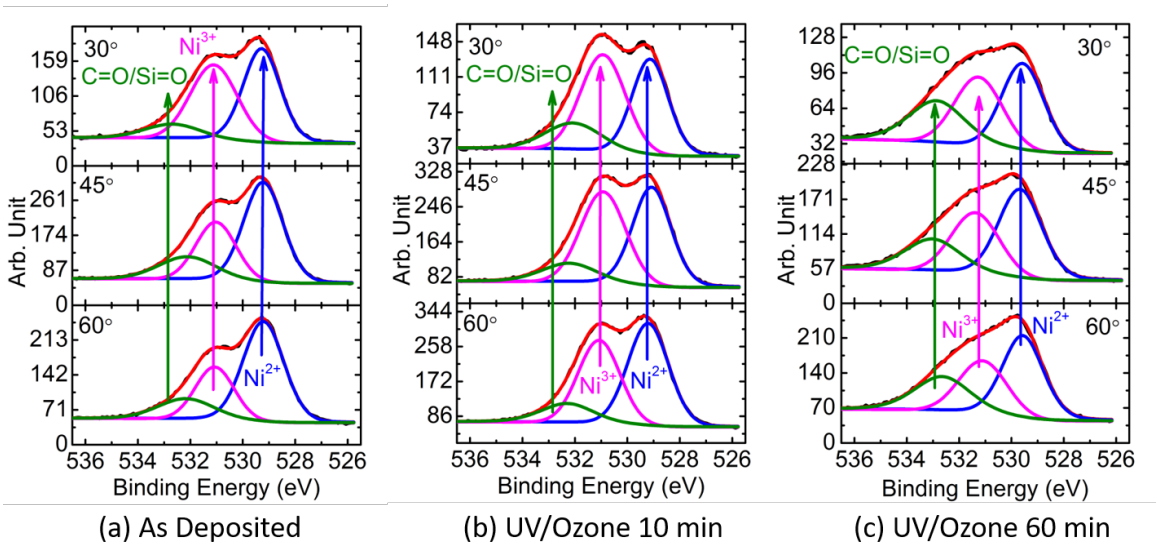


Figure 4.8: Fitting of the O 1s spectra at different angles of photo-electron emission. The fitting is done for three different UV/ozone treatment conditions, (a) as-deposited (b) UV/ozone treatment for 10 minutes (c) UV/ozone treatment for 60 minutes.

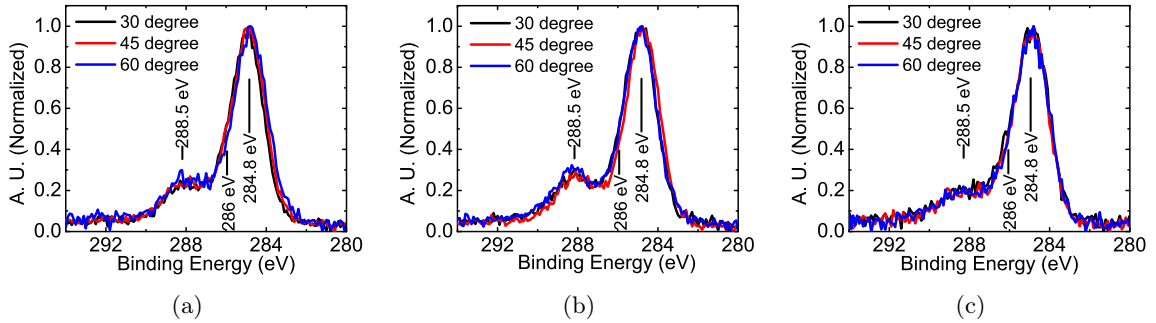


Figure 4.9: Angle resolved XPS spectra of C 1s for (a) as-deposited sample (b) 10 min UV/ozone treated sample and (c) 60 min UV/ozone treated sample for three different angles.

treatment compared to the as-deposited sample. However, when the film is exposed to UV/ozone for even longer time (60 min) (Figure 4.6c), we observe that the $Ni^{3+}$ related peak appears to be reducing with respect to the peak corresponding to $Ni^{2+}$ as the angle increases.

In order to resolve the peaks properly, we fit the O 1s peaks for different angles with Gaussian curves and calculate the underlying area for each peak. The result is tabulated in Table 4.1. The plot of the fitted peaks are shown in Fig. 4.8. From this table, we observe that besides the usual $Ni^{2+}$ and $Ni^{3+}$ peaks, properly fitting the spectra requires including a relatively weaker peak in between 532-533 eV. This peak can be either due to the oxygen bonded with carbon or the oxygen bonded to Si at the interface (Note that the XPS samples were all spin-coated directly on Si substrate instead

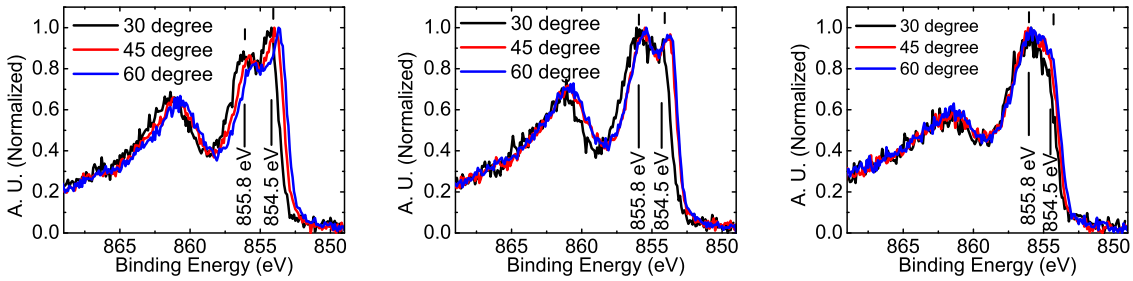


Figure 4.10: Angle resolved XPS spectra of Ni $2p_{3/2}$ for (a) as-deposited sample (b) 10 min UV/ozone treated sample and (c) 60 min UV/ozone treated sample for three different angles.

of glass). The interesting point here is that after a relatively long UV/ozone treatment (60 min), this peak (between 532-533 eV) area increases significantly compared to both the as-deposited and 10 min UV/ozone treated samples. However, if we compare the C 1s spectra of these samples in Figures 4.9a, 4.9b and 4.9c, it is clear that the C=O peak (288.5 eV) intensity reduces with respect to the C-C peak (284.8 eV). This is reasonable since the UV/ozone treatment is expected to clean the surface of the sample by removing the organic contaminants [91]. This also suggests that the peak between 532-533 eV in the O 1s spectra is due to the oxygen bonded to Si at the $NiO_x$/Si interface. Nevertheless, our fit suggests that $Ni^{3+}$ increased related to $Ni^{2+}$ even if we take 532-533 eV peak into account. Therefore, UV/ozone treatment done for sufficiently longer duration could alter the thermodynamic equilibrium of the bulk film creating Ni vacancy.

Figure 4.10 shows the AR-XPS of Ni $2p_{3/2}$ for different UV/ozone treatment conditions. If we compare Figures 4.10a, 4.10b and 4.10c together, we find that irrespective of the angle, $Ni^{3+}$ state becomes stronger than $Ni^{2+}$ state due to UV/ozone treatment. Also, the spectrum at 30 degree seems to be shifted towards higher binding energy (obtained after peak shift correction with respect to C 1s peak). We conclude that the surface is more oxidized (due to adsorbed species, vacancy defects, higher O/Ni ratio etc.) than deeper inside the film. This apparent spectral shift reduces from the as-deposited sample to the UV/ozone treated samples, which suggests that UV/ozone treatment starts impacting the surface first and gradually moves to change the stoichiometry inside the film.

### 4.3.4 Extraction of Ni/O ratio

From Figures 4.6, 4.9 and 4.10 we can extract the film stoichiometry (O/Ni ratio) as a function of angle for different UV/ozone treatment conditions. In order to extract the true stoichiometry oxygen bonded to carbon needs to be quantified and excluded from the overall estimation of oxygen percentage. The fitting of C 1s peak shown in Fig. 4.11 is used to extract the true ratio between Ni and O in the following way:

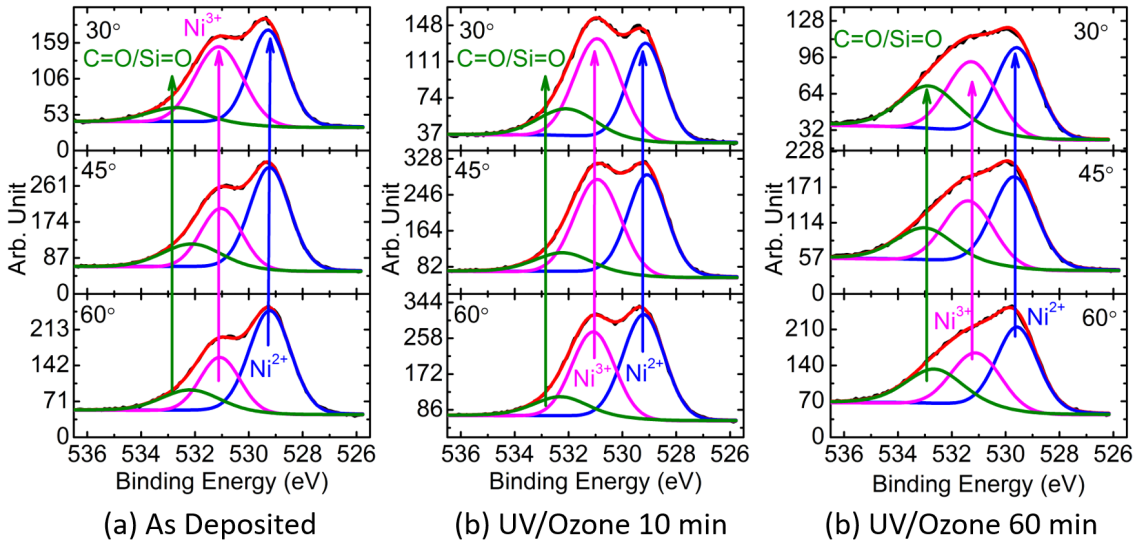


Figure 4.11: Fitting of the C 1s spectra at different angles of photo-electron emission. The fitting is done for three different UV/ozone treatment conditions, (a) as-deposited (b) UV/ozone treatment for 10 minutes (c) UV/ozone treatment for 60 minutes.

1. The area under Ni $2p_{3/2}$, O 1s and C 1s is calculated to extract the raw ratio between different chemical species.

2. The area under the fitted C 1s spectra (Fig. 4.11) gives the estimate of how much O is bonded to C.

3. Subtract the proportional amount of oxygen based on the area under the fitted curve corresponding the C-O and C=O bonds.

4. Calculate the true ratio of Ni to O from the subtracted O percentage.

The film stoichiometry is shown in Figure 4.12. The as-deposited film is close to stoichiometric. The higher relative oxygen content at 30 degree is because of the defects at the surface. After UV/ozone treatment of 10 min, we see a slight increase in O content relative to Ni especially at 45 degree. This change in stoichiometry is consistent with the formation of Ni vacancies. After a 60 min UV/ozone treatment, the O/Ni ratio increases significantly for all acceptance angles. The overall trend of the curve looks similar to the as deposited one. This confirms that the reduced stoichiometry (and high Ni vacancy concentration) relative to the as-deposited sample extends across the thickness of the film.

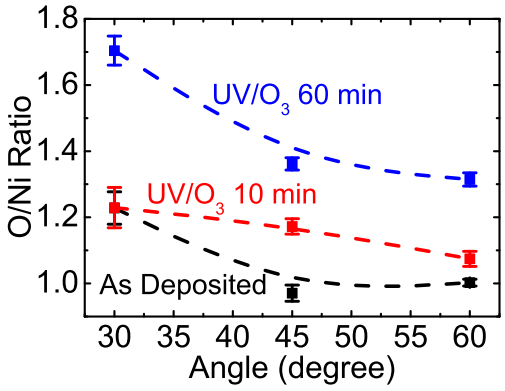


Figure 4.12: $NiO_x$ film stoichiometry extracted from XPS spectra as a function of the angle of XPS. Three different UV/ozone treatment conditions are shown. The dotted lines are a guide to the eye.

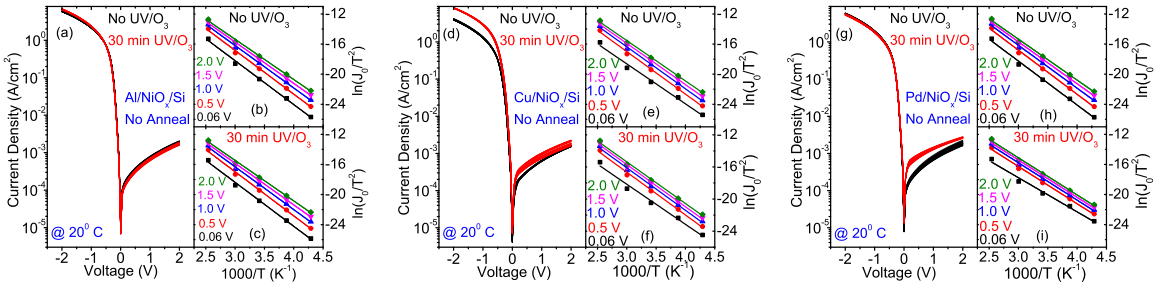


Figure 4.13: Current-voltage characteristics of metal/$NiO_x$/p-Si MIS contact (schematic shown in Fig. 4.1) for (a) Al (d) Cu and (g) Pd. Richardson plots extracted from the I-V characteristics at different temperatures are shown at different reverse bias voltages for as-deposited $NiO_x$ [(b) - Al, (e) - Cu, (h) - Pd] and for 30 min UV/ozone treated $NiO_x$ [(c) - Al, (f) - Cu, (i) - Pd].

### 4.3.5 Extraction of Hole Barrier Height

Figure 4.13 shows the current-voltage (I-V) characteristics of the MIS devices (details in experimental section) for different metal contacts ((a) Al, (b) Cu and (c) Pd) comparing the I-V between as-deposited and 30 min UV/ozone treated $NiO_x$. Each of these figures provides two additional Richardson plots shown in the smaller panels extracted from the associated I-V plot [49]. If we assume the effective barrier height for holes to be $\phi_{Bp}$, then the Schottky contact equation for a metal-semiconductor junction is,

$$J = A^* T^2 e^{-\frac{q\phi_{Bp}}{kT}} \left( e^{-\frac{qV}{kT}} - 1 \right) \tag{4.1}$$

where $J$ is the current density, $A^*$ is the Richardson constant, $T$ is the temperature in Kelvin, $q$ is the electronic charge, $k$ is Boltzmann's constant and $V$ is the applied voltage. The reverse

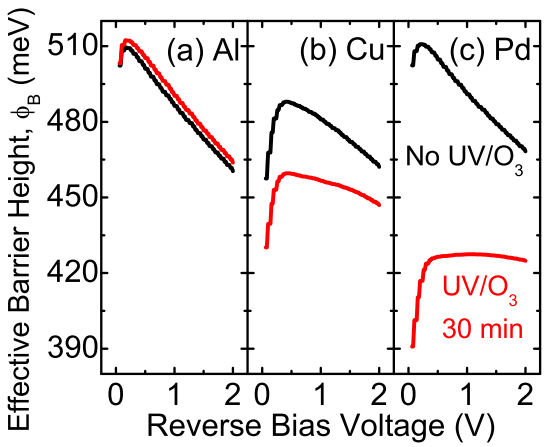


Figure 4.14: Effective barrier height extracted from the slope of the Richardson plots in Figure 4.13 as a function of reverse bias voltage for different metal contacts (a) Al (b) Cu and (c) Pd comparing the as-deposited and 30 min UV/ozone treated $NiO_x$.

saturation current of the aforementioned junction ($J_0$) can be approximated as,

$$J_0 \approx A^* T^2 e^{-\frac{q\phi_{Bp}}{kT}} \tag{4.2}$$

From rearranging this equation we get,

$$ln\left(\frac{J_0}{T^2}\right) \approx ln\left(-A^*\right) - \frac{q\phi_{Bp}}{kT} \tag{4.3}$$

Therefore, if $ln\left(\frac{J_0}{T^2}\right)$ is plotted as a function of $\frac{1}{T}$ a straight line is generated which is called the Richardson plot. The slope of this curve gives the effective barrier height. It is referred to as an effective barrier height because this technique of extracting barrier height cannot distinguish between the thermionic emission over the barrier and tunneling through the peak of the barrier. Since the barrier shape and hence tunneling probability changes with bias, the effective barrier height varies with reverse bias voltage. The I-V curves shown in Figure 4.13 were obtained at 20 °C. Corresponding Richardson plots for 5 different reverse bias voltages are shown with each I-V curve for both the as-deposited and 30 min UV/ozone treated $NiO_x$. Al, Cu, Pd metal layers were chosen because they span a wide range of metal workfunctions (Al = 4.05 - 4.26 eV, Cu = 4.53 - 5.10 eV, Pd = 5.22 - 5.6 eV). We can see that with an Al metal contact the I-V curve does not change significantly after UV/ozone treatment. This difference between the untreated and the treated I-V curves gradually increases from Al to Cu to Pd. In particular, as the metal workfunction increases so does the reverse saturation current. All the Richardson plots show excellent fits to straight lines, which lends confidence that this model is an appropriate way to extract barrier heights.

We have extracted barrier heights from the Richardson plots and presented them as a function

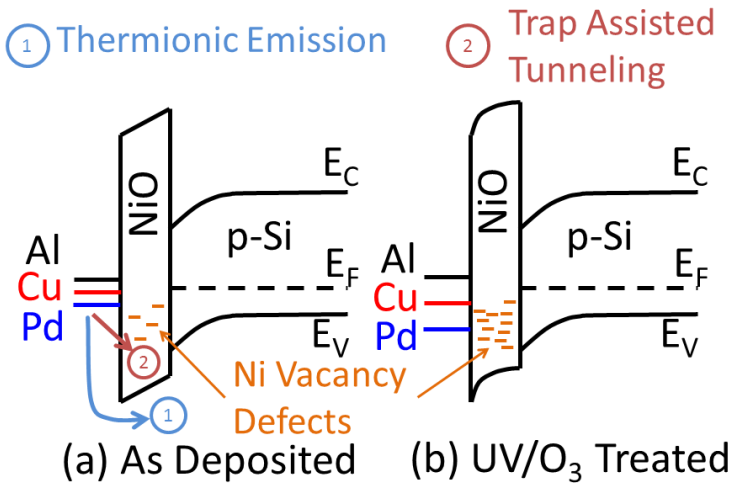


Figure 4.15: Energy band diagram of Metal/$NiO_x$/p-Si for (a) as deposited and (b) UV/Ozone treated $NiO_x$. Three different metals' Fermi level pinning position is shown. UV/Ozone treatment reduces the pinning and increases vacancy defects (not drawn to scale).

of the reverse bias voltage in Figure 4.14. Starting from the zero bias, as voltage increases, the band bending increases and the current becomes completely thermionic emission dominated [98]. Therefore initially the barrier height increases sharply. However, increasing reverse bias results in higher tunneling (both trap assisted and direct tunneling). Therefore, the barrier height starts decreasing at higher reverse bias. While UV/ozone treatment has almost no effect on devices with Al metal, barrier height decreases with treatment for the other metals, and the greater the workfunction of the metal, the larger the magnitude of the decrease.

The results shown in Figure 4.14 can be explained by taking two factors into consideration. First, UV/ozone treatment affects the surface dipole of $NiO_x$ [90], which shifts the vacuum level at the metal/$NiO_x$ interface resulting in a change in the pinning properties. Similar effects have also been observed for oxygen plasma treatment [99]. Secondly, lowering resistivity by creating Ni vacancies introduces defect states near the valence band [83], which increases trap assisted tunneling. In order to visualize the effect of these two phenomena, we look into the schematic energy-band diagram of the MIS contact in Figure 4.15. This figure summarizes all the changes that occur in $NiO_x$ due to UV/ozone treatment. We can explain the results in Figure 4.14c if we consider the increase in trap assisted tunneling and assume the reduction in pinning when $NiO_x$ is UV/ozone treated for high workfunction metal like Pd. Since Al has much lower workfunction than Pd, the reduction in pinning due to the UV/ozone treatment does not change the effective barrier height significantly. The defect states due to the Ni vacancies appear near the valence band [83]. Therefore, for a lower workfunction

metal (Al), trap assisted tunneling does not increase significantly with UV/ozone treatment as well. The as-deposited Cu shows a lower barrier height than both Al and Pd, despite high amount of pinning. This might be because of the formation of an interfacial copper oxide, which increases trap assisted tunneling resulting in a lower effective barrier height.

## 4.4 Conclusion

In this chapter we have investigated the effect of UV/ozone treatment on $NiO_x$. Our experimental results suggest that UV/ozone treatment creates non-stoichiometry in $NiO_x$ resulting in Ni vacancy defects, which lowers the film resistivity. Metal/$NiO_x$/p-Si devices show lower Schottky barrier height for holes due to this increase in vacancy defects and a reduction in pinning caused by the change in surface dipole created from the treatment. This study shows an effective way to engineer p type contacts to $NiO_x$ and to control the electrical properties of the film.

# Chapter 5

# Characterization of Oxide-Selective Contacts - Fermi Level Pinning Study and Contact Selectivity

## 5.1 Introduction

In chapter 3, we have observed that Fermi level pinning is an important consideration for designing oxide selective contact for solar cell. Also, we have established a qualitative definition of contact selectivity in chapter 2 but have not yet shown any experimental technique to quantify contact selectivity. In this chapter, these two issues will be addressed.

First, we report the experimental demonstration of Fermi level depinning using nickel oxide (NiO) as the insulator material in metal-insulator-semiconductor (M-I-S) contacts. Using this contact, we show less than 0.1 eV barrier height for holes in Pt/NiO/p-Si contact. Overall, the pinning factor was improved from 0.08 (metal/Si) to 0.26 (metal/NiO/Si). The experimental results show good agreement with that obtained from theoretical calculation. NiO offers high conduction band offset and low valence band offset with Si. By reducing Schottky barrier height, this contact can be used as a carrier selective contact allowing hole transport but blocking electron transport, which is important for high efficiency in photonic applications, such as, photovoltaics and optical detectors.

Second, we extract the contact resistivity of Metal/NiO/Si contact with both n and p type Si. It can be observed that the asymmetry of contact resistivity between n and p contact is increased significantly compared to that of the the control sample of Metal/Si contact giving the proof of increasing contact selectivity. Based on the ratio of contact resistivity for n and p type carrier we finally define the metric contact selectivity (CS) as a performance metric for contacts in solar cells.

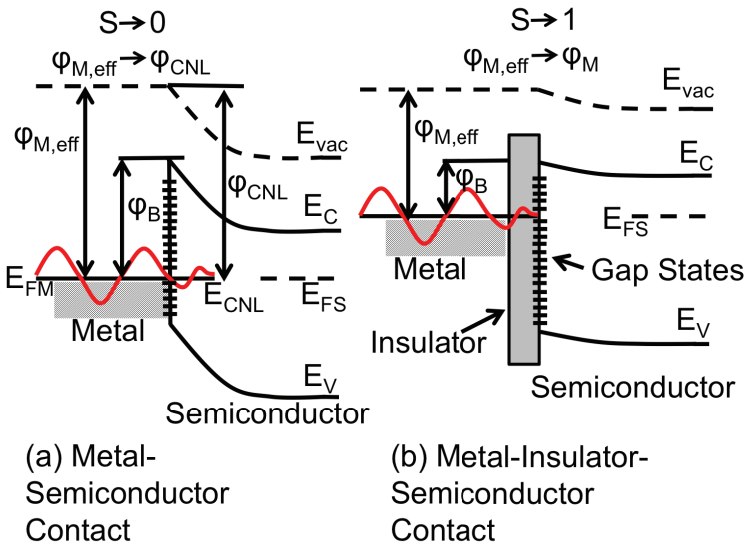


Figure 5.1: Fermi level pinning explained. (a) M-S contact where the Fermi level is pinned at the charge neutrality level. This is the case where S is closed to zero. (b) M-I-S contact where the Fermi level is depinned and effective Fermi level is aligned with the metal Fermi level. This is the case where S is closed to 1.

## 5.2 Fermi Level Pinning Theory

Fermi level pinning theory suggests that in a metal-semiconductor (M-S) contact wave functions of electrons in the metal can decay into the semiconductor in the band gap (Fig. 5.1), creating intrinsic states known as the metal-induced gap states (MIGS) [100]. The energy level in the band gap at which the dominant character of the interface states changes from donorlike to acceptorlike is called the charge neutrality level ($E_{CNL}$). In a M-S junction, charge transfer generally occurs across the interface, charging of these states creates a dipole that tends to drive the band lineup toward a position that would give zero dipole charge. This effectively pulls the metal Fermi level ($E_{FM}$) towards the charge neutrality level ($E_{CNL}$). How strongly $E_{FM}$ will be pinned towards $E_{CNL}$ is determined by the pinning factor ($S$), which is defined as the rate of change in the Schottky barrier height ($\phi_B$) with respect to the change in metal workfunction ($\phi_M$). An Empirical trend established by Mönch [72] relates $S$ to the dielectric screening of the material on which the metal Fermi level is pinned as,

$$S = \frac{\partial \phi_B}{\partial \phi_M} = \frac{1}{1 + 0.1(\varepsilon_\infty - 1)} \tag{5.1}$$

The effective metal workfunction ($\phi_{M,eff}$) of a pinned M/S junction is therefore given by,

$$\phi_{M,eff} = S\phi_M + (1 - S)\phi_{CNL} \tag{5.2}$$

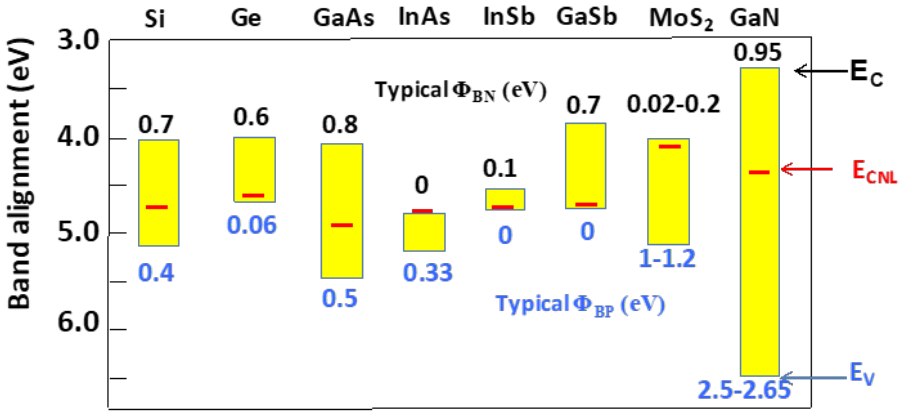


Figure 5.2: Energy band lineup of different semiconductors with known charge neutrality level and the resulting barrier height for electrons and holes written.

Here, $\varepsilon_\infty$ is the high frequency dielectric constant and $\phi_{CNL}$ is the charge neutrality level with respect to the vacuum. Fig. 5.2 shows the pinning properties of common semiconductors.

Pinning can cause large contact resistance due to a very high Schottky barrier height irrespective of the metal used. Insertion of an ultra-thin insulating layer between semiconductor and metal is known to reduce this barrier [101]. The purpose of the insulating layer is to attenuate the metal wavefunction penetration into the semiconductor, reducing MIGS and thus reduce pinning (Fig. 5.1). In the early work common oxides and nitrides have been proposed for this purpose as insulator [101]. This introduces high tunneling resistance resulting in a trade-off between decreasing pinning and added tunneling resistance. Proper choice of band offset for the desired contact can solve the problem of added tunneling resistance in metal-insulator-semiconductor (M-I-S) contacts. For example, $TiO_2$ and ZnO have been shown to reduce the contact resistance for electrons in n-Si, n-GaAs and n-Ge [102, 103, 104, 105]. These oxides work better in n type contact because they have close to zero conduction band offset. Most of the research efforts so far have been centered on the reduction of effective barrier height seen by electrons in n type contacts by the depinning of metal Fermi level using M-I-S contacts. N type contact in Si and Ge is problematic because metal pins close to the valence band. This introduces large Schottky barrier height for electrons resulting in high contact resistance. Reduction of the barrier for holes in p-Si is also important because it will lead to the path of designing low-doped highly conductive p type contact with higher selectivity between two types of carriers. By selective contact we mean a contact, which allows only one type of carrier and blocks the other type of carrier. Selective contacts are useful in solar cell where proper separation of carriers upon generation inside the absorber is the key to ensure high open circuit voltage. Recently, it has been shown that highly selective low-doped M-I-S contact can improve the efficiency of c-Si solar cell up to 27% in ideal condition [57]. Therefore, M-I-S contact for both types of carrier is essential for high efficiency solar cell. However, nothing has been reported

experimentally in this regard so far. Recently, NiO has been predicted to work as a suitable material for MIS contact to p-Si [105]. The prediction has been made on the basis of band lineup with Si. The band lineup of NiO with respect to Si is suitable for reducing barrier height for holes because there is a small valence band offset and a high conduction band offset [43].

In this chapter, we have shown for the first time, the experimental proof of barrier height reduction for holes using NiO as an insulator in M-I-S contacts on p-Si. By varying the metal workfunction, we have experimentally extracted the effective barrier height seen by holes in metal/NiO/p-Si M-I-S contacts and compared it with the control sample of metal/p-Si. We have seen significant improvement in the pinning factor from 0.08 to 0.26. We have shown barrier height less than 0.10 eV for Pt contact to p-Si. This finding signifies that NiO can be a suitable choice for hole selective p type contact in Si solar cells replacing highly doped $p^{++}$ contact region with a better carrier selectivity.

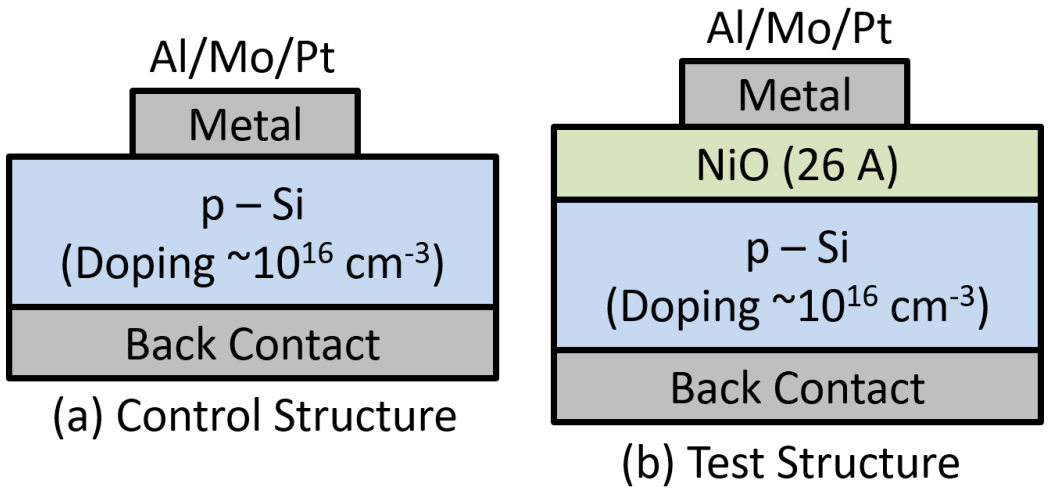


Figure 5.3: Metal/NiO/Si Schottky barrier contact to study Fermi level pinning. Top metal contact is varied (Al, Mo, Pt) in each sample.

## 5.3 Device Fabrication

Experimental structures are shown in Fig. 5.3. NiO was deposited on moderately doped ($10^{16}$ $cm^{-3}$) p-type Si wafer using RF magnetron sputtering from a NiO target. The deposition was done with a flow of 5 sccm of oxygen and 45 sccm of argon gas mixture at a pressure of 3 mTorrr. Higher oxygen partial pressure during NiO deposition is reported to have higher conductivity by introducing both $Ni^{3+}$ and $Ni^{2+}$ states [106]. The thickness of the NiO deposited was 26 Å measured from Ellipsometry. On top of the NiO layer, metal was patterned by lithography. The other contact was taken from the back of the silicon substrate. Before any processing, Si wafers were cleaned in

Piranha solution and dipped in HF to keep the native oxide at a minimum. In order to vary the metal workfunction, three different metals were deposited - Aluminum (Al), Molybdenum (Mo) and Platinum (Pt). With workfunction varying from 4.16 eV to 5.52 eV, this covers almost the entire bandgap range of Si. M-S structures using the same metals on p-Si were also fabricated in order to compare the Schottky barrier heights of different metals with and without the presence of NiO.

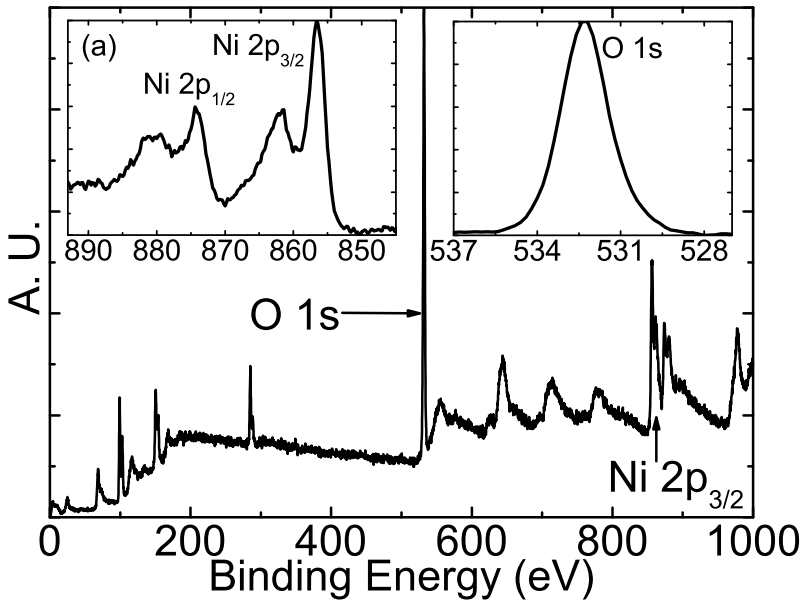


Figure 5.4: X-ray Photoemission spectroscopy of the deposited NiO. (a) Survey scan (b) Elemental scan of Ni $2p_{3/2}$, $2p_{1/2}$ and O 1s peak shown.

X-ray Photoemission Spectroscopy (XPS) profile of the deposited NiO is shown in Fig. 5.4. The survey scan shown in Fig. 5.4 confirms the existence of a slightly oxygen rich NiO. Inset figures show (a) the Ni 2p (both $2p_{3/2}$ and $2p_{1/2}$) and (b) the O 1s elemental scan. Both these peaks occur at higher binding energy than that reported for stoichiometric NiO [94]. The peaks at higher binding energy are attributed to the $Ni^{3+}$ states, which is a result of defects inside NiO crystal. Usually in NiO, the defects are formed as metal deficiency or oxygen interstitials. Both the figures (5.4(a) and 5.4(b)) prove that the deposited NiO has metal vacancy sites created due to defect formation. Each metal vacancy site in NiO contributes two holes to the crystal lattice. Thus, NiO that we deposited on Si becomes a p-type semiconductor, which aids transport of holes from Si to metal and blocks electrons. This is important for the selectivity of holes in p type contacts on Si.

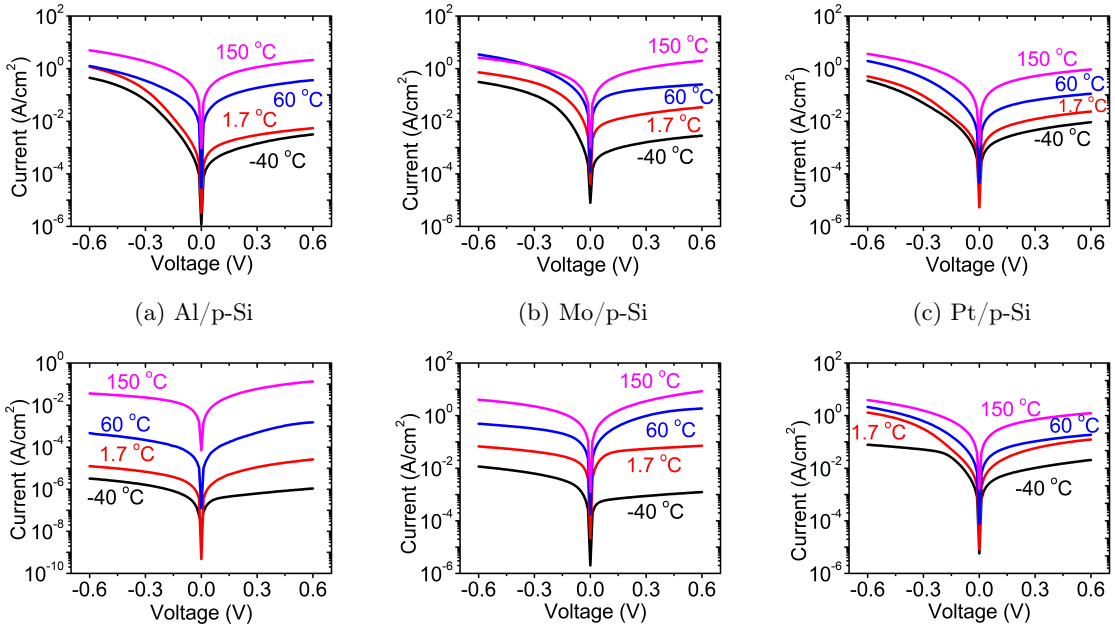


(a) Al/p-Si (b) Mo/p-Si (c) Pt/p-Si

(d) Al/NiO/p-Si (e) Mo/NiO/p-Si (f) Pt/NiO/p-Si

Figure 5.5: Temperature dependent I-V characteristics of Metal/p-Si contact (top) and Metal/NiO/p-Si contact (bottom) from which the barrier height is extracted.

## 5.4 Extraction of Schottky Barrier Height

To extract the Schottky barrier height, temperature dependent current-voltage (I-V) measurements were made within the temperature range of $-40\,^{\circ}\mathrm{C}$ to $150\,^{\circ}\mathrm{C}$. Note that the barrier height extracted using this method is the electrical equivalent of the M-S junction, but it may or may not be the physical barrier height of an M-I-S junction. For this reason, the extracted barrier height is termed as the "effective Schottky barrier height". If the effective Schottky barrier height is expressed as $\phi_{Bp}$ for holes, the Schottky contact equation for a typical metal-semiconductor junction is defined as,

$$J = A^{*}T^{2}exp\left(-\frac{q\phi_{Bp}}{kT}\right)\left[exp\left(-\frac{qV}{kT}\right)-1\right] \tag{5.3}$$

where, $J$ is the current density, $A^{*}$ is the Richardson constant, $T$ is the temperature in Kelvin, $q$ is the electronic charge, $k$ is the Boltzmann constant and $V$ is the applied voltage. The reverse saturation current $J_0$ can be approximated as,

$$J_0 \approx A^{*}T^{2}exp\left(-\frac{q\phi_{Bp}}{kT}\right) \tag{5.4}$$

From rearranging this equation, we can write,

$$ln\left(\frac{J_0}{T^2}\right) \approx ln\left(-A^*\right) - \frac{q\phi_{Bp}}{kT} \tag{5.5}$$

Therefore, $ln\left(\frac{J_0}{T^2}\right)$ vs. $\frac{1}{T}$ curve is a straight line with a slope of $-\frac{q\phi_{Bp}}{k}$. This curve is known as the "Richardson plot" which is used in this study to extract effective Schottky barrier heights of holes.

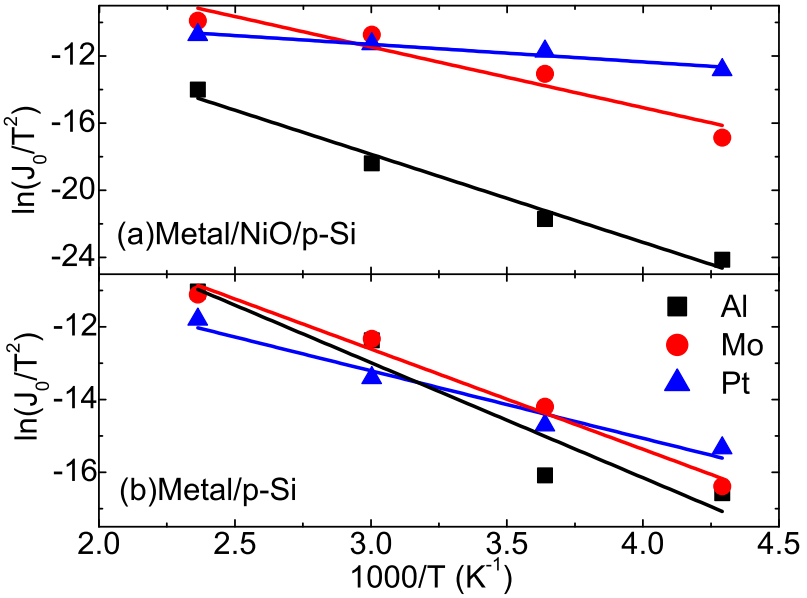


Figure 5.6: Richardson plot of the contacts for three different metals âĂŞ Al, Mo, Pt. (a) Metal/NiO/p-Si (b) Metal/p-Si. The plots are obtained from temperature dependent current-voltage measurement.

## 5.5 Results and Discussion

From the temperature dependent I-V curves (Fig. 5.5, the reverse saturation current is extracted. The Richardson plots of M-I-S contacts along with the corresponding M-S contacts are shown in Fig. 5.6. The experimental results shown in this figure can be fitted reasonably well with a straight line. This signifies that the theory described above is equally applicable to both M-S and M-I-S Schottky contacts considering effective Schottky barrier heights for M-I-S contacts. From the slopes of the straight lines shown in Fig. 5.6, the effective Schottky barrier heights are extracted and shown as a function of metal workfunction in Fig. 5.7. For low workfunction metal like Al, the Schottky barrier height increases with the insertion of NiO, whereas for high workfunction metal like Pt, the Schottky barrier height decreases. This means that insertion of NiO moves the Fermi level pinning

position of metals according to their workfunction. Therefore, it is proven that M-I-S contacts with NiO as insulator on p-Si can provide effective Fermi level depinning of metals so that for high workfunction metal Schottky barrier height for holes decreases. Effective barrier height for both the test and control sample shows linear variation with respect to the change in metal workfunction.

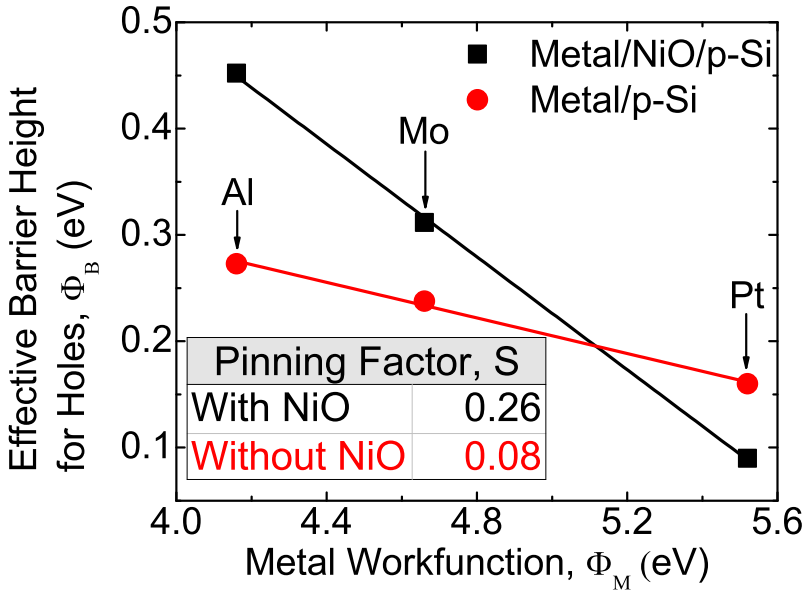


Figure 5.7: Extracted effective barrier height for holes as a function of metal workfunction shown for both with NiO and without NiO. The pinning factor (S) is the slope of the straight line connecting the data points.

Table 5.1: Comparison of the pinning factor from experiments with that of theoretical calculation.

| | Experimental | Calculation from Eq. 5.1 |
|---|---|---|
| Metal/NiO/Si | 0.26 | 0.31 |
| Metal/Si | 0.08 | 0.078 |

From Fig. 5.7 we can extract the pinning factor ($S$) experimentally by calculating the slope of the straight line fitting the data points. The experimentally determined pinning factor along with the theoretical calculation from Eq. (5.1) is tabulated in Table 5.1. A good agreement is seen in experiment and theoretical calculation. The pinning factor of M-S contact shows consistent result with previously reported experimental results [104] also. Effective metal workfunction is calculated directly from the extracted effective barrier height considering the electron affinity (4.0 eV) and bandgap (1.12 eV) of silicon. Then the CNL of NiO and Si is calculated using Eq. (5.2) and tabulated in Table 5.2. CNL values are consistent for different metal workfunctions and match well with the previously reported values [43].

Table 5.2: Comparison of the charge neutrality level extracted from experiments with that of reported values. $\phi_{Bp}$ is with respect to the valence band of Si and the rest are with respect to the vacuum. All values are in eV.

| | Metal ($\phi_M$) | $\phi_{Bp}$ | $\phi_{M,eff}$ | $\phi_{CNL}$ (Experiment) | $\phi_{CNL}$ (Ref. [43]) |
|---|---|---|---|---|---|
| With NiO | Al(4.16) | 0.4521 | 4.6679 | 4.8512 | 4.9 |
| | Mo(4.66) | 0.3118 | 4.8082 | 4.8617 | |
| | Pt(5.52) | 0.0901 | 5.0299 | 4.8529 | |
| Without NiO | Al(4.16) | 0.2729 | 4.8571 | 4.9099 | 4.82 |
| | Mo(4.66) | 0.2377 | 4.8823 | 4.9027 | |
| | Pt(5.52) | 0.1601 | 4.9599 | 4.9087 | |

To predict NiO's performance in lowering contact resistivity, we calculate conductivity of Pt/NiO/p-Si device using the Tsu-Esaki model

$$J = \frac{qm^*kT}{2\pi^2\hbar^3} \int d\epsilon_\perp \; T(\epsilon_\perp) \; log\left(\frac{1+exp(\frac{E_{F_1}-\epsilon_\perp}{kT})}{1+exp(\frac{E_{F_2}-\epsilon_\perp}{kT})}\right) \tag{5.6}$$

where $T(\epsilon_\perp)$ is the transmission evaluated from numerical solutions to the Schrödinger and Poisson equations [105]. NiO electron affinity is assumed 1.5 eV, which is reported consistently in the literature [107]. The badgap of NiO reported in the literature varies from 3.6 - 4.0 eV [73]. Since the contact resistivity depend on the tunneling barrier, bandgap variation changes contact resistivity. We vary the bandgap of NiO and calculate the contact resistivity as a function of NiO Thickness (Fig. 5.8).

The results show that NiO has the potential to lower contact resistivity but it is exponentially sensitive to the barrier height (band gap) and barrier thickness, as expected in tunneling systems. However, around the thickness of 5 Å, which roughly represents one monolayer of NiO, contact resistivity improves irrespective of the bandgap. This signifies the impact of lowering Schottky barrier height in reducing contact resistivity. Deliberate engineering of the NiO gap and precise control of the thickness are the promising tools for making low-resistance contacts. Although Pt was chosen as a representative high workfunction metal, the result shown in this simulation holds for any high workfunction metal. Nickel ($\phi_M$ = 5.25 eV) can be another low cost alternative to Pt suitable for photovoltaics.

## 5.6 Asymmetry of Contact Resistivity as Contact Selectivity

In the earlier part of this chapter, NiO is shown as a potential insulator for M-I-S contact on p-Si to depin the Fermi level. Experimental results suggest that for high workfunction metal, Schottky barrier height seen by holes can be lowered significantly. This type of structure enables low resistance

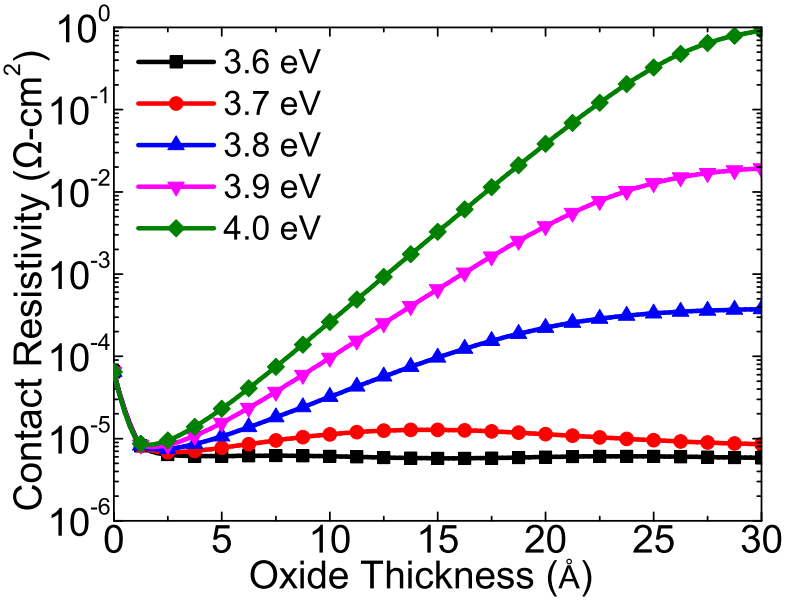


Figure 5.8: Simulated contact resistivity as a function of NiO thickness for different bandgaps. The electron affinity is assumed 1.5 eV.

contact without the necessity of high doping. Besides reducing Schottky barrier height, NiO offers high conduction band offset but low valence band offset to Si. This results in asymmetry in contact resistivity between electrons and holes. We observed that contact resistivity asymmetry can also be obtained from doping a semiconductor heavily. In the second part of this chapter, we show that due to the band offset asymmetry, NiO shows much higher asymmetry of contact resistivity between p and n type contacts.

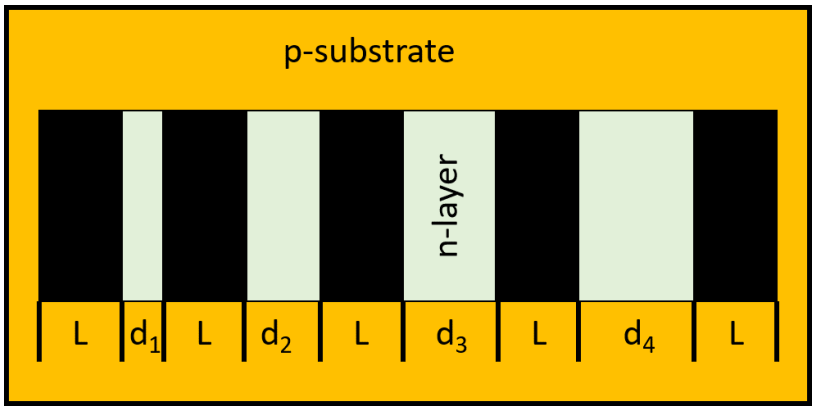


Figure 5.9: Linear TLM structure top view.

## 5.7 Contact Resistivity

Contact resistance between a metal and semiconductor contact is defined as,

$$R_c = \frac{\rho_c}{A} \tag{5.7}$$

where, $\rho_c$ is the contact resistivity and $A$ is the area of the contact. $\rho_c$ can be related to the material parameters using the following equation,

$$\rho_c \propto exp\left(\frac{2\phi_B}{\hbar}\sqrt{\frac{\epsilon_s m^*}{N(orP)}}\right) \tag{5.8}$$

In this equation, $phi_B$ is the barrier height seen by the carrier, $\epsilon_s$ is the dielectric constant of the semiconductor and $N(orP)$ is the carrier concentration (N for electrons, P for holes). If the semiconductor is very lightly doped (almost intrinsic), both N and P are comparable to each other and the asymmetry in contact resistivity only arises from the barrier height seen by the corresponding carrier, which depends on Fermi level pinning. Generally the contacts in a solar cell is higher doped than the absorber. This increases either the N (n-type contact) or P (p-type contact), which results in the decrease in contact resistivity for the majority carrier type and increase in contact resistivity for the minority carrier type. This forms the basis of contact selectivity. For heterojunctions, band offsets, if chosen properly, can bring in another component of tunnel barrier into the contact resistivity equations. This dramatically increases the contact resistivity of the minority carrier while keeping the contact resistivity of the majority carrier unchanged (or lower). This asymmetry in contact resistivity can be taken as a metric for the determination and comparison of contact selectivity.

In order to extract the contact resistance and hence contact resistivity, the *Transmission Line Method* (TLM) has been used. In this technique, rectangular contacts are patterned on the semiconductor of interest at different distances d (Fig. 5.9). The semiconductor region is formed as a mesa to suppress the current in non-perpendicular direction across the contact metal. In this structure, the total resistance between any two contacts can be expressed as,

$$R_T = \frac{R_{sh}}{W}(d + 2L_T) \tag{5.9}$$

Here, $R_{sh}$ is the sheet resistance of the semiconductor (which depends on the carrier concentration). If equation 5.9 is plotted as a function of d (distance between the contacts as seen in Fig. 5.9), the resulting line is a straight line with the y-intercept being $2R_c$ (2×contact resistance) and the x-intercept being $2L_T$ (2×transfer length) (Fig. 5.10). The transfer length is defined as the length under the contact within which most of the current is transferred from the semiconductor to the metal. This depends on the contact resistivity and the sheet resistance in the following way,

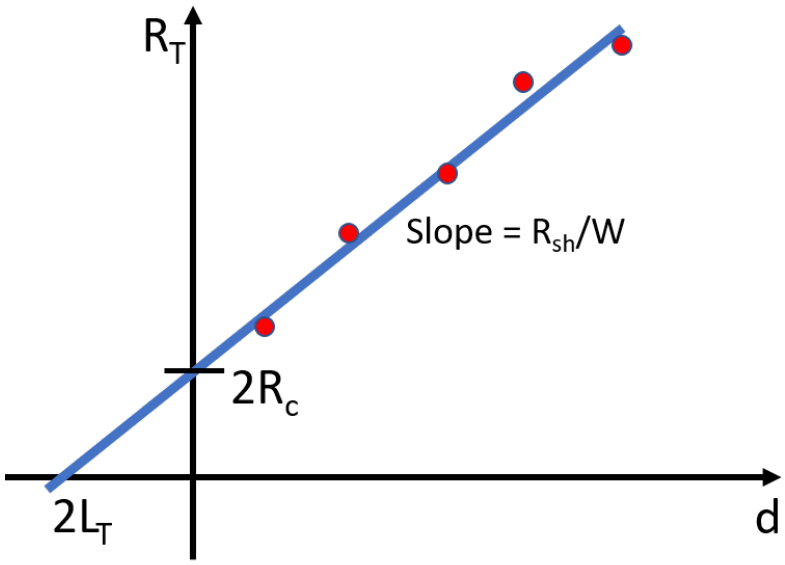


Figure 5.10: Linear R vs d characteristics of a typical TLM graph.

$$L_T = \sqrt{\frac{\rho_c}{R_{sh}}} \tag{5.10}$$

From equation 5.10, contact resistivity can be extracted. If the contact length $L >> L_T$ then the TLM method contact extraction does not depend on $L$.

In the next section, it is shown using TLM measurements that integrating NiO in metal/Si contacts can increase the asymmetry between electron and hole contact resistivity significantly. In order to create contacts dominated by electrons Metal/NiO/$n^+$-Si contacts were fabricated. Also, metal/NiO/$p^+$-Si were fabricated to create hole dominated contact. For each case the corresponding control sample is fabricated without any NiO.

## 5.8 Device Fabrication

To measure the contact resistivity, four configurations of TLM test structures were fabricated on c-Si, using platinum (Pt) as the metal contact: (i) Pt/$n^+$-Si metal-semiconductor (MS) contact, (ii) Pt/NiO/$n^+$-Si MIS contact, (iii) Pt/$p^+$-Si MS contact, and (iv) Pt/NiO/$p^+$-Si contact. Pt/$n^+$-Si MS contacts and Pt/NiO/$n^+$-Si MIS contacts were fabricated on (100) oriented, 100 Ω-cm p-type CZ c-Si substrates. First, a 100 nm layer of $10^{19}$ $cm^{-3}$ phosphorus doped Si was deposited on the substrate using an Applied Materials Epi2 reduced-pressure-chemical-vapor-deposition (RPCVD) system using dichlorosilane (DCS) with phosphine ($PH_3$) as the dopant source. The deposition temperature was approximately 1000 °C. Second, the TLM area was defined using lithography and

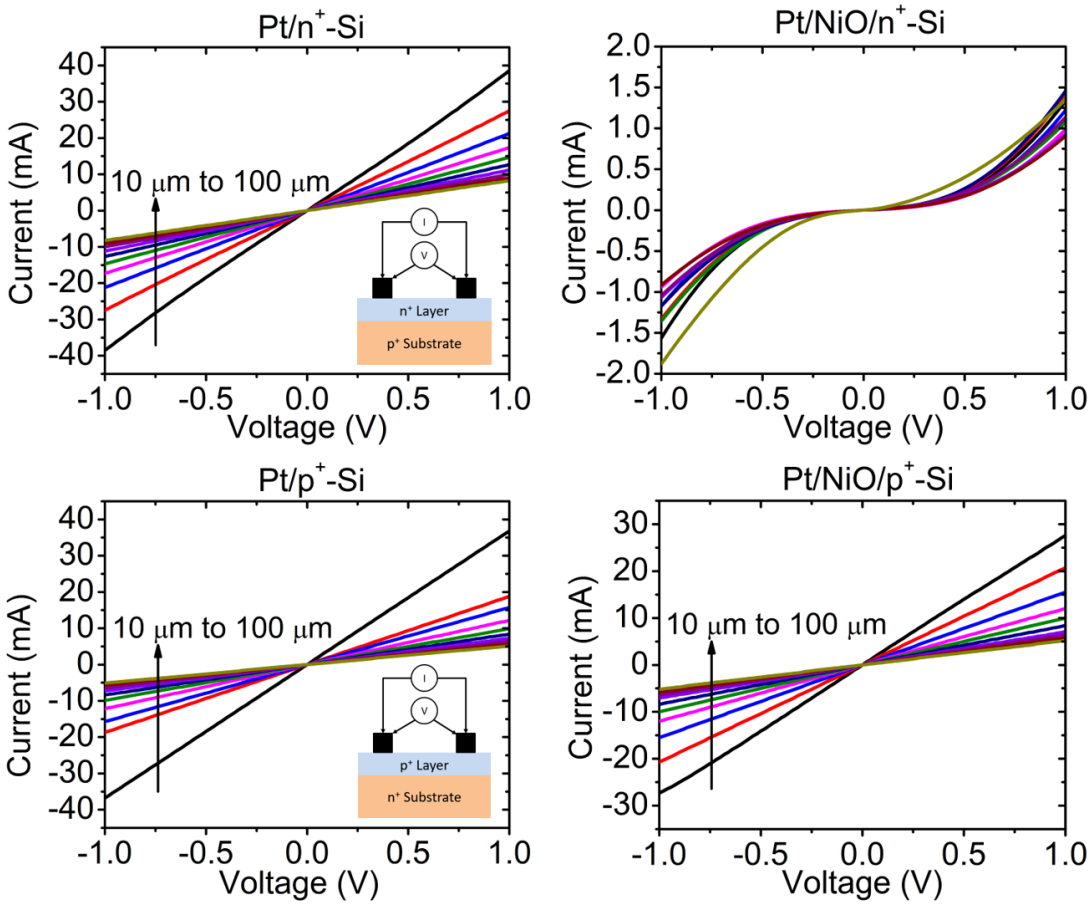


Figure 5.11: Current voltage characteristics of 4 TLM contacts along with the corresponding schematics.

dry etching of Si. Later, the MS and MIS contacts were defined using a lithography process. Finally, the MS and MIS contacts were formed using a sputtering process, followed by a lift-off in acetone. The MS contacts consist of 100 nm of Pt, while the MIS contacts consist of 5 nm NiO followed by 100 nm of Pt. The metal contact distance (d) varies from 10 $\mu$m to 100 $\mu$m linearly, by 10 $\mu$m steps. Before the measurement, the MS and MIS contacts were annealed in forming gas ambient (5% $H_2$ + 95% $N_2$) for 90 s at 350 °C using a rapid-thermal-anneal (RTA) process. The Pt/p-Si MS contacts and Pt/NiO/p-Si MIS contacts were fabricated using the similar process on (100) oriented, 100 Ω-cm n-type CZ c-Si substrates. The 100 nm $10^{19}$ $cm^{-3}$ boron doped $p^+$ layer is deposited in the same system at 1000 °C using DCS and borane ($BH_3$). NiO film was deposited by RF magnetron sputtering at 150 W power in oxygen and Ar ambient from a NiO target. The overall pressure of the chamber during the deposition was kept at 3 mT while the partial pressure of oxygen in the $Ar/O_2$ ambient was maintained at 10% [108].

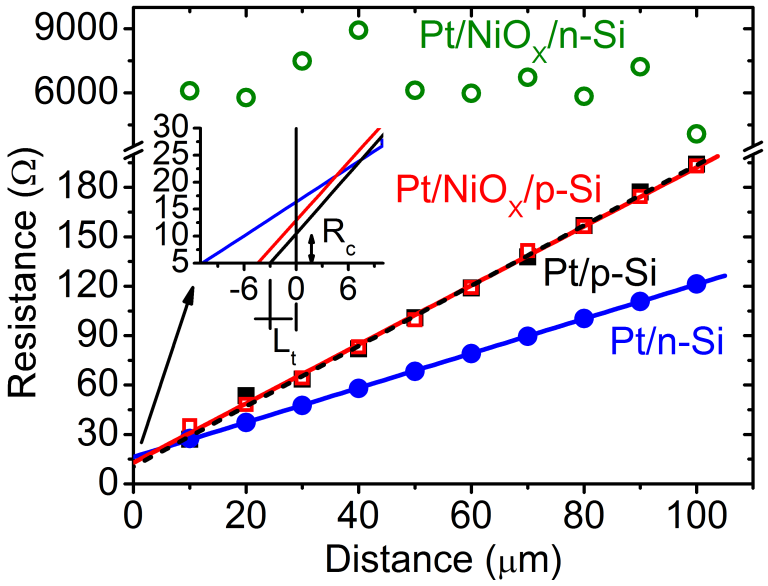


Figure 5.12: Resistance vs. distance curve of the 4 TLM structures to extract $\rho_c$.

## 5.9 Results and Discussion

Table 5.3: Comparison of the contact resistivity (mΩ-cm$^2$) for different contact configurations.

| | Metal Contact | MIS Contact |
|---|---|---|
| n$^+$-Si | 0.25 | Very High |
| p$^+$-Si | 0.02 | 0.01 |

Fig. 5.11 shows the I-V characteristics of the four contact structure. We observe that Pt/NiO/n$^+$-Si contact shows non-ohmic behavior. All the other contacts show highly ohmic behavior. This is because of the high conduction band offset of NiO which blocks the electrons and introduces high tunnel barrier for electrons to pass. For p$^+$-Si, the we do not observe any significant change in the current shape or value. This means that NiO allow holes to pass. We extract the resistance from the slope of these curves at $V = 0$ point and plot it as a function of contact distance d (Fig. 5.12). The inset figure shows the y-axis intercept which represents the contact resistance. We observe that Pt/n$^+$-Si contact shows slightly higher contact resistance whereas with NiO the resistance values are two orders of magnitude higher. The contact resistivity is extracted from Fig. 5.12 and shown in table 5.3. This shows that with the integration of NiO, there is a slight decrease in contact resistivity for holes because of Fermi level depinning effect. However, the contact resistivity for electrons increase significantly. This proves that NiO can enhance the contact selectivity of Si photovoltaic cell.

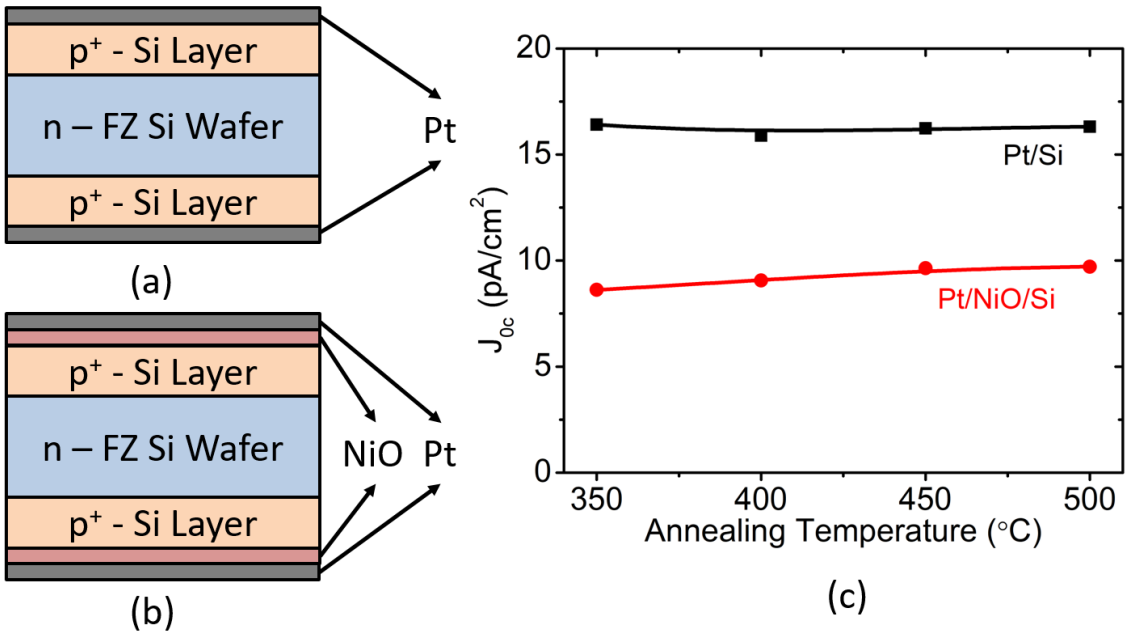


Figure 5.13: Schematic of the lifetime test structure for (a) Pt/Si and (b) Pt/NiO/Si contact and (c) extracted contact recombination factor $J_{0c}$ as a function of anneal temperature.

## 5.10 Lifetime Test Structures for Contact Recombination Study

Contact resistivity, although can provide a good indication of carrier blocking capability, it does not give any indication of the passivation quality at the hetero-interface between oxide and silicon. The efficacy of contact passivation of NiO interlayer is assessed through the contact recombination factor $J_0c$ [109], which is determined from the lifetime test structures. Two types of test structures were fabricated on $10^4$ Ω-cm high quality float-zone (FZ) wafers, as in Fig. 5.13(a) and (b). Next, 100 nm $10^{19}$ $cm^{-3}$ boron doped $p^+$ layers were deposited on both sides of the FZ wafers using the similar RPCVD process described in the previous section. Next, for the Pt/Si test structure, Pt films with 10 nm thickness were deposited on both sides of the sample using sputtering. Such a thin layer of Pt could mimic a device contact, whereas still allowing enough light transmitted into the Si to generate light induced carrier whose lifetime can be measured by the quasi steady-state photoconductance (QSSPC) technique [110]. On the other hand, for the Pt/NiO/Si test structure, 5 nm NiO was deposited on both sides of the sample using the sputtering process followed by a deposition of 10 nm Pt. Later, samples of both the structures were annealed in forming gas ambient (5% $H_2$ in $N_2$) for 90 s from 350 °C to 500 °C using the RTA process to study the dependence of $J_{0c}$ on annealing temperature. After RTA, the effective lifetime was measured by the QSSPC method in a standard Sinton WCT-120 system at room temperature. Finally, the contact recombination factor $J_{0c}$ was

extracted using the Kane and Swanson method [109] with the intrinsic carrier concentration ($n_i$) value of $8.201\times10^9$ $cm^{-3}$ at room temperature [108].

The comparison of $J_{0c}$ of the two structures is shown in Fig. 5.13(c), where the $J_{0c}$ dependence on annealing temperature is shown. For all the annealing temperatures, the $J_{0c}$ of Pt/NiO/Si structure is significantly lower than that of the Pt/Si structure. The as-deposited $J_{0c}$ is too large to measure due to the sputtering damage on the surface. Therefore, the as deposited $J_{0c}$ is not shown in this plot. At 350 °C, the $J_{0c}$ of Pt/NiO/Si is only 8.62 pA/$cm^2$, which is only 52% of the $J_{0c}$ of Pt/Si. This clearly shows the contact passivation effect of the NiO interlayer. For the Pt/Si structure, annealing at different temperatures didnâĂŹt change the $J_{0c}$ significantly showing a relative variation within +/- 1.5%. However, with the addition of NiO layer, the $J_0c$ of Pt/NiO/Si increases from 8.62 pA/$cm^2$ at 350 °C to 9.71 pA/$cm^2$ at 500 °C. Despite the increase with annealing temperature, the $J_{0c}$ in the oxide structure remains significantly smaller that the structure having direct metal contacts. This shows that NiO provides the necessary passivation at the interface with Si to reduce the recombination of minority carrier at the hetero-interface. Therefore, by all the three metric of a selective contact presented in this chapter, nickel oxide is proven to be a great candidate for hole selective/electron blocking contacts to silicon suitable for better carrier management in ultra-thin solar cell.

## 5.11 Summary

In this chapter, techniques for characterizing and benchmarking oxides as carrier selective contacts are shown with a specific example of nickel oxide, which is proven to be an effective hole selective contact to silicon experimentally. Our experiments show NiO can depin the Fermi level to lower the hole barrier height and hence the contact resistivity for holes can be reduced. At the same time due to the higher conduction band offset it provides an enhanced blocking of minority carrier electrons with an additional passivation at the interface to increase the carrier selectivity of the contact.

# Chapter 6

# Contact Selectivity Engineering in Ultra-thin c-Si Solar Cells using Transition Metal Oxides

In this chapter, the integration of metal oxides as carrier-selective contacts for ultra-thin crystalline silicon (c-Si) solar cells is demonstrated which results in 13% relative improvement in efficiency. The improvement in efficiency originates from the suppression of the contact recombination current due to the band offset asymmetry of these oxides with Si. First, an ultra-thin c-Si solar cell having a total thickness of 2 $\mu$m is shown having >10% efficiency without any light trapping scheme. This is achieved by the integration of nickel oxide ($NiO_x$) as a hole-selective contact interlayer material, which has a low valence band offset and high conduction band offset with Si. Second, we show a champion cell efficiency of 10.8% with the additional integration of titanium oxide ($TiO_x$), a well-known material for an electron-selective contact interlayer. Key parameters including $V_{oc}$ and $J_{sc}$ also show different degrees of enhancement if single ($NiO_x$ only) or double (both $NiO_x$ and $TiO_x$) carrier-selective contacts are integrated. The fabrication process for $TiO_x$ and $NiO_x$ layer integration is scalable and shows good compatibility with the device.

## 6.1 Introduction

Crystalline silicon (c-Si) photovoltaic (PV) technology has dominated the PV industry for more than a decade due to its stability, reliability and low cost. Ultra-thin c-Si solar cells have versatile applications and advantages. They provide a feasible pathway towards shrinking the materials cost by allowing utilization of the substrate multiple times [24, 111, 112, 113, 114]. Ultra-thin c-Si can also be integrated onto flexible substrates and show promise for high efficiency tandem cells with the

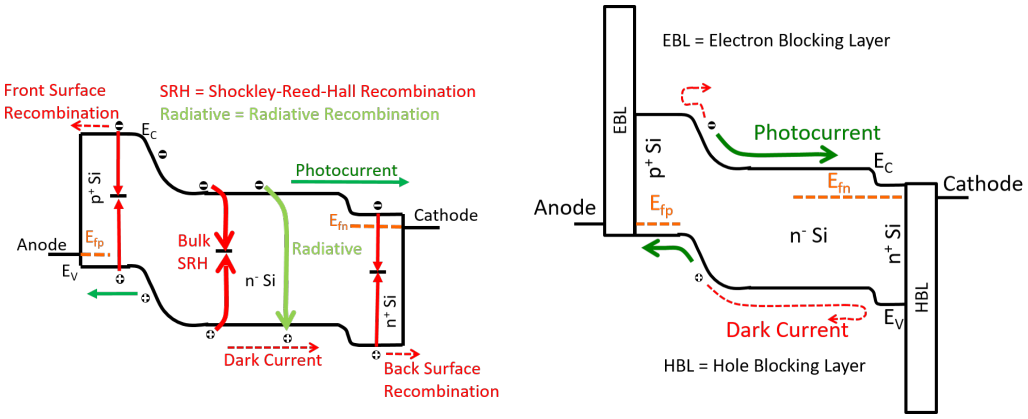


(a) Si p-n junction cell (b) Si solar cell with oxide selective contact

Figure 6.1: (a) Energy band diagram of a p-n junction solar cell showing the recombination mechanisms, (b) energy band diagram of a p-n junction solar cell with selective contacts.

low-cost perovskite semiconductor cells [115, 116, 18]. Unlike the other thin film PV technologies, ultra-thin c-Si technology can ensure higher efficiency at lower cost utilizing both the factors to lower the $/Watt cost.

Ultra-thin c-Si PV technology can also facilitate a significant improvement in energy harvesting for internet-of-things (IoT) sensors through on-chip embedded solar cells [12] or 3-D integration of solar cells onto the IoT sensor chips [11]. As the IoT is becoming a pervasive technology for future, energy harvesting for IoT devices is becoming a real necessity. Powering millions of IoT sensor chips, placed in locations often not accessible by humans, using batteries is not a feasible solution due to high maintenance and disposal costs. Among different energy harvesting technologies, harvesting energy from light (both indoor and outdoor) can provide high energy density [3]. However, on-chip energy harvesting technology faces the challenge of ensuring high efficiency using an ultra-thin absorber where the area is also constrained.

The performance of ultra-thin c-Si solar cells is not only constrained by the limited light absorption, but also the selectivity of the contacts [117, 118, 119] to reach the theoretical efficiency of silicon solar cells [55, 120]. Selectivity of the contact in the context of photovoltaics means the ability of a contact to pass one type of carrier and block the other type. Typically, the formation of a p-n junction provides the required carrier selectivity by creating the built-in electric field. When the solar cell is ultra-thin, the carrier selectivity becomes predominantly limited by the recombination of minority carrier at the contacts [118]. It has been shown that the minority carrier recombination losses at the metal/Si interface significantly reduce the selectivity of the contacts resulting in a degradation of the open-circuit voltage [58]. Fig. 6.1a shows all the dominant recombination mechanisms during the operation of a typical p-n junction solar cell. When the absorber is ultra-thin, the "short" diode assumption determines the reverse saturation current, which is a metric for open

circuit voltage [98]. According to this assumption, an increasing number of minority carriers reach the contact before recombining in the bulk, given that the bulk lifetime is high - a typical scenario for a c-Si cell. Therefore, contact recombination determines the overall performance of the cell.

Moreover, employing light trapping to increase the short-circuit current of an ultra-thin solar cell creates effective carrier confinement inside the solar cell [121, 122, 123], which results in an increase in surface recombination. Therefore, suppressing the minority carrier recombination at the interface under the contacts is of great importance to improve the efficiency of ultra-thin c-Si solar cell. This can be achieved by the insertion of a thin dielectric layer at the metal/Si interface having asymmetric band offsets with Si, i.e. a large band offset for either valence or conduction band and a small band offset for the other (conduction or valence). The material combination is chosen in such a way that a high band offset blocks the minority carrier recombination current at the interface while providing negligible resistance for the majority carriers to the metal contact (Fig. 6.1b).

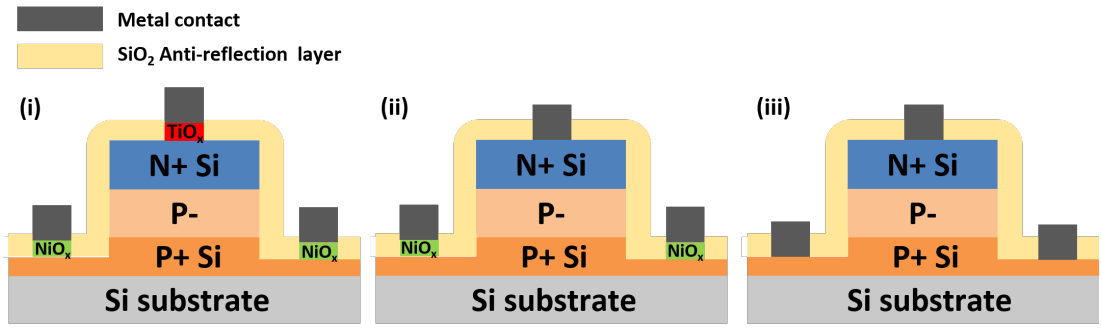


Figure 6.2: Schematic of three groups of 2 $\mu$m thick ultrathin c-Si solar cells - (i) double sided, with both $NiO_x$ and $TiO_x$ carrier-selective contacts on p-contact and n-contact respectively, (ii) single sided, with only $NiO_x$ as hole selective contact on p-contact and (iii) control, no carrier selective contact on either contact.

In this work, we demonstrate $NiO_x$ as an effective electron blocking layer to improve the hole-selectivity of the p-contact of a c-Si ultrathin solar cell. $NiO_x$ is shown to reduce the hole barrier height compared to a metal/Si contact due to Fermi level depinning [49]. It also has low valence band offset and high conduction band offset with Si. Additionally, with p-type conductivity, $NiO_x$ has all the required characteristics to be an effective hole-selective contact interlayer [124, 125]. For n-contacts, $TiO_x$ has already been demonstrated as electron-selective/hole-blocking contact interlayer having the opposite band alignment with Si (high valence band offset/low conduction band offset) [126, 127, 128, 129, 130, 131, 86].

We demonstrate the integration of both $NiO_x$ and $TiO_x$ on an ultra-thin c-Si solar cell having a total thickness of 2 $\mu$m, resulting in a cell efficiency of 10.8% (See Fig. 6.2 for the device cross-section). The integration of these oxides results in a relative improvement of 13% in efficiency compared to a control cell without any oxide selective contacts, demonstrating significant improvement in contact

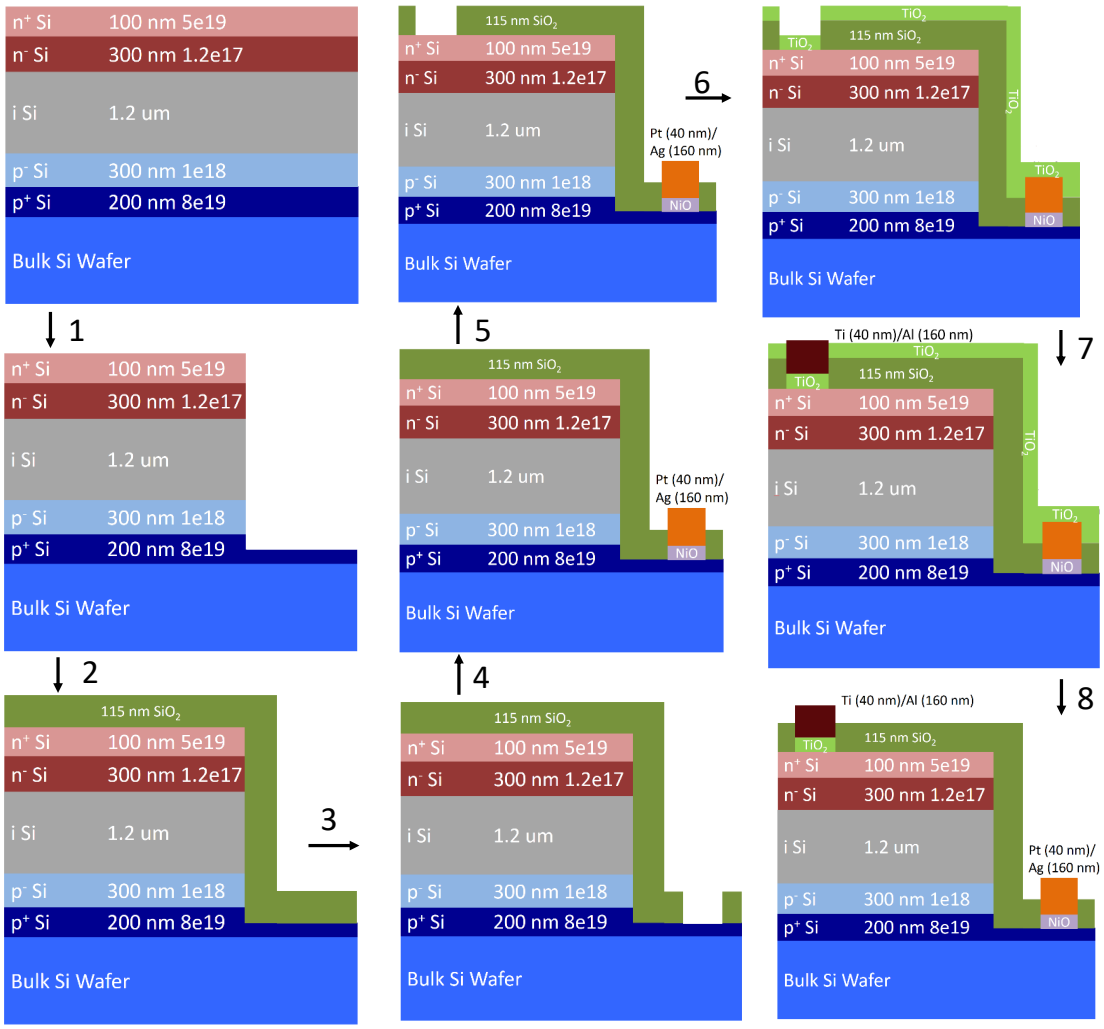


Figure 6.3: Fabrication process flow of the solar cell with oxide selective contacts.

selectivity. The improvement in efficiency is a result of an increase in both the open-circuit voltage and the short-circuit current without using any explicit light trapping techniques. This is a proof that the improvement in contact selectivity results in better carrier collection. Our detailed study also reveals that a forming gas anneal has a significant impact on the improvement in efficiency. Chemical analysis of the interface suggests that during the forming gas anneal, a Pt/$NiO_x$/p-Si contact forms $Ni_xPt_yO$ at the Pt/$NiO_x$ interface by scavenging oxygen from the $SiO_x$ formed at the $NiO_x$/Si interface, and similar effect is observed for Al/$TiO_x$/n-Si contacts. This significantly reduces the overall series resistance of the cell improving the fill factor resulting in higher efficiency.

## 6.2 Experimental Details

### 6.2.1 Device Fabrication

First, the 2 $\mu$m thick c-Si cell active region is epitaxially grown on (100) silicon substrate (boron-doped, 0.1-0.9 $\Omega$-cm resistivity) in a reduced-pressure chemical vapor deposition (RPCVD) system at 1050 °C, in the following order - (i) $p^+$ contact layer (0.2 $\mu$m at $8 \times 10^{19}$ $cm^{-3}$ doping (boron) and 0.3 $\mu$m at $1 \times 10^{18}$ $cm^-3$ doping (boron)), (ii) $p^-$ - absorber layer (1.2 $\mu$m). No dopant gas flow was turned on during the absorber layer deposition (iii) $n^+$ contact layer (0.3 $\mu$m at $1.2 \times 10^{17}$ $cm^{-3}$ doping (phosphorus) and 0.1 $\mu$m at $5 \times 10^{19}$ $cm^{-3}$ doping (phosphorus)). After the epitaxial growth, the first lithography step consists of an active cell area definition using dry etching of Si to a depth of 2 $\mu$m. This step exposes the $p^+$ contact layer for making the bottom contact of the solar cell. Then the c-Si cell is surface passivated by 25 nm thick $SiO_2$ grown by thermal oxidation in dry $O_2$ at 1000 °C, which is followed by a deposition of plasma-enhanced CVD $SiO_x$ forming an anti-reflection coating layer. The total thickness of the $SiO_x$ is controlled to be 115 nm. Then the second lithography step is done to open the $p^+$ contact region by etching the oxide layer using 20:1 buffered oxide etchant (BOE). Then 5 nm $NiO_x$ is deposited directly by electron-beam evaporation followed by 200 nm platinum deposition without breaking the vacuum. The e-beam evaporation of $NiO_x$ is done from $NiO_x$ (99.99%) pellets using an *AJA International, Inc.* evaporator system inside a high vacuum ($< 5 \times 10^{-7}$ mTorr) chamber. Standard lift-off in acetone is used to complete the contact patterning process. Subsequently, a similar patterning technique is used to open the n contact region using BOE oxide etch on the top of the mesa. For the n-contact, a 6 nm thick $TiO_x$ layer is deposited by thermal atomic layer deposition (ALD) at 200 °C. The ALD recipe was composed of alternating pulsing of Tetrakis (dimethylamido)-titanium (TMA-Ti) and $H_2O$ (in steam form). The precursor is kept at 75 °C. The pulsing time is long enough to saturate the surface with the precursor and there is a 15 second gap between the pulsing. The ALD process is followed by the contact region patterning lithography followed by the e-beam evaporation of Titanium (40 nm)/ Aluminum (160 nm) metal stack as the metal contact and subsequent lift-off in acetone. An ion milling process is then used to remove the $TiO_x$ from other regions using metal as the hard mask

(Note that $TiO_x$ is only 5 nm thick, so the metal etching is negligible). The process flow discussed so far can be visualized in Fig. 6.3 with the list of the steps shown as numbers in the figure given below:

1. Mesa etch
2. Oxide passivation
3. Bottom contact window etch
4. $NiO_x$ and bottom contact metal deposition followed by lift-off
5. Top contact window etch
6. $TiO_x$ deposition
7. Top contact metal patterning followed by lift-off
8. $TiO_x$ etch

No surface texturing is introduced to increase the light absorption in this study. All experimental results discussed in the results section are obtained after rapid thermal annealing (RTA) in forming gas (5% $H_2$ + 95% $N_2$) at 450 °C, which is the optimized annealing condition yielding the highest cell efficiency for all the three groups of cells. We fabricated three device splits (Fig. 6.2 - (i), (ii) and (iii)) to have one control (no oxide selective contact), single sided (only $NiO_x$) and double sided (both $NiO_x$ and $TiO_x$). Each cell is 3 mm × 3 mm in dimension. The active area of each device is 0.0221 $cm^2$ after subtracting the shaded area due to the metal contacts.

### 6.2.2 Transmission Electron Microscopy (TEM)

TEM was performed on a FEI 80-300 kV environmental (scanning) transmission electron microscope equipped with a spherical aberration image corrector. Energy-dispersive x-ray spectroscopy (EDS) was performed in STEM mode using an Oxford Xmax SDD Detector. Cross-section samples were fabricated in a FEI Helios Nanolab 600i DualBeam focused ion beam (FIB)/scanning electron microscope (SEM). Amorphous carbon was deposited by an electron beam, then an ion beam to protect the sample from ion beam damage.

### 6.2.3 X-ray Photoemission Spectroscopy (XPS)

XPS was performed on a PHI Versaprobe system, which uses Al (K$\alpha$) radiation (1486 eV). We prepared the sample by depositing $TiO_x$ (6 nm) /Ti (10 nm)/Al (50 nm) on Si (for electron selective contact stack) and $NiO_x$ (5 nm)/ Pt (10 nm) on Si (for hole selective contact stack). During the XPS characterization we started with etching through the layers carefully using an in-situ Ar sputter gun.

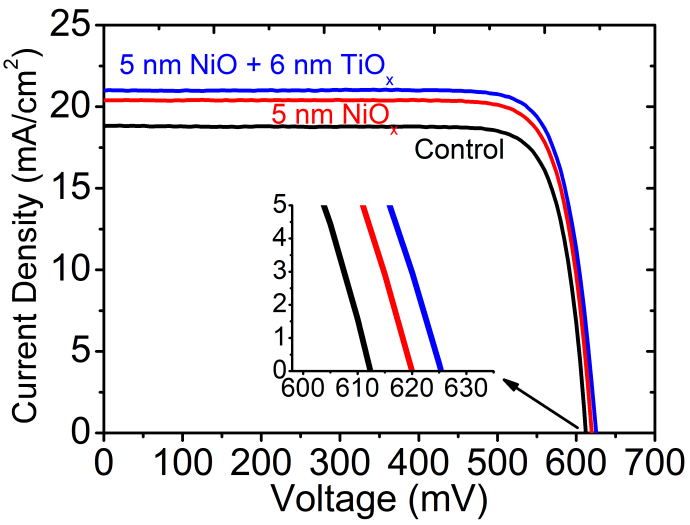


Figure 6.4: J-V characteristics of the champion cells under AM1.5G one sun illumination. The inset figure shows the zoomed-in J-V near open circuit condition to highlight the improvement in $V_{oc}$.

Table 6.1: Cell parameter summary of the device with the highest efficiency for each type of fabricated structure

| | $V_{oc}$ (mV) | $J_{sc}$ (mA/cm$^2$) | FF (%) | Efficiency (%) | $R_s$ (Ω-cm$^2$) |
|---|---|---|---|---|---|
| Control Cell | 612 | 18.8 | 82.5 | 9.5 | 1.50 |
| 5 nm $NiO_x$ | 620 | 20.4 | 82.0 | 10.4 | 1.59 |
| 6 nm $TiO_x$ + 5 nm $NiO_x$ | 625 | 21.0 | 81.9 | 10.8 | 1.72 |

We did alternative etching and measurement to observe different species in the survey spectrum. The etching was done slowly to make sure we did not etch through the oxide layer; sputtering was stopped when the thickness of the top metal layer was such that the signal from the oxide/Si interface is visible. At that point, we probed the whole stack, including the interfacial bonding states. To resolve different bonding states, we fitted the spectra using Lorentz-Gaussian curves.

## 6.3 Results and Discussion

Table 6.2: Average of the cell parameter among many cells from each type of fabricated device

| | $V_{oc}$ (mV) | $J_{sc}$ (mA/cm$^2$) | FF (%) | Efficiency (%) |
|---|---|---|---|---|
| Control Cell | 610 | 18.5 | 82.2 | 9.2 |
| 5 nm $NiO_x$ | 617 | 20.4 | 81.4 | 10.3 |
| 6 nm $TiO_x$ + 5 nm $NiO_x$ | 620 | 20.6 | 82.4 | 10.5 |

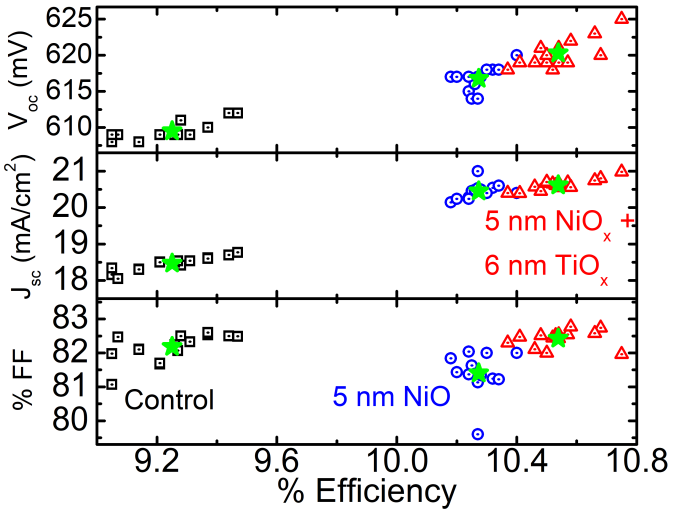


Figure 6.5: Scatter plot of cell performance metrics ($J_{sc}$, $V_{oc}$ and %FF) as a function of efficiency comparing the statistical distribution of cell performance. The green stars represent the average of the corresponding clusters.

### 6.3.1 Characterizing Cell Performance under Sun Simulator

The current density-voltage (J-V) experimental results under 1 sun illumination (AM 1.5G) for the champion cells obtained from each of the fabricated devices are shown in Fig. 6.4, with the key parameters summarized in Table 6.1. It is clearly shown that the cell efficiency improves from 9.5% to 10.3% when only NiOx is introduced as a hole-selective layer, and from 9.5% to 10.8% when both TiOx and NiOx carrier-selective layers are introduced, achieving a substantial efficiency for the current sub 5 $\mu$m c-Si solar cells [132, 133]. The reduction in contact recombination of minority carriers is supported by the corresponding open circuit voltage ($V_{oc}$) enhancement. The $V_{oc}$ of the champion device is 625 mV with both the n- and p-contact passivated with carrier-selective interlayers.

To show the statistical distribution of the device performance enhancement for different cells having double sided and single sided selective contacts compared to the control group, the scatter plot of the cell performance metrics (Voc, Jsc and %FF) as a function of the corresponding efficiency is shown in Fig. 6.5, with the average value of key parameters summarized in Table 6.2.

The scatter plot confirms that the improvement from integrating oxide materials as selective contact is consistent across multiple devices fabricated on a single wafer. Table 6.1 also reveals the trade-off for using oxide as selective contact. Since each oxide introduces a small additional series resistance, we observe a decrease in the fill factor (% FF). However, this decrease is over compensated by the improvement in both the $V_{oc}$ and $J_{sc}$, resulting in an overall improvement in efficiency. Table 6.2 shows significant improvement in the average cell efficiency with a tight spread

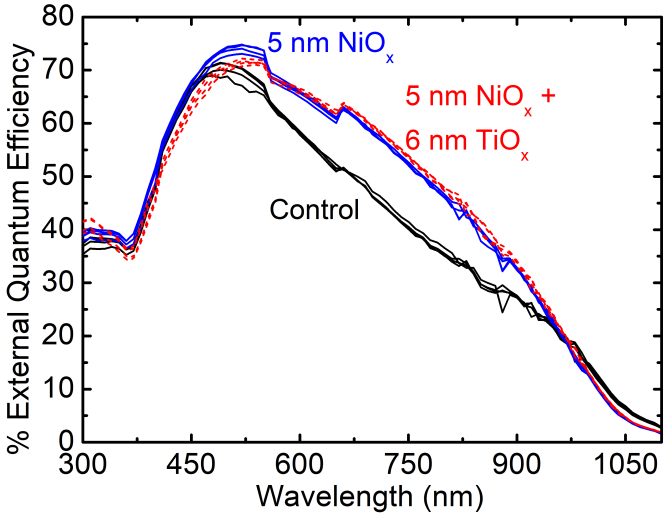


Figure 6.6: External quantum efficiency (EQE) as a function of wavelength showing comparison between three groups of fabricated cells - control (black), single sided selective contact (blue), double sided selective contact (red).

seen in the cell performance distribution scatter plot (Fig. 6.5. This proves that the improvement from incorporating the oxide selective contacts is more than the typical process variations.

### 6.3.2 External Quantum Efficiency (EQE)

Oxide selective contacts not only improve the contact passivation (as evidenced by the improvement in $V_{oc}$), but also the relative band offset of $NiO_x$ and $TiO_x$ with Si, leads to better carrier extraction (as evidenced by the improvement in $J_{sc}$). To study the carrier extraction in detail, the external quantum efficiency (EQE) was also characterized in the short circuit condition, as shown in Fig. 6.6. From the EQE result, it is observed that when either single or double carrier selective contacts are inserted, the EQE is significantly improved in the wavelength range from 500 nm to 950 nm. This improvement in EQE is due to better extraction of carrier into the contacts, which explains the $J_{sc}$ enhancement in Table 6.1 & 6.2. The $J_{sc}$ of the samples with single- and double-sided carrier selective contacts shows a relative improvement of 11 % compared to the control cells without carrier selective contacts. The Jsc increases from 18.5 $mAcm^{-2}$ to 20.4 $mAcm^{-2}$ and 20.6 $mAcm^{-2}$, respectively on average. However, for wavelengths below 500 nm, the EQE result for these three groups of cells are very similar. The reason is that surface recombination dominates the total loss for the shorter wavelengths, which results in the EQE being relatively insensitive to the improvement of contact recombination.

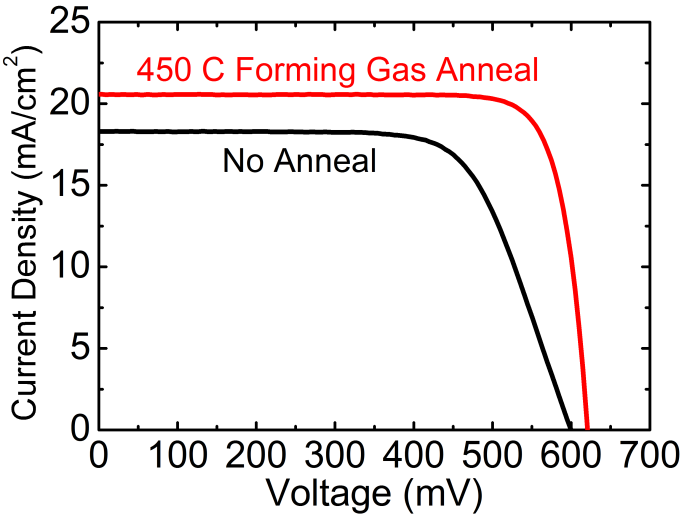


Figure 6.7: J-V characteristics of the cell containing double sided selective contact before and after forming gas annealing at 450 °C for 90 sec.

### 6.3.3 Effect of Annealing on Cell Performance

Through various annealing iterations, we found the optimized annealing condition for the cells, which is forming gas annealing at 450 °C for 90 seconds. The cell J-V before and after annealing at the optimized condition are compared in Fig. 6.7. This figure clearly suggests that the improvement in cell performance arises from the lowering of the overall series resistance improving both the $J_{sc}$ and % FF. Only the cell performance having double sided selective contact is shown here, but the other groups of fabricated devices show similar performance gain from forming gas annealing. The detailed mechanism of the forming gas annealing in cells containing oxide selective contacts is studied using transmission electron microscopy and X-ray photoemission spectroscopy.

### 6.3.4 Transmission Election Microscopy (TEM)

The device structure before and after forming gas anneal was observed using transmission electron microscopy (TEM) in both parallel beam illumination and scanning transmission (STEM) mode. In the non-annealed Si/$SiO_x$/$TiO_x$/Ti/Al sample (Fig. 6.8a), we observe, from left to right, the Si substrate, a 2 nm amorphous layer, a 6 nm amorphous layer that is distinct from the first, and finally the metal top-contact. The same sample after the forming gas anneal is shown in Figure Fig. 6.8b. Two main changes occur because of the anneal - First, Moiré contrast in the oxide layer closest to the substrate indicates overlapping polycrystalline grains and is consistent with $TiO_x$ crystallization, and second, contrast changes in the metal contact indicate some grain growth, which is expected [134]. The non-annealed Si/$SiO_x$/$NiO_x$/Pt sample (Fig. 6.8c) is very similar to the non-annealed Si/$SiO_x$/$TiO_x$/Ti/Al sample. The layers are, from left to right, the Si substrate, a 4

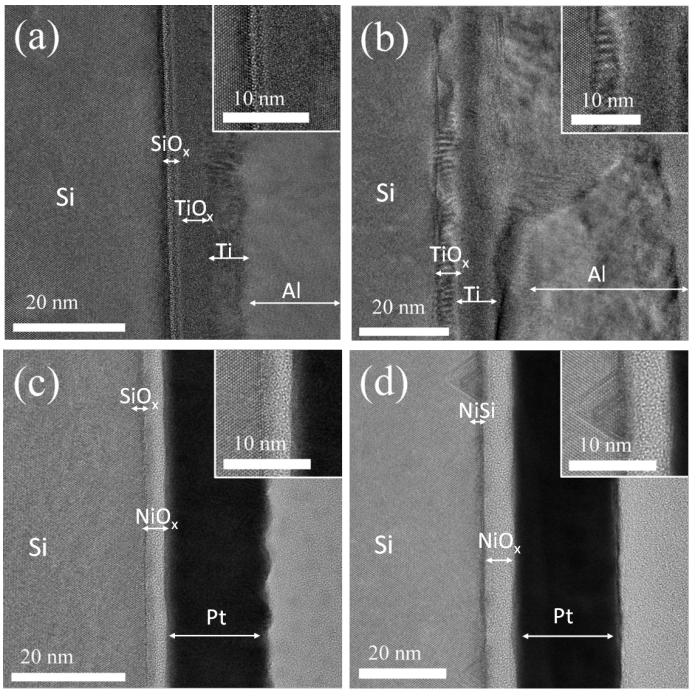


Figure 6.8: Aberration corrected [110] zone axis high resolution transmission electron microscope images of (a) non-annealed Si/$SiO_x$/$TiO_x$/Ti/Al, (b) 450 °C forming gas annealed Si/$SiO_x$/$TiO_x$/Ti/Al, (c) non-annealed Si/$SiO_x$/$NiO_x$/Pt, and (d) 450 °C forming gas annealed Si/$SiO_x$/$NiO_x$/Pt.

nm amorphous layer with two regions of slightly differing contrast, and the metal top-contact. The differing contrast in the amorphous layer can be attributed to uniformity variations in the $NiO_x$ layer, which is electron-beam evaporated. The same sample after forming gas anneal (Fig. 6.8d) develops dark triangular precipitate structures with re-entrant surfaces, although other aspects of the sample are relatively unchanged.

### 6.3.5 X-ray Energy Dispersion Spectroscopy (EDS)

Elemental composition of the different layers in the TEM samples was analyzed using x-ray energy dispersive spectroscopy (EDS) in STEM mode. In many of the samples, Ga-K x-rays are observed ( 9.24 kV), which is typical for FIB prepared TEM samples. Cu-K ( 8.04 kV, 8.91 kV) and C-K ( 0.277 kV) x-rays are also observed due to the Cu TEM grid and adventitious carbon on the sample. For the non-annealed Si/$SiO_x$/$TiO_x$/Ti/Al and Si/$SiO_x$/$NiO_x$/Pt samples, the EDS confirms the expected structures (Figures 6.9a- 6.10a). After 450 °C rapid thermal annealing in forming gas, the interfacial O-K x-ray signal from the native oxide layer is significantly decreased in the Si/$SiO_x$/$TiO_x$/Ti/Al samples. This can be attributed to the reducing effect of the forming gas anneal as well as oxygen

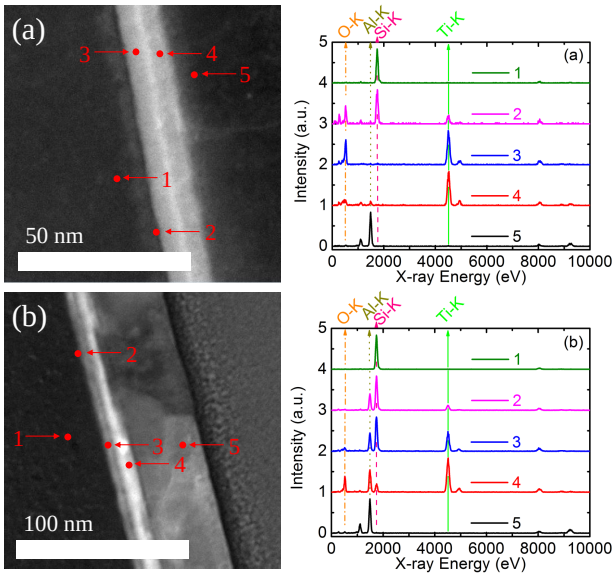


Figure 6.9: Scanning transmission electron microscopy images showing the elemental analysis location (1-5) (left) and the spectra of spatially resolved x-ray energy dispersive spectroscopy on those locations (right) for (a) unannealed $Si/SiO_x/TiO_x/Ti/Al$, and (b) 450 °C forming gas annealed $Si/SiO_x/TiO_x/Ti/Al$.

scavenging due to the $TiO_x$ layer above [135] where Ti is reacting with O [136]. Furthermore, the O-K x-ray signal in the $TiO_x$ is observed to increase with increasing distance from the substrate. The O-K x-ray signal in the substrate/oxide interface of the $Si/SiO_x/NiO_x/Pt$ sample is also decreased after 450 °C rapid thermal annealing. In addition, triangular Ni- and Si-rich silicide phase precipitate structures with re-entrant surfaces are formed on the substrate surface. For both samples after annealing, the oxide layer closest to the metal top-contact remained oxygen rich (Figures 6.9b-6.10b). For $TiO_x$ and $NiO_x$ selective contacts, the forming gas anneal resulted in reduction of interface silicon oxide at the substrate/oxide interface, while preserving the metal oxide selective contact. This is consistent with our observation that device efficiency increases and device resistance decreases after the 450 °C anneal in forming gas.

### 6.3.6 X-ray Photoemission Spectroscopy (XPS)

To study the effect of annealing and how it affects the interface, we have performed X-ray photoemission spectroscopy (XPS) of the original hole selective and electron selective contact stacks. The detailed spectra of two different contact stacks are shown in Figures 6.11 & 6.12. Fig. 6.11 shows the spectra of (a) Si 2p, (b) Pt 4f and (c) Ni 2p. In the spectra of Si, we see a suppression of the peak at 103 eV with forming gas annealing. This peak corresponds to the Si-O bond for near-stoichiometric

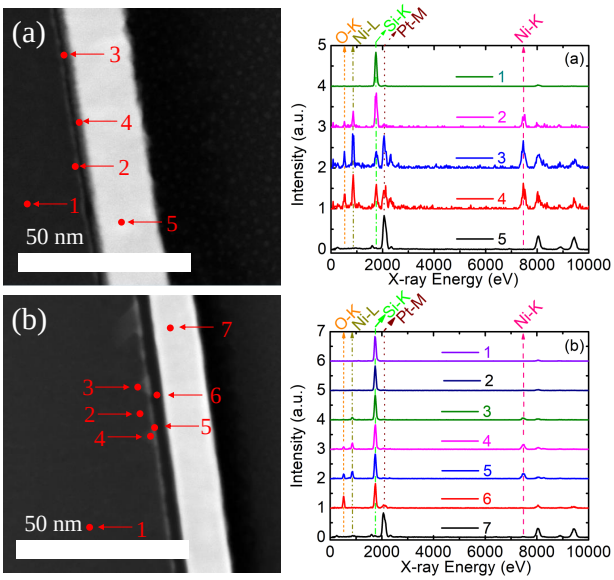


Figure 6.10: Scanning transmission electron microscopy images showing the elemental analysis location (1-7) (left) and the spectra of spatially resolved x-ray energy dispersive spectroscopy on those locations (right) for (a) non-annealed Si/$SiO_x$/$NiO_x$/Pt, and (b) 450 °C forming gas annealed Si/$SiO_x$/$NiO_x$/Pt.

$SiO_x$. Therefore, we can conclude that as-deposited $NiO_x$ forms a thin layer of $SiO_x$ layer at the interface, which is the source of tunneling resistance. Forming gas annealing removes this oxide. Fig. 6.11b suggests that the removal of $SiO_x$ is influenced by the presence of the Pt layer directly in contact with $NiO_x$. The as-deposited sample shows a metallic Pt peak along with the existence of Pt-O bonds. This is further corroborated by the presence of metallic Ni in the Ni 2p spectra of the as-deposited sample (Fig. 6.11c). We hypothesize that at the interface between NiO and Pt, Ni-Pt complex oxide is formed ($Ni_xPt_3O_4$) [137]. Although the formation of this oxide requires a relatively higher temperature, the atoms during the e-beam evaporation are energetic when they arrive at the sample surface. It has been shown that Pt oxides with metals all have metallic-like conduction [137, 138, 139] resulting in a reduction in overall series resistance of the cell. In this process, the Ni to O ratio does not change significantly, so the mechanism of forming gas annealing of Si/$NiO_x$/Pt stack is to reduce the $SiO_x$ at the $NiO_x$/Si interface and to form Ni-Pt oxide at the $NiO_x$/Pt interface, which reduces the tunneling resistance. This is consistent with the observed STEM EDS, which shows reduced oxide at the Si/$NiO_x$ interface after a forming gas anneal.

Similarly, Fig. 6.12 shows the spectra of (a) Ti 2p, (b) O 1s and (c) Si 2p for Ti/$TiO_x$/Si electron selective contacts. Since $TiO_x$ is covered with Ti, which acts as oxygen scavenging material [135], we

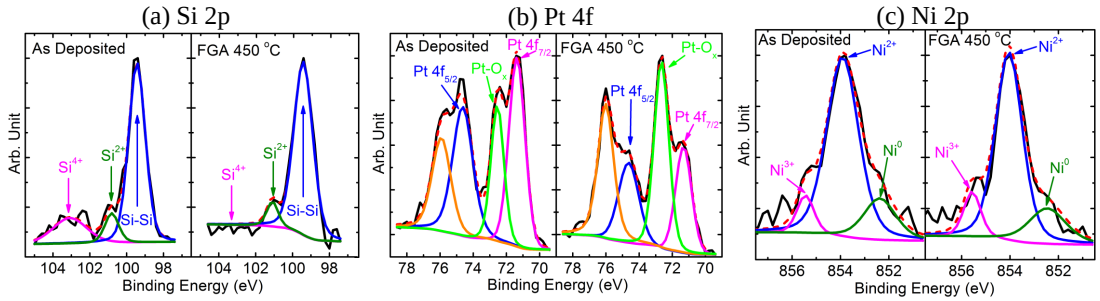


Figure 6.11: Elemental XPS spectra of (a) Si 2p (b) Pt 4f and (c) Ni 2p for Pt/$NiO_x$/Si interface before and after forming gas anneal at 450 °C for 90 sec.

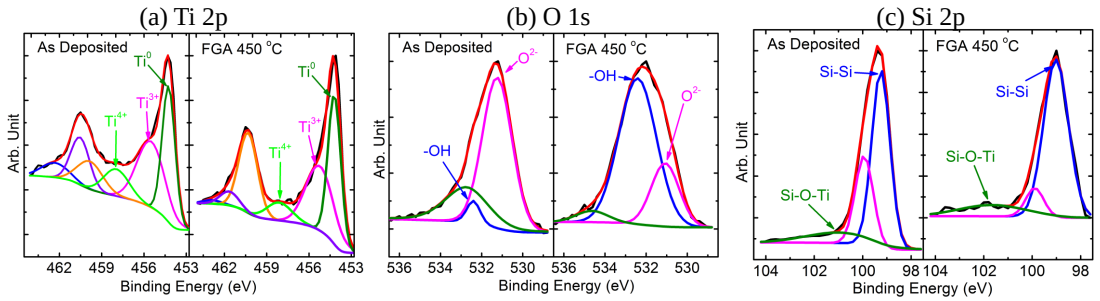


Figure 6.12: Elemental XPS spectra of (a) Ti 2p (b) O 1s and (c) Si 2p for Ti/$TiO_x$/Si interface before and after forming gas anneal at 450 °C for 90 sec.

see the presence of both $Ti^{4+}$ and $Ti^{2+}$ in the Ti 2p spectra (Fig. 6.12a). This indicates that the as-deposited sample contains oxygen-vacancy dominated $TiO_2$ that is n-type in nature. With forming gas annealing, the $Ti^{4+}$ peak gets smaller with respect to the $Ti^{3+}$ peak. This is also confirmed by the increase in -OH peak associated with H annealing at higher temperature (Fig. 6.12b). This increase in -OH also passivates the interface between Si/$TiO_x$ [140]. Since Ti getters oxygen from the Si/$TiO_x$ interface, we see a very weak peak signifying Si-O-Ti bonding at the interface (Fig. 6.12c). As a result, the improvement in the contacts originates from the removal of $SiO_x$ at the hole-selective contact interface and the increase in oxygen vacancy concentration in $TiO_x$.

## 6.4 Conclusion

In this chapter, we have demonstrated an ultra-thin c-Si solar cell with metal oxide selective contact that shows an efficiency of 10.8%. Nickel oxide has been shown to block the electrons while working as a hole contact, and titanium oxide has been demonstrated to block holes while working as an electron contact. Detailed study by TEM and XPS shows that forming gas annealing reduces the interfacial $SiO_x$ layer and lowers the tunneling resistance. The asymmetric band offset in each

contact improves the open circuit voltage significantly. Also, since the carrier collection improves, we see an improvement in the short circuit current. This cell shows significant improvements in performance without any explicit light trapping techniques. The improvement arises from better carrier management. This work also shows the importance of contact improvement in ultra-thin silicon solar cells.

# Chapter 7

# Future Work and Summary of Contributions

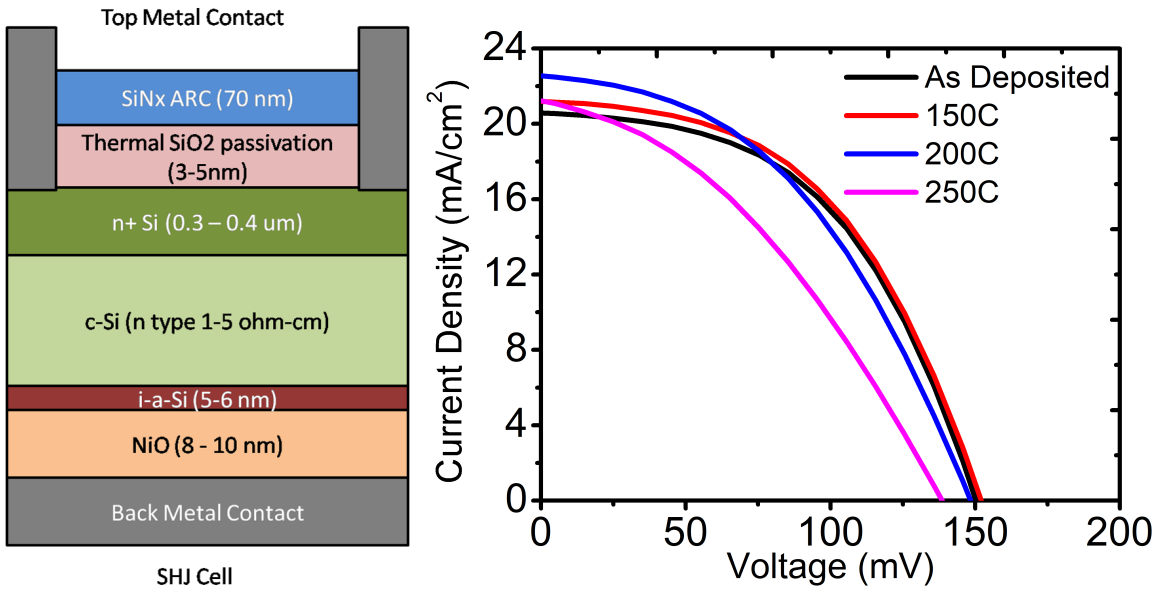


(a) (b)

Figure 7.1: (a) The schematic of the heterojunction cell with NiO on the back of low doped Si absorber (b) Current voltage characteristics of NiO/n-Si heterojunction cell under 1-sun condition for different annealing temperature.

## 7.1 Future Work on Heterojunction Solar Cells

In chapter 2, we have introduced heterojunction solar cell without any highly doped $p^+$ and n+ layer. The oxide heterojunction directly with low doped Si absorber would provide the necessary contact selectivity with added benefit of removing high doped homojunction, which is the bulk recombination region. In chapter 3, we have presented the optimization of the heterojunction contact using oxides. Finally in chapter 6 we have shown the proof-of-concept cell showing the integration of nickel oxide (NiO) as the hole selective contact layer experimentally.

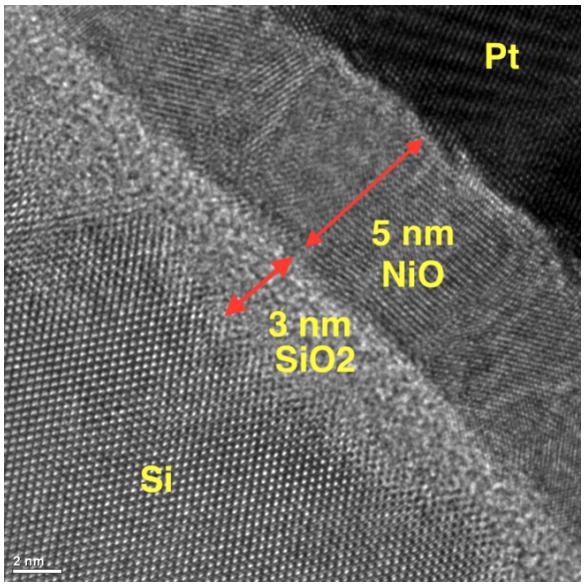


Figure 7.2: Cross-sectional TEM image of Pt/NiO/Si heterostructure contact showing significant $SiO_x$. The reason for $SiO_x$ formation is the oxidizing environment seen by Si during sputtering.

In future, true heterojunction solar cell with oxide contact directly integrated with c-Si absorber material needs to be shown, specifically with NiO that demonstrate $>$ 10 % efficiency for a thin c-Si absorber. Integration of oxide on low doped c-Si absorber material poses experimental challenges beyond what is considered in the previous chapters during optimization. One of the most challenging task is to ensure excellent contact passivation between NiO and Si. Hydrogenated intrinsic amorphous Si provides some of the best quality passivation to Si that resulted in the current world record of 26.3% efficiency for a terrestrial solar cell device [141]. Initially a-Si was thought to be useful for passivating NiO/Si interface as well. That is why the cell structure of Fig. 7.1a was fabricated to characterize the performance of heterojunction solar cell with nickel oxide. The details of the fabrication are beyond the scope of this chapter. However, the current-voltage characteristic measurement of the cell reveals very poor performance (Fig. 7.1b) for all annealing condition. The annealing was performed on a hot plate. Analyzing the J-V characteristics shows that the short

circuit current remains very high while the open circuit voltage and the fill factor is significantly reduced. For the best performing cell, $V_{oc}$ = 152 mV and $J_{sc}$ = 21.20 mA/cm$^2$ and FF = 49.15% resulting in an efficiency of 1.58 %. The low values of FF suggests that there is a barrier for carrier extraction although NiO depins the Fermi level. Perhaps, the positive tunnel barrier shown to the majority carrier holes by the NiO might be a problem.

Most importantly, our TEM results (Fig. 7.2) show that there is indeed some $SiO_x$ formation at the interface which acts as a tunnel barrier and minority carrier recombination center at the same time due to its defective nature. In future, the performance of this cells can be improved by studying the interface passivation properties of NiO and Si systematically. Also, the development of a technique to prevent $SiO_x$ formation at the interface is necessary. Additionally, high doping in Si solar cell provides the necessary band bending to deflect the carrier away from the interface. In this case, that can only be done by high doping in oxides and/or finding unconventional materials to shift the Fermi level of the contacts near the conduction band (electron selective) and near the valence band (hole selective). Also, the study of how Fermi level pinning changes with sub-stoichiometric oxide is of importance because it can provide important insight about the barrier height of photogenerated holes and other contact selectivity properties.

III-V materials like GaAs is another potential material for high performance solar cell. For III-V cells, the absorber material required is significantly thinner than Si. In this case, oxide selective contact could be useful. In fact our simulation [57] suggests that the improvement in GaAs solar cell from oxide selective contact is significant because the bulk lifetime is generally very high. Usually III-V cells use some kind of heterojunction as a window layer for contacts where other lattice matched III-V is used. Using amorphous transition metal oxides can remove the stringent requirement of lattice matching.

### 7.1.1 Towards Ultimate Thin Solar Cell using 2D Materials

Two dimensional materials from transition metal dichalcogenides ($MoS_2$, $WSe_2$, $WS_2$ etc.) have interesting optical properties that makes them good absorber of light even with a few monolayers. Therefore integrating oxide contacts to make double heterojunction solar cell would be a useful contribution for the future study of chip integrated ultra-thin photovoltaics. Also, it has been shown that Van der Waals heterostructures between multiple TMD materials having specific band alignment with each other can also provide significant improvement in solar enery harvesting by the TMD materials [142]. This is an exciting field of future research that can have a lot of practical impact.

## 7.2 Summary of the Thesis

Finally, as a summary of the thesis, the important contribution of this research work is given below -

- A systematic study to compare the performance of solar cells for different contact configurations
- Experimental characterization of Fermi level pinning in NiO and introduced a contact resistivity based characterization technique for contact selectivity determination
- Demonstrated a post-deposition UV/ozone exposure technique to alter stoichiometry in NiO resulting in p-doping
- Integrated NiO as hole selective contacts to solar cells demonstrating 13% relative improvement in performance.
- Experimentally shown greater than 10% efficiency from a thin ($< 10$ $\mu$m) c-Si solar cell.

## 7.3 Summary of Contributions

List of publications resulted from this work.

### 7.3.1 Journals

- R. Islam, G. Chen, P. Ramesh, N. Fuchigami, D. Lee, K. Littau, K. Weiner, R. T. Collins, K. C. Saraswat, Investigation of the Changes in Electronic Properties of Nickel Oxide ($NiO_x$) due to UV/Ozone Treatment, ACS Applied Materials and Interfaces, 2017, 9 (20), pp 17201-17207.

- N. El-Atab, T. G. Ulusoy, A. Ghobadi, J. Suh, R. Islam, A. K. Okyay, K. Saraswat, and A. Nayfeh, Cubic-phase zirconia nano-islands growth using atomic layer deposition and application in low-power charge-trapping nonvolatile-memory devices, Nanotechnology, 2017 (accepted, in-press).

- R. Islam, K. N. Nazif and Krishna C. Saraswat, Si Heterojunction Solar Cells: A Simulation Study of the Design Issues, IEEE Transactions on Electron Devices, vol. 63, no. 12, Dec. 2016.

- R. Islam, G. Shine and Krishna C. Saraswat, Schottky Barrier Height Reduction for Holes by Fermi Level Depinning using Metal/Nickel Oxide/Silicon Contacts, Applied Physics Letters, vol. 105, no. 18, Nov. 2014.

- M. Xue*, R. Islam*, A. C. Meng*, Z. Lyu, C.-Y. Lu, C. Tae, M. R. Braun, K. Zang, P. C. McIntyre, T. I. Kamins, K. C. Saraswat, J. Harris, Contact Selectivity Engineering in 2 $\mu$m Thick Ultrathin c-Si Solar Cell using Transition Metal Oxides Achieving Efficiency of 10.8%, ACS Applied Materials and Interfaces, 2017 (under review, *equal contribution).

### 7.3.2 Conferences

- M. Xue, Y. Chen, R. Islam, J. Chen, C.-Y. Lu, Z. Lyu, K. Zang, J. Jia, H. Deng, Y. Huo, T. Kamins, K. Saraswat, J. Harris, Ultra-Thin Crystalline Silicon Solar Cells with Nickel Oxide Interlayer as Hole-selective Contact, $44^{th}$ IEEE Photovoltaic Specialist Conference, Washington, DC, Jun. 2017.

- R. Islam, K. N. Nazif, K. Saraswat, Optimization of Selective Contacts in Si Heterojunction Photovoltaic Cells Considering Fermi Level Pinning and Interface Passivation, $43^{rd}$ IEEE Photovoltaic Specialist Conference, Portland, OR, Jun. 2016.

- R. Islam, G. Chen, P. Ramesh, R. Collins, K. Saraswat, Resistivity Control of Nickel Oxide by Defect Doping Through UV/Ozone Treatment, MRS Spring Meeting, Phoenix, AZ, Mar. 2016.

- R. Islam, N. Fuchigami, P. Ramesh, D. Lee, K. Littau, K. Weiner, K. Saraswat, Tuning Stoichiometry in Atomic Layer Deposited $NiO_x$ by Changing Deposition Temperature, MRS Spring Meeting, Phoenix, AZ, Mar. 2016.
- P. Ramesh, R. Islam, D. Lee, K. Weiner, K. Saraswat, Control of Resistivity and Stoichiometry in Atomic Layer Deposited Titanium Dioxide Using Rapid Thermal Annealing, MRS Spring Meeting, Phoenix, AZ, Mar. 2016.
- R. Islam, P. Ramesh, J. H. Nam and K. C. Saraswat, Nickel Oxide Carrier Selective Contacts for Silicon Solar Cells, $42^{th}$ IEEE Photovoltaic Specialist Conference, New Orleans, LA, Jun. 2015.
- S. Deshmukh, R. Islam, C. Chen, E. Yalon, K. C. Saraswat, E. Pop, Thermal Modeling of Metal Oxides for Highly Scaled Nanoscale RRAM, The 2015 International Conference on Simulation of Semiconductor Processes and Devices (SISPAD), Washington, DC, Sep. 2015.
- R. Islam and Krishna C. Saraswat, Metal/Insulator/Semiconductor Carrier Selective Contacts for Photovoltaic Cells, $40^{th}$ IEEE Photovoltaic Specialist Conference, Denver, CO, Jun. 2014.

# Bibliography


[1] http://www.libelium.com/resources/top_50_iot_sensor_applications_ranking/.

[2] J. Bryzek, "Tsensor summit." http://mediax.stanford.edu/news/tsensors-summit, Oct. 2013.

[3] M. Raju and M. Grazier, "Energy Harvesting ULP Meets Energy Harvesting: A Game-changing Combination for Design Engineers," tech. rep., Texas Instruments, Apr. 2010. White Paper.

[4] G. Xu, W. Shen, and X. Wang, "Applications of wireless sensor networks in marine environment monitoring: A survey," *Sensors*, vol. 14, no. 9, pp. 16932–16954, 2014.

[5] Y. Jiber, H. Harroud, and A. Karmouch, "Precision agriculture monitoring framework based on WSN," in *2011 7th International Wireless Communications and Mobile Computing Conference*, pp. 2015–2020, July 2011.

[6] A. E. Kouche, L. Al-Awami, H. Hassanein, and K. Obaia, "WSN application in the harsh industrial environment of the oil sands," in *2011 7th International Wireless Communications and Mobile Computing Conference*, pp. 613–618, July 2011.

[7] A. S. G. Andrae and T. Edler, "On global electricity usage of communication technology: Trends to 2030," *Challenges*, vol. 6, no. 1, pp. 117–157, 2015.

[8] "Energy harvesting wireless power for the internet of things," tech. rep., EnOcean GmBH, Aug. 2015.

[9] http://batteryuniversity.com/learn/article/recycling_batteries.

[10] A. Perea, C. Honeyman, S. Kann, A. Mond, M. Shiao, J. Jones, S. Moskowitz, C. Smith, B. Gallagher, S. Rumery, A. Holm, K. O'Brien, and J. Baca, "US solar market insight report Q2," tech. rep., Wood Mackenzie, Ltd./Solar Energy Industries Association (SEIA), 2017.

[11] F. K. Hsueh, C. H. Shen, J. M. Shieh, K. S. Li, H. C. Chen, W. H. Huang, H. H. Wang, C. C. Yang, T. Y. Hsieh, C. H. Lin, B. Y. Chen, Y. S. Shiao, G. W. Huang, O. Y. Wong, P. H. Chen, and W. K. Yeh, "First fully functionalized monolithic 3D+ IoT chip with 0.5 V light-electricity power management, 6.8 GHz wireless-communication VCO, and 4-layer vertical ReRAM," in *2016 IEEE International Electron Devices Meeting (IEDM)*, pp. 2.3.1–2.3.4, Dec. 2016.

[12] C. Y. Wu, W. J. Sung, P. H. Kuo, C. K. Tzeng, C. C. Chiao, and Y. C. Tsai, "The design of CMOS self-powered 256-pixel implantable chip with on-chip photovoltaic cells and active pixel sensors for subretinal prostheses," in *2015 IEEE Biomedical Circuits and Systems Conference (BioCAS)*, pp. 1–4, Oct 2015.

[13] A. U. Rehman, S. H. Lee, and S. H. Lee, "Crystalline silicon thin-film solar cells on ceramic substrates," *Electronic Materials Letters*, vol. 11, pp. 295–302, Mar 2015.

[14] J. Haschke, D. Amkreutz, L. Korte, F. Ruske, and B. Rech, "Towards wafer quality crystalline silicon thin-film solar cells on glass," *Solar Energy Materials and Solar Cells*, vol. 128, pp. 190 – 197, 2014.

[15] R. Brendel, "Review of layer transfer processes for crystalline thin-film silicon solar cells," *Japanese Journal of Applied Physics*, vol. 40, no. 7R, p. 4431, 2001.

[16] S. Mokkapati and K. R. Catchpole, "Nanophotonic light trapping in solar cells," *Journal of Applied Physics*, vol. 112, no. 10, p. 101101, 2012.

[17] F. K. Shaikh and S. Zeadally, "Energy harvesting in wireless sensor networks: A comprehensive review," *Renewable and Sustainable Energy Reviews*, vol. 55, pp. 1041 – 1054, 2016.

[18] P. Kowalczewski, L. Redorici, A. Bozzola, and L. C. Andreani, "Silicon solar cells reaching the efficiency limits: from simple to complex modelling," *Journal of Optics*, vol. 18, no. 5, p. 054001, 2016.

[19] P. Campbell and M. A. Green, "Light trapping properties of pyramidally textured surfaces," *Journal of Applied Physics*, vol. 62, no. 1, pp. 243–249, 1987.

[20] P. Campbell, "Enhancement of light absorption from randomizing and geometric textures," *J. Opt. Soc. Am. B*, vol. 10, pp. 2410–2415, Dec 1993.

[21] P. Campbell, S. Wenham, and M. Green, "Light trapping and reflection control in solar cells using tilted crystallographic surface textures," *Solar Energy Materials and Solar Cells*, vol. 31, no. 2, pp. 133 – 153, 1993.

[22] K. J. Weber and A. W. Blakers, "A novel silicon texturization method based on etching through a silicon nitride mask," *Progress in Photovoltaics: Research and Applications*, vol. 13, no. 8, pp. 691–695, 2005.

[23] S. B. Mallick, M. Agrawal, and P. Peumans, "Optimal light trapping in ultra-thin photonic crystal crystalline silicon solar cells," *Opt. Express*, vol. 18, pp. 5691–5706, Mar 2010.

[24] K. X. Wang, Z. Yu, V. Liu, Y. Cui, and S. Fan, "Absorption enhancement in ultrathin crystalline silicon solar cells with antireflection and light-trapping nanocone gratings," *Nano Letters*, vol. 12, no. 3, pp. 1616–1619, 2012.

[25] P. Pathi, A. Peer, and R. Biswas, "Nano-photonic structures for light trapping in ultra-thin crystalline silicon solar cells," *Nanomaterials*, vol. 7, no. 1, p. 17, 2017.

[26] D. M. Schaadt, B. Feng, and E. T. Yu, "Enhanced semiconductor optical absorption via surface plasmon excitation in metal nanoparticles," *Applied Physics Letters*, vol. 86, no. 6, p. 063106, 2005.

[27] P. Matheu, S. H. Lim, D. Derkacs, C. McPheeters, and E. T. Yu, "Metal and dielectric nanoparticle scattering for improved optical absorption in photovoltaic devices," *Applied Physics Letters*, vol. 93, no. 11, p. 113108, 2008.

[28] K. Yamamoto, M. Yoshimi, Y. Tawada, Y. Okamoto, A. Nakajima, and S. Igari, "Thin-film poly-Si solar cells on glass substrate fabricated at low temperature," *Applied Physics A*, vol. 69, pp. 179–185, Aug 1999.

[29] M. D. Kelzenberg, S. W. Boettcher, J. A. Petykiewicz, D. B. Turner-Evans, M. C. Putnam, E. L. Warren, J. M. Spurgeon, R. M. Briggs, N. S. Lewis, and H. A. Atwater, "Enhanced absorption and carrier collection in Si wire arrays for photovoltaic applications," *Nat Mater*, vol. 9, pp. 239–244, Mar 2010.

[30] D. M. Callahan, J. N. Munday, and H. A. Atwater, "Solar cell light trapping beyond the ray optic limit," *Nano Letters*, vol. 12, no. 1, pp. 214–218, 2012.

[31] T. Markvart, "Beyond the yablonovitch limit: Trapping light by frequency shift," *Applied Physics Letters*, vol. 98, no. 7, p. 071107, 2011.

[32] J. Schmidt, M. Kerr, and P. P. Altermatt, "Coulomb-enhanced auger recombination in crystalline silicon at intermediate and high injection densities," *Journal of Applied Physics*, vol. 88, no. 3, pp. 1494–1497, 2000.

[33] K. R. McIntosh and L. E. Black, "On effective surface recombination parameters," *Journal of Applied Physics*, vol. 116, no. 1, p. 014503, 2014.

[34] Y. Kang, *High Efficiency Thin Film Crystalline Solar Cells*. PhD thesis, Stanford University, 2015.

[35] E. Yablonovitch and G. D. Cody, "Intensity enhancement in textured optical sheets for solar cells," *IEEE Transactions on Electron Devices*, vol. 29, pp. 300–305, Feb 1982.

[36] E. Yablonovitch, "Statistical ray optics," *J. Opt. Soc. Am.*, vol. 72, pp. 899–907, Jul 1982.

[37] M. A. Green, "Lambertian light trapping in textured solar cells and light-emitting diodes: analytical solutions," *Progress in Photovoltaics: Research and Applications*, vol. 10, no. 4, pp. 235–241, 2002.

[38] Z. Yu, A. Raman, and S. Fan, "Fundamental limit of nanophotonic light trapping in solar cells," *Proceedings of the National Academy of Sciences*, vol. 107, no. 41, pp. 17491–17496, 2010.

[39] C. Wang, S. Yu, W. Chen, and C. Sun, "Highly efficient light-trapping structure design inspired by natural evolution," vol. 3, pp. 1025 EP –, Jan 2013.

[40] J. Robertson, R. Gillen, and S. Clark, "Advances in understanding of transparent conducting oxides," *Thin Solid Films*, vol. 520, no. 10, pp. 3714 – 3720, 2012.

[41] L. Lin, J. Robertson, and S. Clark, "Shifting schottky barrier heights with ultra-thin dielectric layers," *Microelectronic Engineering*, vol. 88, no. 7, pp. 1461 – 1463, 2011.

[42] S. Das, H.-Y. Chen, A. V. Penumatcha, and J. Appenzeller, "High performance multilayer $MoS_2$ transistors with scandium contacts," *Nano Letters*, vol. 13, no. 1, pp. 100–105, 2013.

[43] J. Robertson and S. J. Clark, "Limits to doping in oxides," *Phys. Rev. B*, vol. 83, p. 075205, Feb 2011.

[44] T. Hitosugi, N. Yamada, S. Nakao, Y. Hirose, and T. Hasegawa, "Properties of $TiO_2$-based transparent conducting oxides," *physica status solidi (a)*, vol. 207, no. 7, pp. 1529–1537, 2010.

[45] O. Lupan, S. Shishiyanu, V. Ursaki, H. Khallaf, L. Chow, T. Shishiyanu, V. Sontea, E. Monaico, and S. Railean, "Synthesis of nanostructured Al-doped zinc oxide films on Si for solar cells applications," *Solar Energy Materials & Solar Cells*, vol. 93, pp. 1417–1422, Aug 2009.

[46] S. Nandy, U. N. Maiti, C. K. Ghosh, and K. K. Chattopadhyay, "Enhanced p-type conductivity and band gap narrowing in heavily Al doped NiO thin films deposited by RF magnetron sputtering," *Journal of Physics: Condensed Matter*, vol. 21, no. 11, p. 115804, 2009.

[47] G. Hautier, A. Miglio, G. Ceder, G.-M. Rignanese, and X. Gonze, "Identification and design principles of low hole effective mass p-type transparent conducting oxides," *Nat Commun*, vol. 4, Aug. 2013.

[48] R. Stangl, C. Leendertz, and J. Haschke, *Numerical Simulation of Solar Cells and Solar Cell Characterization Methods: the Open-Source on Demand Program AFORS-HET, Solar Energy, Radu D. Rugescu (Ed.)*, ch. 14, pp. 319–352. InTech, Feb. 2010.

[49] R. Islam, G. Shine, and K. C. Saraswat, "Schottky barrier height reduction for holes by fermi level depinning using metal/nickel oxide/silicon contacts," *Applied Physics Letters*, vol. 105, no. 18, p. 182103, 2014.

[50] D. Norton, Y. Heo, M. Ivill, K. Ip, S. Pearton, M. Chisholm, and T. Steiner, "ZnO: growth, doping & processing," *Materials Today*, vol. 7, no. 6, pp. 34 – 40, 2004.

[51] J. A. del Alamo and R. M. Swanson, "Modelling of minority-carrier transport in heavily doped silicon emitters," *Solid-State Electronics*, vol. 30, no. 11, pp. 1127 – 1136, 1987.

[52] M. Tyagi and R. V. Overstraeten, "Minority carrier recombination in heavily-doped silicon," *Solid-State Electronics*, vol. 26, no. 6, pp. 577 – 597, 1983.

[53] A. Louwen, W. van Sark, R. Schropp, and A. Faaij, "A cost roadmap for silicon heterojunction solar cells," *Solar Energy Materials and Solar Cells*, vol. 147, pp. 295 – 314, 2016.

[54] M. A. Green, "The path to 25% silicon solar cell efficiency: History of silicon cell evolution," *Progress in Photovoltaics: Research and Applications*, vol. 17, no. 3, pp. 183–189, 2009.

[55] A. Richter, M. Hermle, and S. W. Glunz, "Reassessment of the limiting efficiency for crystalline silicon solar cells," *IEEE Journal of Photovoltaics*, vol. 3, pp. 1184–1191, Oct 2013.

[56] S. Avasthi, S. Lee, Y.-L. Loo, and J. C. Sturm, "Role of majority and minority carrier barriers silicon/organic hybrid heterojunction solar cells," *Advanced Materials*, vol. 23, no. 48, pp. 5762–5766, 2011.

[57] R. Islam and K. Saraswat, "Metal/insulator/semicondcutor carrier selective contacts for photovoltaic cells," in *Proc. IEEE Photovoltaic Specialist Conference (PVSC '14)*, (Denver, USA), pp. 285–289, June 2014.

[58] U. Würfel, A. Cuevas, and P. Würfel, "Charge carrier separation in solar cells," *IEEE Journal of Photovoltaics*, vol. 5, pp. 461–469, Jan 2015.

[59] M. Tanaka, M. Taguchi, T. Matsuyama, T. Sawada, S. Tsuda, S. Nakano, H. Hanafusa, and Y. Kuwano, "Development of new a-Si/c-Si heterojunction solar cells: ACJ-HIT (artificially constructed junction-heterojunction with intrinsic thin-layer)," *Japanese Journal of Applied Physics*, vol. 31, no. 11R, p. 3518, 1992.

[60] K. Masuko, M. Shigematsu, T. Hashiguchi, D. Fujishima, M. Kai, N. Yoshimura, T. Yamaguchi, Y. Ichihashi, T. Mishima, N. Matsubara, T. Yamanishi, T. Takahama, M. Taguchi, E. Maruyama, and S. Okamoto, "Achievement of more than 25 % conversion efficiency with crystalline silicon heterojunction solar cell," *IEEE Journal of Photovoltaics*, vol. 4, pp. 1433–1435, Nov 2014.

[61] Z. C. Holman, A. Descoeudres, L. Barraud, F. Z. Fernandez, J. P. Seif, S. D. Wolf, and C. Ballif, "Current losses at the front of silicon heterojunction solar cells," *IEEE Journal of Photovoltaics*, vol. 2, pp. 7–15, Jan 2012.

[62] S. Avasthi, K. A. Nagamatsu, J. Jhaveri, W. E. McClain, G. Man, A. Kahn, J. Schwartz, S. Wagner, and J. C. Sturm, "Double-heterojunction crystalline silicon solar cell fabricated at 250 °C with 12.9 % efficiency," in *2014 IEEE 40th Photovoltaic Specialist Conference (PVSC)*, pp. 0949–0952, June 2014.

[63] K. A. Nagamatsu, S. Avasthi, J. Jhaveri, and J. C. Sturm, "A 12% efficient silicon/PEDOT:PSS heterojunction solar cell fabricated at $< 100$ °C," *IEEE Journal of Photovoltaics*, vol. 4, pp. 260–264, Jan 2014.

[64] C. Battaglia, X. Yin, M. Zheng, I. D. Sharp, T. Chen, S. McDonnell, A. Azcatl, C. Carraro, B. Ma, R. Maboudian, R. M. Wallace, and A. Javey, "Hole selective MoOx contact for silicon solar cells," *Nano Letters*, vol. 14, no. 2, pp. 967–971, 2014.

[65] J. Geissbühler, J. Werner, S. Martin de Nicolas, L. Barraud, A. Hessler-Wyser, M. Despeisse, S. Nicolay, A. Tomasi, B. Niesen, S. De Wolf, and C. Ballif, "22.5% efficient silicon heterojunction solar cell with molybdenum oxide hole collector," *Applied Physics Letters*, vol. 107, no. 8, p. 081601, 2015.

[66] J. Bullock, M. Hettick, J. Geissbühler, A. J. Ong, T. Allen, C. M. Sutter-Fella, T. Chen, H. Ota, E. W. Schaler, S. De Wolf, C. Ballif, A. Cuevas, and A. Javey, "Efficient silicon solar cells with dopant-free asymmetric heterocontacts," *Nature Energy*, vol. 1, p. 15031, Jan 2016.

[67] K.-U. Ritzau, M. Bivour, S. Schröer, H. Steinkemper, P. Reinecke, F. Wagner, and M. Hermle, "TCO work function related transport losses at the a-Si:H/TCO-contact in SHJ solar cells," *Solar Energy Materials and Solar Cells*, vol. 131, pp. 9 – 13, 2014.

[68] M. Mews, L. Korte, and B. Rech, "Oxygen vacancies in tungsten oxide and their influence on tungsten oxide/silicon heterojunction solar cells," *Sol. Energy Mater. Sol. Cells*, vol. 158, pp. 77–83, 2016.

[69] R. Rö$\beta$ler, C. Leendertz, L. Korte, N. Mingirulli, and B. Rech, "Impact of the transparent conductive oxide work function on injection-dependent a-Si:H/c-Si band bending and solar cell parameters," *Journal of Applied Physics*, vol. 113, no. 14, p. 144513, 2013.

[70] R. Varache, C. Leendertz, M. Gueunier-Farret, J. Haschke, D. Munõz, and L. Korte, "Investigation of selective junctions using a newly developed tunnel current model for solar cell applications," *Solar Energy Materials and Solar Cells*, vol. 141, pp. 14 – 23, 2015.

[71] W. Mönch, "Barrier heights of real schottky contacts explained by metal-induced gap states and lateral inhomogeneities," *Journal of Vacuum Science & Technology B*, vol. 17, no. 4, pp. 1867–1876, 1999.

[72] W. Mönch, "Role of virtual gap states and defects in metal-semiconductor contacts," *Phys. Rev. Lett.*, vol. 58, pp. 1260–1263, Mar 1987.

[73] A. B. Kunz, "Electronic structure of NiO," *Journal of Physics C: Solid State Physics*, vol. 14, no. 16, p. L455, 1981.

[74] M. Guziewicz, J. Grochowski, M. Borysiewicz, E. Kaminska, J. Z. Domagala, W. Rzodkiewicz, B. S. Witkowski, K. Golaszewska, R. Kruszka, M. Ekielski, and A. Piotrowska, "Electrical and optical properties of NiO films deposited by magnetron sputtering," *Optica Applicata*, vol. 41, no. 2, pp. 431–440, 2011.

[75] K. X. Steirer, J. P. Chesin, N. E. Widjonarko, J. J. Berry, A. Miedaner, D. S. Ginley, and D. C. Olson, "Solution deposited NiO thin-films as hole transport layers in organic photovoltaics," *Organic Electronics*, vol. 11, no. 8, pp. 1414 – 1418, 2010.

[76] P. Paramahans Manik, R. Kesh Mishra, V. Pavan Kishore, P. Ray, A. Nainani, Y.-C. Huang, M. C. Abraham, U. Ganguly, and S. Lodha, "Fermi-level unpinning and low resistivity in contacts to n-type Ge with a thin ZnO interfacial layer," *Applied Physics Letters*, vol. 101, no. 18, p. 182105, 2012.

[77] L. Petti, N. Münzenrieder, C. Vogt, H. Faber, L. Büthe, G. Cantarella, F. Bottacchi, T. D. Anthopoulos, and G. Tröster, "Metal oxide semiconductor thin-film transistors for flexible electronics," *Appl. Phys. Rev.*, vol. 3, no. 2, p. 021303, 2016.

[78] G. Korotcenkov, "Metal oxides for solid-state gas sensors: What determines our choice?," *Mater. Sci. Eng., B*, vol. 139, no. 1, pp. 1–23, 2007.

[79] D. Ielmini, "Resistive switching memories based on metal oxides: Mechanisms, reliability and scaling," *Semicond. Sci. Technol.*, vol. 31, no. 6, p. 063002, 2016.

[80] D. S. Jeong, R. Thomas, R. S. Katiyar, J. F. Scott, H. Kohlstedt, A. Petraru, and C. S. Hwang, "Emerging memories: Resistive switching mechanisms and current status," *Rep. Prog. Phys.*, vol. 75, no. 7, p. 076502, 2012.

[81] K. M. Kim, D. S. Jeong, and C. S. Hwang, "Nanofilamentary resistive switching in binary oxide system; a review on the present status and outlook," *Nanotechnology*, vol. 22, no. 25, p. 254002, 2011.

[82] J. A. Dawson, Y. Guo, and J. Robertson, "Energetics of intrinsic defects in NiO and the consequences for its resistive random access memory performance," *Appl. Phys. Lett.*, vol. 107, no. 12, p. 122110, 2015.

[83] F. J. Morin, "Oxides of the 3d transition metals," *Bell Syst. Tech. J.*, vol. 37, no. 4, pp. 1047–1084, 1958.

[84] S. P. Mitoff, "Electrical conductivity and thermodynamic equilibrium in nickel oxide," *J. Chem. Phys.*, vol. 35, no. 3, p. 882, 1961.

[85] L. Liu, Y. Hou, B. Chen, B. Gao, and J. Kang, "Improved unipolar resistive switching characteristics of mixed-$NiO_x$/$NiO_y$-film-based resistive switching memory devices," *Jpn. J. Appl. Phys.*, vol. 54, no. 9, p. 094201, 2015.

[86] R. Islam, K. N. Nazif, and K. C. Saraswat, "Si heterojunction solar cells: A simulation study of the design issues," *IEEE Trans. Electron Devices*, vol. 63, no. 12, pp. 4788–4795, 2016.

[87] F. Wang, G. Sun, C. Li, J. Liu, S. Hu, H. Zheng, Z. Tan, and Y. Li, "Finding the lost open-circuit voltage in polymer solar cells by UV-ozone treatment of the nickel acetate anode buffer layer," *ACS Appl. Mater. Interfaces*, vol. 6, no. 12, pp. 9458–9465, 2014.

[88] C. W. Chen, F. Ren, G.-C. Chi, S.-C. Hung, Y. P. Huang, J. Kim, I. I. Kravchenko, and S. J. Pearton, "UV ozone treatment for improving contact resistance on graphene," *J. Vac. Sci. Technol., B: Nanotechnol. Microelectron.: Mater., Process., Meas., Phenom.*, vol. 30, no. 6, p. 060604, 2012.

[89] A. E. Özçam, K. Efimenko, and J. Genzer, "Effect of ultraviolet/ozone treatment on the surface and bulk properties of poly(dimethyl siloxane) and poly(vinylmethyl siloxane) networks," *Polymer*, vol. 55, no. 14, pp. 3107 – 3119, 2014.

[90] S. Liu, R. Liu, Y. Chen, S. Ho, J. H. Kim, and F. So, "Nickel oxide hole injection/transport layers for efficient solution-processed organic light-emitting diodes," *Chem. Mater.*, vol. 26, no. 15, pp. 4528–4534, 2014.

[91] J. R. Vig, "UV/ozone cleaning of surfaces," *J. Vac. Sci. Technol., A*, vol. 3, no. 3, p. 1027, 1985.

[92] H. Kirihata and M. Uda, "Externally quenched air counter for low-energy electron emission measurements," *Rev. Sci. Instrum.*, vol. 52, no. 1, p. 68, 1981.

[93] Y. Nakajima, M. Hoshino, D. Yamashita, and M. Uda, "Near edge structures of Mg-, Co-, Cu- and Zn-tetraphenylporphyrins measured by PESA and calculated with DV-X$\alpha$," *Adv. Quantum Chem.*, vol. 42, pp. 399–405, 2003.

[94] K. Kim and N. Winograd, "X-ray photoelectron spectroscopic studies of nickel-oxygen surfaces using oxygen and argon ion-bombardment," *Surf. Sci*, vol. 43, no. 2, pp. 625–643, 1974.

[95] A. P. Grosvenor, M. C. Biesinger, R. S. Smart, and N. S. McIntyre, "New interpretations of XPS spectra of nickel metal and oxides," *Surf. Sci.*, vol. 600, no. 9, pp. 1771–1779, 2006.

[96] C. Brundle and A. Carley, "Oxygen adsorption on nickel surfaces: Detection of different species by X-ray photoelectron spectroscopy," *Chem. Phys. Lett.*, vol. 31, no. 3, pp. 423–427, 1975.

[97] J. Yu, K. M. Rosso, and S. M. Bruemmer, "Charge and ion transport in NiO and aspects of Ni oxidation from first principles," *J. Phys. Chem. C*, vol. 116, no. 2, pp. 1948–1954, 2012.

[98] S. M. Sze and K. K. Ng, *Physics of Semiconductor Devices, $3^{rd}$ ed.* Hoboken, New Jersey: Wiley-Interscience, 2007.

[99] E. L. Ratcliff, J. Meyer, K. X. Steirer, A. Garcia, J. J. Berry, D. S. Ginley, D. C. Olson, A. Kahn, and N. R. Armstrong, "Evidence for near-surface NiOOH species in solution-processed $NiO_x$ selective interlayer materials: Impact on energetics and the performance of polymer bulk heterojunction photovoltaics," *Chem. Mater.*, vol. 23, no. 22, pp. 4988–5000, 2011.

[100] V. Heine, "Theory of surface states," *Phys. Rev.*, vol. 138, pp. A1689–A1696, Jun 1965.

[101] D. Connelly, C. Faulkner, P. A. Clifton, and D. E. Grupp, "Fermi-level depinning for low-barrier schottky source/drain transistors," *Appl. Phys. Lett.*, vol. 88, no. 1, 2006.

[102] J. Hu, K. C. Saraswat, and H.-S. P. Wong, "Metal/III-V schottky barrier height tuning for the design of nonalloyed III-V field-effect transistor source/drain contacts," *Journal of Applied Physics*, vol. 107, no. 6, 2010.

[103] J.-Y. J. Lin, A. M. Roy, A. Nainani, Y. Sun, and K. C. Saraswat, "Increase in current density for metal contacts to n-germanium by inserting $TiO_2$ interfacial layer to reduce schottky barrier height," *Appl. Phys. Lett.*, vol. 98, no. 9, p. 092113, 2011.

[104] A. Agrawal, J. Lin, B. Zheng, S. Sharma, S. Chopra, K. Wang, A. Gelatos, S. Mohney, and S. Datta, "Barrier height reduction to 0.15 eV and contact resistivity reduction to $9.1\times 10^{-9}$ $\Omega$-cm$^2$ using ultrathin $TiO_{2-x}$ interlayer between metal and silicon," in *2013 Symposium on VLSI Technology (VLSIT)*, pp. T200–T201, IEEE, 2013.

[105] G. Shine and K. Saraswat, "Limits of specific contact resistivity to Si, Ge and III-V semiconductors using interfacial layers," in *2013 International Conference on Simulation of Semiconductor Processes and Devices (SISPAD)*, pp. 69–72, Sept 2013.

[106] H. Sato, T. Minami, S. Takata, and T. Yamada, "Transparent conducting p-type NiO thin films prepared by magnetron sputtering," *Thin Solid Films*, vol. 236, no. 1 - 2, pp. 27 – 31, 1993.

[107] H. Wu and L.-S. Wang, "A study of nickel monoxide (NiO), nickel dioxide (ONiO), and Ni($O_2$) complex by anion photoelectron spectroscopy," *J. Chem. Phys.*, vol. 107, no. 1, pp. 16–21, 1997.

[108] This work was performed in collaboration with Yusi Chen (Harris Group, Stanford University).

[109] D. E. Kane and R. M. Swanson, "Measurement of the emitter saturation current by a contactless photoconductivity decay method," in *Proc. of the 18th IEEE Photovoltaic Specialists Conference*, pp. 578–583, IEEE, 1985.

[110] R. A. Sinton, A. Cuevas, and M. Stuckings, "Quasi-steady-state photoconductance, a new method for solar cell material and device characterization," in *Conference Record of the Twenty Fifth IEEE Photovoltaic Specialists Conference - 1996*, pp. 457–460, May 1996.

[111] "International Technology Roadmap for Photovoltaics." `http://www.itrpv.net/Reports/Downloads/`, 2017. [Online].

[112] J. Yoon, A. J. Baca, S.-I. Park, P. Elvikis, J. B. Geddes, L. Li, R. H. Kim, J. Xiao, S. Wang, T.-H. Kim, M. J. Motala, B. Y. Ahn, E. B. Duoss, J. A. Lewis, R. G. Nuzzo, P. M. Ferreira, Y. Huang, A. Rockett, and J. A. Rogers, "Ultrathin silicon solar microcells for semitransparent, mechanically flexible and microconcentrator module designs," *Nature Materials*, vol. 7, pp. 907–915, Nov 2008.

[113] E. Garnett and P. Yang, "Light trapping in silicon nanowire solar cells," *Nano Letters*, vol. 10, no. 3, pp. 1082–1087, 2010.

[114] S. Wang, B. D. Weil, Y. Li, K. X. Wang, E. Garnett, S. Fan, and Y. Cui, "Large-area free-standing ultrathin single-crystal silicon as processable materials," *Nano Letters*, vol. 13, no. 9, pp. 4393–4398, 2013.

[115] K. A. Bush, A. F. Palmstrom, Z. J. Yu, M. Boccard, R. Cheacharoen, J. P. Mailoa, D. P. McMeekin, R. L. Z. Hoye, C. D. Bailie, T. Leijtens, I. M. Peters, M. C. Minichetti, N. Rolston, R. Prasanna, S. Sofia, D. Harwood, W. Ma, F. Moghadam, H. J. Snaith, T. Buonassisi, Z. C. Holman, S. F. Bent, and M. D. McGehee, "23.6%-efficient monolithic perovskite/silicon tandem solar cells with improved stability," vol. 2, pp. 17009 EP –, Feb 2017.

[116] J. Werner, C.-H. Weng, A. Walter, L. Fesquet, J. P. Seif, S. De Wolf, B. Niesen, and C. Ballif, "Efficient monolithic perovskite/silicon tandem solar cell with cell area >1 $cm^2$," *The Journal of Physical Chemistry Letters*, vol. 7, no. 1, pp. 161–166, 2016.

[117] A. V. Shah, H. Schade, M. Vanecek, J. Meier, E. Vallat-Sauvain, N. Wyrsch, U. Kroll, C. Droz, and J. Bailat, "Thin-film silicon solar cell technology," *Progress in Photovoltaics: Research and Applications*, vol. 12, no. 2-3, pp. 113–142, 2004.

[118] Y. Liu, Y. Chen, D. T. LaFehr, Y. Su, Y. Huo, Y. Kang, H. Deng, J. Jia, L. Zhao, M. Yuan, Z. Lyu, D. DeWitt, M. A. Vilgalys, K. Zang, X. Chen, C.-Y. Lu, T. I. Kamins, and J. S. Harris, "Titanium oxide electron-selective layers for contact passivation of thin-film crystalline silicon solar cells," in *Proc. SPIE*, vol. 9749, pp. 97491J–97491J–8, 2016.

[119] L. Tous, M. Aleman, R. Russell, E. Cornagliotti, P. Choulat, A. Uruena, S. Singh, J. John, F. Duerinckx, J. Poortmans, and R. Mertens, "Evaluation of advanced p-perl and n-pert large area silicon solar cells with 20.5 % energy conversion efficiencies," *Progress in Photovoltaics: Research and Applications*, vol. 23, no. 5, pp. 660–670, 2015.

[120] P. Kowalczewski and L. C. Andreani, "Towards the efficiency limits of silicon solar cells: How thin is too thin?," *Solar Energy Materials and Solar Cells*, vol. 143, pp. 260 – 268, 2015.

[121] S. E. Han and G. Chen, "Toward the lambertian limit of light trapping in thin nanostructured silicon solar cells," *Nano Letters*, vol. 10, no. 11, pp. 4692–4696, 2010.

[122] S. Zhong, Z. Huang, X. Lin, Y. Zeng, Y. Ma, and W. Shen, "High-efficiency nanostructured silicon solar cells on a large scale realized through the suppression of recombination channels," *Advanced Materials*, vol. 27, no. 3, pp. 555 – 561, 2015.

[123] G. Li, H. Li, J. Y. L. Ho, M. Wong, and H. S. Kwok, "Nanopyramid structure for ultrathin c-si tandem solar cells," *Nano Letters*, vol. 14, no. 5, pp. 2563–2568, 2014.

[124] R. Newman and R. M. Chrenko, "Optical properties of nickel oxide," *Phys. Rev.*, vol. 114, pp. 1507–1513, Jun 1959.

[125] M. D. Irwin, D. B. Buchholz, A. W. Hains, R. P. H. Chang, and T. J. Marks, "p-type semiconducting nickel oxide as an efficiency-enhancing anode interfacial layer in polymer bulk-heterojunction solar cells," *Proceedings of the National Academy of Sciences*, vol. 105, no. 8, pp. 2783–2787, 2008.

[126] X. Chen and S. S. Mao, "Titanium dioxide nanomaterials: Synthesis, properties, modifications, and applications," *Chemical Reviews*, vol. 107, no. 7, pp. 2891–2959, 2007.

[127] A. Fujishima, T. N. Rao, and D. A. Tryk, "Titanium dioxide photocatalysis," *Journal of Photochemistry and Photobiology C: Photochemistry Reviews*, vol. 1, no. 1, pp. 1 – 21, 2000.

[128] F. Feldmann, M. Simon, M. Bivour, C. Reichel, M. Hermle, and S. W. Glunz, "Carrier-selective contacts for si solar cells," *Applied Physics Letters*, vol. 104, no. 18, p. 181105, 2014.

[129] X. Yang, P. Zheng, Q. Bi, and K. Weber, "Silicon heterojunction solar cells with electron selective $TiO_x$ contact," *Solar Energy Materials and Solar Cells*, vol. 150, pp. 32 – 38, 2016.

[130] A. Agrawal, J. Lin, M. Barth, R. White, B. Zheng, S. Chopra, S. Gupta, K. Wang, J. Gelatos, S. E. Mohney, and S. Datta, "Fermi level depinning and contact resistivity reduction using a reduced titania interlayer in n-silicon metal-insulator-semiconductor ohmic contacts," *Applied Physics Letters*, vol. 104, no. 11, p. 112101, 2014.

[131] K. A. Nagamatsu, S. Avasthi, G. Sahasrabudhe, G. Man, J. Jhaveri, A. H. Berg, J. Schwartz, A. Kahn, S. Wagner, and J. C. Sturm, "Titanium dioxide/silicon hole-blocking selective contact to enable double-heterojunction crystalline silicon-based solar cell," *Applied Physics Letters*, vol. 106, no. 12, p. 123906, 2015.

[132] A. Gaucher, A. Cattoni, C. Dupuis, W. Chen, R. Cariou, M. Foldyna, L. Lalouat, E. Drouard, C. Seassal, P. Roca i Cabarrocas, and S. Collin, "Ultrathin epitaxial silicon solar cells with inverted nanopyramid arrays for efficient light trapping," *Nano Letters*, vol. 16, no. 9, pp. 5358–5364, 2016.

[133] Y. Hayashi, "Crystalline silicon solar cells, thinner the better," in *2010 International Conference on Solid State Devices and Materials*, pp. 1237–1238, The Japan Society of Applied Physics, Sep 2010. Invited Talk.

[134] S. S. oes, R. Calinas, M. T. Vieira, M. F. Vieira, and P. J. Ferreira, "In situ TEM study of grain growth in nanocrystalline copper thin films," *Nanotechnology*, vol. 21, no. 14, p. 145701, 2010.

[135] P. F. Satterthwaite, A. G. Scheuermann, P. K. Hurley, C. E. D. Chidsey, and P. C. McIntyre, "Engineering interfacial silicon dioxide for improved metal-insulator-semiconductor silicon photoanode water splitting performance," *ACS Applied Materials & Interfaces*, vol. 8, no. 20, pp. 13140–13149, 2016.

[136] K.-I. Seo, D.-I. Lee, P. Pianetta, H. Kim, K. C. Saraswat, and P. C. McIntyre, "Chemical states and electrical properties of a high-k metal oxide/silicon interface with oxygen-gettering titanium-metal-overlayer," *Applied Physics Letters*, vol. 89, no. 14, p. 142912, 2006.

[137] R. D. Shannon, T. E. Gier, P. F. Carcia, P. E. Bierstedt, R. B. Flippen, and A. J. Vega, "Synthesis and properties of platinum metal oxides of the type $M_xPt_3O_4$," *Inorganic Chemistry*, vol. 21, no. 9, pp. 3372–3382, 1982.

[138] K. Schwartz and C. Prewitt, "Structural and electronic properties of binary and ternary platinum oxides," *Journal of Physics and Chemistry of Solids*, vol. 45, no. 1, pp. 1 – 21, 1984.

[139] D. Cahen, J. A. Ibers, and R. D. Shannon, "Structure and properties of $Ni_{0.25}Pt_3O_4$. new platinum bronze," *Inorganic Chemistry*, vol. 11, no. 10, pp. 2311–2315, 1972.

[140] G. Sahasrabudhe, S. M. Rupich, J. Jhaveri, A. H. Berg, K. A. Nagamatsu, G. Man, Y. J. Chabal, A. Kahn, S. Wagner, J. C. Sturm, and J. Schwartz, "Low-temperature synthesis of a TiO2/Si heterojunction," *Journal of the American Chemical Society*, vol. 137, no. 47, pp. 14842–14845, 2015.

[141] K. Yoshikawa, H. Kawasaki, W. Yoshida, T. Irie, K. Konishi, K. Nakano, T. Uto, D. Adachi, M. Kanematsu, H. Uzu, and K. Yamamoto, "Silicon heterojunction solar cell with interdigitated back contacts for a photoconversion efficiency over 26%," vol. 2, pp. 17032 EP –, Mar 2017. Article.

[142] M. M. Furchi, A. A. Zechmeister, F. Hoeller, S. Wachter, A. Pospischil, and T. Mueller, "Photovoltaics in Van der Waals heterostructures," *IEEE Journal of Selected Topics in Quantum Electronics*, vol. 23, pp. 106–116, Jan 2017.